UNIVERSITÉ DE STRASBOURG

ÉCOLE DOCTORALE DE PHYSIQUE ET CHIMIE PHYSIQUE
Institut Pluridisciplinaire Hubert Curien (IPHC), UMR 7178

THÈSE

présentée par:

Reem Rasheed

soutenue en : **18 Décembre 2020**

pour obtenir le grade de: **Docteur de l'Université de Strasbourg**
Discipline/Spécialité: Physique des particules

Recherche de nouvelles physiques grâce à la désintégration radiative de mésons B et mesure de leur temps de vie avec l'expérience Belle II

THÈSE dirigée par:

Pr. Jérôme Baudot	Institut Pluridisciplinaire Hubert Curien

RAPPORTEURS:

Pr. Haitham Zaraket	Lebanese university, Faculty of sciences
Pr. Olivier Schneider	Ecole Polytechnique Fédérale de Lausane

AUTRES MEMBRES DU JURY:

Mr Karim Trabelsi	IJCLab, Orsay
Mme Christelle Roy	IPHCS, Strasbourg
Mr Alessandro Gaz	Kobayashi-Masakawa Institute

Abstract

After the Big Bang matter and antimatter were present in equal amounts. Today, however, everything we see, is made almost entirely of matter. A fundamental ingredient to explain this asymmetry between matter and antimatter is the violation of the CP (Charge Parity) symmetry. CP violation has been observed but quantitatively not enough to explain the huge asymmetry. The Belle II experiment in Japan studies the particles produced in electron-positron collisions at the SuperKEKB collider, the highest intensity collider in the World, allowing a high precision measurements of the known sources of CP violation and looking for new ones. In this document, I present my work on measuring the CP violation in B meson radiative decays (decays with photon in final state) particularly promising thanks to their high sensitivity to possible new processes. Following this analysis, I present a new measurement of the B mesons lifetime where I could verify the robustness of the tools used in the CP violation measurement.

Acknowledgements

Thanks to all whom helped in contributing and finishing this work. My supervisor Jerome Baudot, thank you for all the ideas and instructions that helped me evolve my thesis with great results, thank you as well for all the humanistic care you gave me through my ups and downs during these three years. Isabelle-Ripp Baudot, thank you being the strong boss organizing all our activities in the Belle II collaboration, and a great co-director for my thesis. Special thanks for Giulio Dujany for this contribution to the B^0 lifetime analysis that helped to make it more complete and faster published. I thank the director of the doctoral school, Aziz Dinia, for giving me the opportunity to go through this research journey and obtain the PhD degree. I'm also grateful to the Belle II physics convener, Alessandro Gaz, for his invitation and working with me at KMI institution in Nagoya, as well, thanks to all the Time Dependent CP violation group members in Belle II for their advises and comments on both analysis in this thesis.

Last but not least, thanks to my husband, the endless support and calmness. Thanks to my family, especially my mom, to whom I endow this degree. Finally, I thank all the jury members, who will read this thesis, and be part of my defense.

Contents

Introduction i

1 Overview of the Standard Model 1
- 1.0.1 Symmetries . . . 4
- 1.1 The Cabibbo-Kobayashi-Maskawa Matrix . . . 8
  - 1.1.1 Unitarity traingle . . . 8

2 Mixing and CP violation in neutral B meson 13
- 2.1 Mixing of neutral B meson . . . 13
  - 2.1.1 Decay rates . . . 17
- 2.2 CP violation in the B meson system . . . 17
- 2.3 CP violation in b $\to$ s γ transitions . . . 20
  - 2.3.1 Trees and Penguins . . . 20
  - 2.3.2 Photon polarization in radiative B^0 decays . . . 21
- 2.4 Physical observables and experimental status . . . 22
  - 2.4.1 Mixing-induced CP asymmetry . . . 23
  - 2.4.2 Summary of previous experimental results for $B^0 \to K^0_S\pi^0\gamma$ and $B^0 \to K^0_S\pi^+\pi^-\gamma$ . . . 24

3 SuperKEKB and Belle II project 25
- 3.1 SuperKEKB . . . 26
  - 3.1.1 Nano-beam scheme . . . 27
  - 3.1.2 Beam-Induced Background . . . 28
- 3.2 SuperKEKB commissioning and running phases . . . 30
- 3.3 Belle II detector . . . 30
  - 3.3.1 Tracking Detectors . . . 33
  - 3.3.2 Particle Identification devices . . . 36

3.3.3 Electromagnetic calorimeter . . . 40
3.3.4 The neutral kaon and muon detector . . . 40
3.3.5 Trigger . . . 41

4 TDCPV Analysis of $B^0 \to K^0_S\pi^+\pi^-\gamma$ and $B^0 \to K^0_S\pi^0\gamma$ 45
4.1 Principle of measurement . . . 45
4.1.1 Flavor tagging . . . 47
4.1.2 Extraction of CP violation parameter . . . 50
4.2 Preparation of measurement procedure . . . 52
4.2.1 Data samples . . . 52
4.2.2 $B^0 \to K^0_S\pi^+\pi^-\gamma$ and $B^0 \to K^0_S\pi^0\gamma$ decays . . . 52
4.3 Reconstruction and selection cuts . . . 52
4.3.1 Skim . . . 53
4.3.2 Selection cuts . . . 53
4.3.3 Reconstruction of B^0 meson . . . 55
4.3.4 Event-shape variables . . . 56
4.3.5 Cuts Optimization . . . 60
4.3.6 Multiple candidate selection . . . 62
4.4 Fit to M_{bc}, ΔE, Δt and Fisher . . . 63
4.4.1 Signal PDFs . . . 63
4.4.2 Background PDFs . . . 63
4.4.3 Signal to background fraction fit . . . 63
4.4.4 Results . . . 63
4.5 Systematics $B^0 \to K^0_S\pi^0\gamma$ . . . 66
4.5.1 Systematics $B^0 \to K^0_S\pi^+\pi^-\gamma$ . . . 67
4.5.2 Conclusion . . . 68

5 B^0 lifetime 69
5.1 Introduction . . . 69
5.2 Datasets used . . . 70
5.3 Event selection and reconstruction . . . 70
5.3.1 Signal side . . . 70
5.3.2 Tag side . . . 71
5.3.3 Signal and Tag side vertex fit . . . 72
5.3.4 Efficiencies . . . 72
5.3.5 Continuum suppression . . . 72
5.3.6 Regions defined . . . 73
5.3.7 Multiple candidates . . . 73
5.3.8 Time difference between the two B mesons . . . 73
5.4 Fit to get signal and background fractions . . . 74
5.4.1 Population distirbutions for M_{bc} and ΔE . . . 75
5.4.2 Fit to M_{bc} and ΔE to extract the signal and background contributions . . . 79

5.5 Lifetime extraction method 84
5.5.1 Modeling of Δt component for the three components . 85
5.5.2 Full fit Δt distribution P_{all} 89
5.5.3 Coutntinuum background Δt distribution from data sideband 91
5.6 Unblinding 91
5.7 Systematic uncertainties and cross checks 93
5.7.1 Fit systematic uncertainty 93
5.7.2 Systematic uncertainty for fixing τ_{eff} from simulation . 94
5.7.3 Calibration and alignment systematic uncertainty . . . 95
5.7.4 Total systematic uncertainty 95
5.8 Conclusion 97

Conclusion **i**

RÉSUMÉ français **v**

Appendix Probability density functions **i**
.1 Gaussian function i
.2 Crystal Ball function i
.3 Argus function i
.4 Chebychev function ii

Appendix Plots fit to get signal and background fractions for channels **iii**

Introduction

The main subject of my PhD is to search for experimental signs of New Physics (NP) that cannot be described by the current theory of particle physics, the Standard Model (SM). There are several ways to look for NP. At colliders, these studies are carried with the large hadron collider (LHC) of the European Organization for Nuclear Research (CERN) and with superKEKB located at the High Energy Accelerator Research Organisation in Japan (KEK). The latter was build to create a clean environment using the e^+e^- collisions, to study NP mainly in B and D meson and τ lepton systems, while the LHC collider has a wider physics programs using pp collisions.
The two previous projects of asymmetric B-factories, PEP-II [1] at SLAC and KEKB [2] at KEK started in 1999 and stopped in 2008 and 2010 respectively. The Belle experiment at KEK, recorded data at the world record instantaneous luminosity of 2.11×10^{34} cm^{-2}s^{-1}. A major success of these B-factories was the experimental confirmation of the formalism for CP (charge parity) violation proposed by Kobayashi Makoto and Toshishide Maskawa, who won the physics Nobel prize in 2008 for the "discovery of the origin of the broken symmetry which predicts the existence of at least three families of quarks in nature".
Various search for signs of New Physics were conducted by the BaBar and Belle collaborations, but the results obtained were statistically limited, restricting the ability to interpret the results as signs of new physics. This status motivated researchers in high energy physics to upgrade the KEKB collider to SuperKEKB. This new collider aims to reach a higher luminosity and collect about 50 times, in order to either discover signs of NP, or provide tight constraints on NP theoretical models. One of the hot program of the Belle II experiment, where Belle II is the updated detector of Belle is CP violation in B meson system.

My PhD program was to search for NP indications with CP violating effects in radiative B meson decays. What makes these decays interesting

is their sensitivity to new particles since they involve b to s quark transitions through quantum loops. While the Standard Model almost forbids any CP violation in such decays, NP models could generate sizable violation by restoring to some level the Left-Right symmetry broken in the SM that predicts photons emitted in $b \to s\ \gamma$ decays are only left-handed, up to small corrections.

Hence in my PhD, I worked on the measurement of the indirect and direct CP violation parameters, S and C respectively, in the $b \to s\gamma$ transitions occurring in the two decays $B^0 \to K^0_s\pi^+\pi^-\gamma$ and $B^0 \to K^0_s\pi^0\gamma$ as suggested in [3]. The branching fractions of these channels are 7×10^{-6} and 9.5×10^{-6} respectively, which are relatively small. Measurements on these channels were done by *Belle* [4] [5] and *Babar* [6] [7] experiments. The statistically limited results did not yield positive outcome for the search of New Physics. My goal was to investigate the sensitivity in these channels to non-zero value of the indirect CP violation parameter S using "Time dependent CP violation", TDCPV analysis with the Belle II dataset.

I started to work using simulated data to setup and tune the analysis, which consists mainly in selecting events potentially corresponding to the channel and then perform a fit to the data in order to extract the CP-violating parameter S, finalizing the analysis, I evaluated the possible systematical uncertainties for both channels. In addition, I developed the first measurement of the B^0 lifetime with real data in Belle II, since B^0 lifetime is precisely measured in particle physics experiments, measuring it in Belle II is a first demonstration of the tools used for the TDCPV analysis. B^0 lifetime measurement was documented in a Belle II conference paper, reported in 2020 winter conferences and published in May 2020 [8]. Both, TDCPV and B^0 lifetime analysis are discussed in the present document that is organized as follow.

In chapter one, an overview of Standard Model is presented, charge and parity symmetries are introduced as well and the origin of the CP violation in the Standard Model is elaborated. Then the properties of the complex CKM matrix is examined in detail, formalizing quark-mixing being the origin of the CP violation. The triangle related to the $B^0_d\ \overline{B}^0_d$ system, where most exciting physics of CP violation lies, is examined with its sides and angles parameters as well the current experimental status of these parameters are summarized.

In chapter two, I present the quantum mechanical properties of the neutral B^0 meson and its phenomenology allowing for the extraction of various CP-violating quantities. After that, I introduce the CP violation in $b \to s\ \gamma$ transitions, its correlation with New Physics as well as the physical quantities used to probe a sign of NP. A summary of previous experimental results done using $b \to s\ \gamma$ transition channels used in this thesis closes the chapter.

Chapter three describes the B factory concept and the main upgrades

needed to achieve the SuperKEKB designed luminosity of 8×10^{35} cm^{-2}s^{-1}, 40 times higher than its predecessor KEKB. It also presents the main phases of the accelerator commissioning and its luminosity run plan, which is crucial for the data taking and physics reach of the Belle II program, then the detector is discussed in detail. In particular, I summarize the improvements with respect to Belle needed to meet the high luminosity requirements, and briefly describe the sub-detectors, the trigger system, and the software framework relevant for this analysis.

TDCPV analysis strategy is fully detailed in chapter five. I start with the principles of this measurement and explain the tools, concepts used in the analysis. I elaborate the methodology followed to measure the CP violation parameters. Then, I list the results and explain the steps followed in the two analysis parts I studied for both channels, cuts optimization and systematical uncertainties calculation. I discuss the prospects of this analysis on the Belle II full data set, considering several improvement factors related to the fully installed detector and the increased luminosity.

Chapter six deals with the very first measurement of the B^0 lifetime with the real data accumulated in the first year of Belle II. The analysis is prepared on simulated samples with control data whenever possible. We especially insist on the development of the time resolution function, which is a crucial tool also for TDCPV analysis. Then the analysis method is applied blindly on the data to obtain the lifetime estimate and compared to the known world average value in order to assess the method robustness.

In the conclusion I summarize my results on the two aspects of my work, the TDCPV analysis preparation for radiative B decays and the early B^0 lifetime measurement and discuss the future prospects for both these analysis in Belle II.

CHAPTER 1

Overview of the Standard Model

In this chapter, I start with an overview of the Standard Model, then I introduce the charge and parity symmetries related to the main subject of this thesis, I elaborate the origin of the CP violation, the complex nature of the CKM matrix that is examined in detail, giving the relation between its elements and properties with CP violation of B_d system. Finalizing with the current experimental status of CKM parameters.

The Standard Model is a quantum field theory (QFT) that describes the dynamics of the known elementary particles, driven by the electromagnetic, weak and strong interactions. These interactions are mediated by the exchange of virtual particles, called gauge bosons. All gauge bosons included in the SM are vector bosons: they have a spin equal to 1 and obey Bose-Einstein statistics. Table 1.1 presents a list of SM interactions and their mediators (bosons). Although the gravitational force is not accounted for in the SM, its intensity at the elementary scale is so weak compared to the other interactions (many orders of magnitude lower) that it can be neglected. Finally, one should consider an additional fundamental particle: the recently discovered Higgs boson, a scalar boson of spin 0 associated with the so-called Brout-Englert-Higgs mechanism, through which the $W^{\pm}$ and Z^0 gauge bosons and all elementary fermions acquire their masses.

In opposition to bosons, the fermions, which are the constituents of matter,

Boson	Interaction	Mass(GeV/c^2)	charge (e)
Gluon	Strong	0	0
Photon	Electromagnetic	$< 10^{-24}$	0
$W^{\pm}$	weak	80.38 ± 0.015	± 1
Z^0	weak	91.188 ± 0.002	0

Table 1.1: Properties of force carrying bosons in the SM

are half-spin particles satisfying the Fermi-Dirac statistics and the Pauli exclusion principle. They are further categorized as leptons or quarks. Leptons are particles that, if charged, interact both electromagnetically and weakly, if neutral only weakly. Quarks are the fermionic constituents of hadrons and then nuclei, they interact strongly, weakly and electromagnetically.

The six flavours of leptons are grouped in three separate generations, composed respectively of the electron (e), muon (μ) and tau (τ) leptons, and the corresponding neutral neutrinos (ν_e, ν_μ , ν_τ). Charged leptons are sensitive to the electromagnetic and weak interactions, and have an integer electric charge of -1. Neutrinos only interact via the weak force and are considered massless in the SM, although it was proven experimentally that their masses must be extremely small but non-zero. Thus they interact very weakly and can only be detected with dedicated experiments. Quarks also come in 6 different flavours and are organized in three generations, comprising respectively the up (u) and down (d) quarks, the charm (c) and strange (s) quarks, and the top (t) and bottom (b) quarks. They are sensitive to the three interactions included in the SM, and they have a fractional electric charge of either $+\frac{2}{3}$ or $-\frac{1}{3}$. Due to the particular behaviour of the strong force, quarks can not exist freely but only confined together into composite hadrons, such as protons and neutrons.

All fermions also exist as antiparticles, which are identical to their corresponding particles in every aspect except having opposite internal quantum numbers (such as the electric charge). For both leptons and quarks, the three generations are ordered by increasing mass, and particles of higher generations will decay into lower mass ones. For this reason, the three first-generation particles only make up all the ordinary matter: up and down quarks bound into protons and neutrons which form the atoms's nuclei, around which electrons orbit (in the semi-classic formalism). Figure 1.1 summarizes all the particles included in the SM and their categorizations.

Mathematically, the SM theory is a unified quantum field theory obeying the following gauge group symmetry

$$SU(3)_C \times SU(2)_L \times U(1)_Y.$$

The interactions of quarks and leptons with the photon are described by the theory of quantum electrodynamics (QED) which is based on the Abelian, i.e. commutative, symmetry group of unitary 1×1 operators called $U(1)_{EM}$, EM sands for electromagnetic. Strong interactions are described by quantum

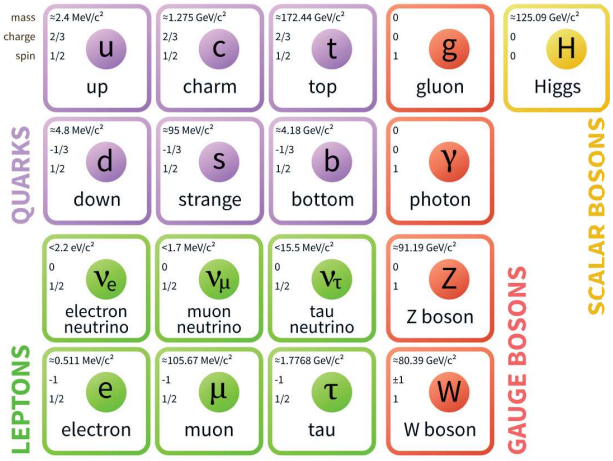


Figure 1.1: The elementary particles of the standard model. For each particle, mass, charge, spin and name are given. They are divided into three generations of quarks and leptons, gauge bosons as force carriers, and the Higgs boson. The fermions are shown in the same order as in the weak isospin doublets.

chromodynamics (QCD) which is based on the non- Abelian symmetry group $SU(3)_c$. The subscript c stands for color charge, or just color, which is the quantum number corresponding to the charge of the interaction. The three degrees of freedom of the symmetry group are the degrees of freedom of the color charge, which are labeled in analogy to the three kinds of colors humans perceive: red, green, blue. Apart from electric charge, every quark carries one of the three different color charges. Bound states of quarks can only exist if they are colourless; e.g. if a meson contains a green quark, its antiquark must be antigreen. The fact that colored objects do not exist as free particles is called *color confinement*.

Considering now weak interactions, they differ from the electromagnetic and the strong interactions. The symmetry group of the weak interaction is the non-Abelian $SU(2)_L$ group, where the subscript L stays for left-handed, indicating that the fermions participating in weak interactions are left-handed. Left-handed fermions form so-called weak isospin doublets and two such doublets compose each generation, while right-handed fermions are weak isospin singlet. The $W^{\pm}$ and Z^0 bosons results from the unification of electromagnetic and weak interactions. The unified interaction is called electroweak interaction and is described by the electroweak theory which is based on the symmetry group $SU(2)_L U(1)_Y$, where the subscript Y stays for hypercharge. I moved this sentence at the end, where it has more impact. The charged mediators of the weak interaction, the $W^{\pm}$ bosons, couple to all quark and lepton doublets; they are the only gauge bosons in the SM that can change the flavor of particles and are therefore responsible for most of the particle decays.

The mechanism providing mass to particles in the SM is implemented through the spontaneous symmetry breaking introduced by the Higgs complex scalar field, which has a non-zero vacuum expectation value and generates the masses of the gauge vector bosons (W^+, W^-, Z^0) and all the fermions except neutrinos in the model [9]. This ultimate piece of the standard model, the Higgs boson,

was discovered in 2012 by the ATLAS and the CMS collaborations [10] [11]. However, there are several open questions suggesting that the SM cannot be the ultimate theory. These theoretical and observational issues do not represent inconsistencies or direct violation of SM, hence they do not point clearly to some other theory. Finding the first indications for New Physics (NP) beyond the SM is the main goal of particle physics today. To search for such indications, there are two complementary approaches, the first one are direct searches for new non-SM particles, an approach that has been successful since the invention of colliders. The second one is indirect searches for non-SM effects by comparing precise measurements with precise SM predictions. Indirect searches focuses on processes where new particles can contribute as virtual particles. In this field quark flavor dynamics offers a large variety and abundance of processes that is sensitive to non-SM dynamics. Thus, offering the most promising opportunities for indirect searches.
This thesis targets at making an essential contribution to the indirect searches at Belle II and is focused on the flavor dynamics of B mesons, in particular, on the phenomena related to the violation of the discrete charge-parity (CP) symmetry in this system.

1.0.1 Symmetries

Symmetries are fundamental in physics. They give rise to conservation laws, structure the formalism of theories and play a major role in our understanding of particle physics. A symmetry exists when a physical law is invariant under certain transformations. There are two types of transformations: continuous transformations, such as rotations or translations, and discrete transformations such as reflections or charge conjugations. The main subject of the thesis is related to two discrete symmetries, parity **P** and charge conjugation **C**, that are of fundamental importance in modern physics and defined as:

1. The parity transformation **P** defined as an inversion of the spatial coordinates at the origin, i.e $(x, y, z) \rightarrow (-x, -y, -z)$

2. The charge conjugation **C** transforms a particle into its anti-particle, and vice-versa : $X \rightarrow \overline{X}$.

Parity symmetry is conserved in strong and in electromagnetic interactions. The conservation of parity was assumed to be a universal law. However, in the mid 1950s Chen Ning Yang and Tsung-Dao Lee suggested that the weak interaction, might violate this law [12]. Indeed, parity violation of the weak interaction was confirmed in the famous ^{60}Co experiment by Chien Shiung Wu and collaborators [13], earning Yang and Lee the 1957 Nobel Prize in Physics. This and further experiments showed that only left handed neutrinos and right handed anti-neutrinos exist. In other words only one single helicity, i.e the projection of spin on the momentum direction, state exist for neutrinos. Hence, both C and P symmetries are violated.

Another experiment was performed later by Lederman [14], which allowed the observation of parity violation in charged pion decay. In this experiment the combined CP symmetry was proposed as an symmetry of nature representing the true symmetry between matter and antimatter where taking the mirror image of a physical system and replacing every particle with its antiparticle would result in exactly the same phenomena as before. The weak interaction seemed to violate P and C in a way that combined CP is conserved. However, in the mid 1960s, James Cronin, Val Fitch and coworkers provided an experimental demonstration that also CP symmetry is violated in certain weak processes [15], in particular, in decays of neutral kaons. Beside the discovery that CP symmetry violation, the quantitative value of the observed violation was intriguing. It took nearly ten years for the breakthrough in understanding how the observed CP violation can be connected with the emerging structure of the Standard Model (SM) of particle physics. In 1973 Makoto Kobayashi and Toshihide Maskawa pointed out that in the case of three quark generations the number of degrees of freedom in the SM naturally gives rise to the CP violating complex phase in the 3×3 quark mixing matrix, now known as the Cabibbo–Kobayashi–Maskawa (CKM) matrix [16] (note that in 1973 only the u, d, s quarks were known. [1] Indeed, two new quarks were discovered soon after, c (1974) and b (1977), and finally also t in 1995).

The CKM matrix is an elegant way to encode information on the relative strength of flavor changing weak decays, predicting correlations between different quark decays and CP violating observables.

In the following section we elaborate the origin of CP violation which is manifested in the electroweak interaction, starting by the mathematical description of the SM that is summarized by its Lagrangian:

$$\mathcal{L}_{SM} = \mathcal{L}_{kinetic} + \mathcal{L}_{Higgs} + \mathcal{L}_{Yuk}$$

The kinetic term describes the dynamics of the spinor fields ψ

$$\mathcal{L}_{kinetic} = i\overline{\psi}(\delta^{\mu}\gamma_{\mu})\psi,$$

where $\overline{\psi} \equiv \psi^{\dagger}\gamma^{0}$and the spinor fields ψ are the three fermion generations, each consisting of the following five presentations:

$$Q^{I}_{Li}(3,2)_{+1/6},\ \ \overline{u}^{I}_{Ri}(\overline{3},1)_{-2/3},\ \ \overline{d}^{I}_{Ri}(\overline{3},1)_{+1/3},\ \ L^{I}_{Li}(1,2)_{-1/2},\ \ \overline{\ell}^{I}_{Ri}(1,1)_{+1},$$

This notation means that $Q^{I}_{i}(3,2)_{+1/6}$ is $SU(3)_C$ triplet, left-handed $SU(2)_L$ doublet, with hypercharge $Y = 1/6$. The superscript I implies that the fermion

[1] The existence of a fourth quark, c, was suggested in 1964 for symmetry reasons related to strong interaction. In 1970, the GIM mechanism that suppresses Flavour Changing Neutral Currents (FCNC) was discovered, involving the introduction to the fourth quark flavour, charm, that was discovered soon after, in (1974).

fields are expressed in the interaction basis. The subscript i stands for the three generations.The subscript L indicates that only left handed fermions transform non-trivially under isospin, they belong to an isodoublet, while right handed fermions belong to an isosinglet.

The interaction terms are obtained by imposing gauge invariance by replacing the partial derivative with the covariant derivate

$$\mathcal{L}_{kinetic} = i\overline{\psi}(D^{\mu}\gamma_{\mu})\psi,$$

with the covariant derivative defined as

$$D^{\mu} = \delta^{\mu} + ig_s G_a^{\mu} L_a + igW_b^{\mu}\sigma_b + ig'B^{\mu}Y,$$

with L_a the Gell-Mann matrices and σ_b the Pauli matrices. G_a^{μ}, W_b^{μ} and B^{μ} are the eight gluon fields, the three weak interaction bosons and the single hypercharge boson, respectively.

Next, the W and Z bosons aquire their mass through the mechanism of spontaneous symmetry breaking. For this, the Higgs scalar field and its potential is added to the Lagrangian:

$$\mathcal{L}_{Higgs} = (D_u\phi)^{\dagger}(D^{\mu}\phi) - \mu^2\phi^{\dagger}\phi - \lambda(\phi^{\dagger}\phi)^2$$

where $\phi(x)$ is an isospin doublet:

$$\phi(x) = \begin{pmatrix} \phi^+ \\ \phi^0 \end{pmatrix}$$

The coupling of the Higgs to the gauge fields follows from the covariant derivative in the kinetic term. However, the interactions between the Higgs and the fermions, the Yukawa couplings, have to be added by hand and this is where CP violation can only arise from,

$$-\mathcal{L}_{Yukawa} = Y_{ij}^{d}\overline{Q_{Li}^{I}}\phi d_{Rj}^{I} + Y_{ij}^{u}\overline{Q_{Li}^{I}}\tilde{\phi}u_{Rj}^{I} + Y_{ij}^{\ell}\overline{L_{Li}^{I}}\phi\ell_{Rj}^{I}, \tag{1.1}$$

where the Higgs representation is ϕ and ($\tilde{\phi} = i\sigma_2\phi^*$)and $Y^{u,d,l}$ are $3\times$ 3 arbitrary complex matrices that operate in flavor space giving rise to couplings between different families, or quark mixing, and thus to the field of flavour physics.

The interesting part lies in the quark mass terms, which we further spell out:

$$\phi(x) = \begin{pmatrix} \phi^+ \\ \phi^0 \end{pmatrix} \xrightarrow{\text{sym.breaking}} \frac{1}{\sqrt{2}}\begin{pmatrix} 0 \\ \nu + h(x) \end{pmatrix},$$

the following mass terms for the fermion fields arise:

$$\begin{aligned} -\mathcal{L}^{quarks}_{Yukawa} &= Y^d_{ij}\overline{Q^I_{Li}}\phi d^I_{Rj} + Y^u_{ij}\overline{Q^I_{Li}}\tilde{\phi}u^I_{Rj} + h.c \\ &= Y^d_{ij}\overline{d^I_{Li}}\frac{\nu}{\sqrt{2}}d^I_{Rj} + Y^u_{ij}\overline{u^I_{Li}}\frac{\nu}{\sqrt{2}}u^I_{Rj} + h.c + interaction\ \ terms \\ &= M^d_{ij}\overline{d^I_{Li}}d^I_{Rj} + M^u_{ij}\overline{u^I_{Li}}u^I_{Rj} + h.c + interaction\ \ terms \end{aligned} \tag{1.2}$$

where the interaction terms of the fermion fields to the Higgs field, $q\bar{q}h(x)$ are omitted and

$$M^d_{ij} = (v/\sqrt{2})Y^d_{ij}\,,\ M^u_{ij} = (v/\sqrt{2})Y^u_{ij}, \tag{1.3}$$

are the 3×3 complex matrices that couple the left-handed component of each quark Q^I_{Li} with the rights-handed projections of all flavours. Thus, they are non-diagonal in the flavour basis. The mass eigenstates being the ones that propagate in space and time, the matrix M must be diagonalized:

$$M^d_{diag} = V^d_L M^d V^{d\dagger}_R$$

$$M^u_{diag} = V^u_L M^u V^{u\dagger}_R$$

Using the requirement that the matrices V are unitary ($V^{d\dagger}_L V^d_L = \mathbb{1}$) the Lagrangian can now be expressed as follows:

$$-\mathcal{L}^{quarks}_{Yukawa} = \overline{d_{Li}}(M^d_{ij})_{diag}d_{Rj} + \overline{u_{Li}}(M^u_{ij})_{diag}u_{Rj} + hc. + \ ... \tag{1.4}$$

where the matrices V are absorbed in the quark states, resulting in the following quark mass eigenstates:

$$\begin{aligned} d_{Li} = (V^d_L)_{ij}d^I_{Lj},\ \ u_{Li} = (V^u_L)_{ij}u^I_{Lj} \\ d_{Ri} = (V^d_R)_{ij}d^I_{Rj},\ \ u_{Ri} = (V^u_R)_{ij}u^I_{Rj} \end{aligned} \tag{1.5}$$

When expressing the SM Lagrangian in terms of the primed mass-eigenstate fields, the quark kinetic terms remain unchanged. The Z and γ boson couplings are also unaffected. As a consequence no flavour-changing neutral current (FCNC) processes are allowed at the tree level in the SM. On the other hand, in the part of the charged-current Lagrangian describing the couplings of the $W^{\pm}$ bosons to the left handed quarks, the transformation leaves the couplings unchanged by V^u_L, but not by $V^{u\dagger}_R V^d_L$:

$$\mathcal{L}_{kinetic,cc}(Q_L) = \frac{g}{\sqrt{2}}\overline{u^I_{iL}}\gamma_\mu W^{-\mu}d^I_{iL} + \text{h.c..} = \frac{g}{\sqrt{2}}\overline{u_{iL}}\gamma_\mu(V^u_L V^{d\dagger}_L)_{ij}d_{Lj}W^{-\mu} + \text{h.c..} \tag{1.6}$$

The unitary 3×3 matrix

$$V_{CKM} = (V^u_L V^{d\dagger}_L)_{ij}$$

is the Cabibbo-Kobayashi-Maskawa (CKM) mixing matrix [17] [16].
CP violation shows up in the complex Yukawa couplings. We examine once more the Yukawa part of the Lagrangian, $\mathcal{L}_{Yukawa}$, focussing on the charged current couplings in the basis of quark mass eigenstates:

$$\mathcal{L}_{kinetic,cc}(Q_L) = \frac{g}{\sqrt{2}}\overline{u_{iL}}\gamma_\mu V_{ij} W^{-\mu} d_{iL} + \frac{g}{\sqrt{2}}\overline{d_{iL}}\gamma_\mu V_{ij}^* W^{+\mu} u_{iL} \tag{1.7}$$

and the CP-transformed expression :

$$\mathcal{L}_{kinetic,cc}(Q_L) = \frac{g}{\sqrt{2}}\overline{d_{iL}}\gamma_\mu V_{ij} W^{+\mu} u_{iL} \frac{g}{\sqrt{2}}\overline{u_{iL}}\gamma_\mu V_{ij}^* W^{-\mu} d_{iL}. \tag{1.8}$$

Then we can conclude that the Lagrangian is unchanged if $V_{ij}^* = V_{ij}$.

The complex nature and the dimension of the CKM matrix, V_{CKM}, is the origin of CP violation in the Standard Model. In the following section, the properties of the CKM mixing matrix will be examined in detail.

1.1 The Cabibbo-Kobayashi-Maskawa Matrix

1.1.1 Unitarity traingle

In the general case of n quark families, the $2n^2$ real parameters of the complex $n \times n$ matrix V_{CKM}, can be reduced using properties of the V_{CKM} matrix and the quarks fields as follows.

1. The Unitarity condition ($V^\dagger V = \mathbb{1}$) reduces the number of parameters to n^2.

2. The phases of the quarks can be rotated freely, since the overall phase is irrelevant , 2n-1 relative quark phases can be removed.

These leaves V_{CKM} matrix with $2n^2 - n^2 - (2n-1) = (n-1)^2$ free parameters. These parameters can be divided into $n(n-1)/2$ Euler angles describing the rotations among the n dimensions, leaving $\frac{1}{2}(n-1)(n-2)$ irreducible phases that turn out to be 0 for $n = 1$ and 2 for $n = 3$. As Kobayashi and Maskawa noticed, this irreducible phase in a three-generation model would be the origin of all CP violation in the SM. The bottom and the top quark were discovered in 1977 and 1994 respectively. In 2008 Kobayashi and Maskawa were awarded the Nobel prize for the discovery of the origin of the broken symmetry which predicts the existence of at least three families of quarks in nature.

Looking again at the consequences of the unitarity condition for the V_{CKM} matrix:

$$V^\dagger V = V V^\dagger = \mathbb{1},$$

leads to the first following relations:

$$\begin{aligned} V_{ud}V_{ud}^* + V_{us}V_{us}^* + V_{ub}V_{ub}^* &= 1, \\ V_{cd}V_{cd}^* + V_{cs}V_{cs}^* + V_{cb}V_{cb}^* &= 1, \\ V_{td}V_{td}^* + V_{ts}V_{ts}^* + V_{tb}V_{tb}^* &= 1. \end{aligned} \tag{1.9}$$

These relations express the so-called weak universality, because it shows that the squared sum of the coupling strengths of the u-quark to the d, s and b-quarks is equal to the overall charged coupling of the c-quark (and the t-quark). In addition, we see that this sum adds up to 1, meaning that "there is no probability remaining" to couple to a 4^{th} down-type quark. Another three additional interesting equations arise from the unitary relation:

$$V_{ud}^*V_{us} + V_{cd}^*V_{cs} + V_{td}^*V_{ts} = 0, \tag{1.10}$$

$$V_{us}^*V_{ub} + V_{cs}^*V_{cb} + V_{ts}^*V_{tb} = 0, \tag{1.11}$$

$$V_{ud}^*V_{ub} + V_{cd}^*V_{cb} + V_{td}^*V_{tb} = 0. \tag{1.12}$$

Each term in these relations can be interpreted geometrically as a vector in the complex plane. This way, each equation above can be visualized as a triangle in the Argand plane, known as the unitarity triangles.

Since the first formulation of the V_{CKM} matrix, several parametrization have been proposed. One of such parametrization is the so called "Standard parametrization" proposed by Chau and Keung, and which is obtained as the product of three (complex) rotation matrices and a overall phase, where $c_{ij} = cos\theta_{ij}$, $s_{ij} = sin\theta_{ij}$ for $i < j = 1, 2, 3$, the θ_{ij} are the three rotation angles between families, and δ is the irreducible phase. The phase is chosen here to appear in the matrix describing the relation between the 1^{st} and 3^{rd} family.

$$V_{CKM} = \begin{pmatrix} c_{12}c_{13} & s_{12}c_{13} & s_{13}e^{-i\delta_{13}} \\ -s_{12}c_{23} - c_{12}s_{23}s_{13}e^{i\delta_{13}} & c_{12}c_{23} - s_{12}s_{23}s_{13}e^{i\delta_{13}} & s_{23}c_{13} \\ s_{12}s_{23} - c_{12}c_{23}s_{13}e^{i\delta_{13}} & -c_{12}c_{23} - s_{12}c_{23}s_{13}e^{i\delta_{13}} & c_{23}c_{13} \end{pmatrix} \tag{1.13}$$

Thanks to many experimental results, it has been established that a hierarchy among the matrix elements exists and that the matrix is dominated by its diagonal terms. In other words, transitions among quarks from different flavour doublets are suppressed, compared to the ones among quarks of the same generation. A useful parameterization that emphasizes the hierarchical, nearly diagonal structure of the matrix, is due to Wolfenstein.

$$V_{CKM} = \begin{pmatrix} V_{ud} & V_{us} & V_{ub} \\ V_{cd} & V_{cs} & V_{cb} \\ V_{td} & V_{ts} & V_{tb} \end{pmatrix} \simeq \begin{pmatrix} 1 - \frac{\lambda^2}{2} & \lambda & \lambda^3 A(\rho - i\eta) \\ -\lambda & 1 - \frac{\lambda^2}{2} & \lambda^2 A \\ \lambda^3 A(1 - \rho - i\eta) & -\lambda^2 A & 1 \end{pmatrix}$$

which is based on a Taylor development where λ is the expansion parameter,

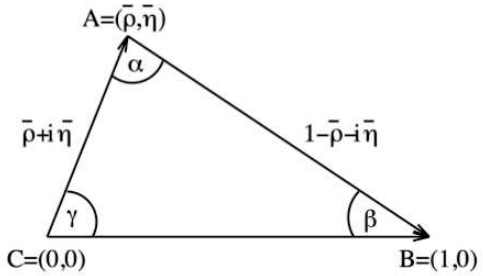


Figure 1.2

known to be small from experimental data, i.e $\lambda \simeq |V_{us}| \sim 0.22$ and A, ρ and η are all of order 1. In the Wolfenstein parametrization η contains the CP violation information. i.e CP violation occurs when η doesn't equal 0 and the triangles do not collapse to a line. To all orders in λ, the exact Wolfenstein parameterization can be defined as,

$$s_{12} \equiv \lambda \tag{1.14}$$

$$s_{23} \equiv \lambda^2 A \tag{1.15}$$

$$s_{13}e^{-i\delta} \equiv \lambda^3 A(\rho - i\eta) \tag{1.16}$$

This definition is useful because it allows an elegant improvement of the accuracy of the original Wolfenstein parameterization. In particular, up to the order $\mathcal{O}(\lambda^6)$, one get

$$V_{us} = \lambda, \;\; V_{cb} = \lambda^2 A, \;\; V_{ub} = \lambda^3 A(\rho - i\eta),$$

$$V_{td} = \lambda^3 A(1 - \bar{\rho} - i\bar{\eta})$$

$$Img(V_{cd}) = -\lambda^5 A^2 \eta, \quad Img(V_{ts}) = -\lambda^4 A\eta,$$

where

$$\bar{\rho} = \rho(1 - \frac{\rho^2}{2}), \bar{\eta} = \eta(1 - \frac{\lambda^2}{2})$$

One of the major physics goal of the B Factories was to improve the experimental constraints on the elements of V_{CKM}. Let us now return to the three relations 1.11-1.12 that give rise to the unitarity triangles. The first two triangles are related to the CKM matrix elements that governs the K^0-$\bar{K}^0$ and $B_s^0 - \bar{B}_s^0$ systems, respectively. For each of those triangles one side is much shorter than the other two, and so they almost collapse to a line. This would give an intuitive understanding of why CP violation is small in the leading K and B_s decays. On the other hand, for the triangle corresponding to the relation given in Equation 1.12, the sides are of the same order of magnitude. It is in this third triangle,related to the $B_d^0 - \bar{B}_d^0$ system, that the most exciting physics of CP violation lies. Indeed,

the openness of this triangle predicts large CP asymmetries in B_d decays. Note that all the unitarity triangles are equal in area. Equation 1.12 can be written in another way. Once divided by $V_{cd}V_{cb}^*$ it becomes

$$\frac{V_{ud}V_{ub}^*}{V_{cd}V_{cb}^*} + 1 + \frac{V_{td}Vtb^*}{V_{cd}V_{cb}^*} = 0.$$

In this convention one of the side of this triangle is aligned to the real axis of the Argand plane. The resulting pictorial representation is a unitarity triangle whose apex is determined by the ρ and η parameters, or equivalently, the irreducible phase (see Figure 1.2). In this representation, the lengths of the sides are given by

$$\overline{CB} = 1, \tag{1.17}$$

$$\overline{AB} = \left|\frac{V_{td}V_{tb}^*}{V_{cd}V_{cb}^*}\right| = \sqrt{(1-\bar{\rho})^2 + \bar{\eta}^2} = \frac{1}{\lambda}\left|\frac{V_{td}}{V_{cb}}\right|, \tag{1.18}$$

$$\overline{AC} = \left|\frac{V_{ud}V_{ub}^*}{V_{cd}V_{cb}^*}\right| = \sqrt{\bar{\rho}^2 + \bar{\eta}^2} = (1 - \frac{\lambda^2}{2})\left|\frac{V_{ub}}{V_{cb}}\right|, \tag{1.19}$$

while the angles are given by (quoting both notation with (α, β, γ) and $(\phi_1, \phi_2, \phi 3)$)

$$\phi_2 = \alpha = arg\left(\frac{V_{td}V_{tb}^*}{V_{cd}V_{cb}^*}\right) \tag{1.20}$$

$$\phi_1 = \beta = arg\left(\frac{V_{td}V_{tb}^*}{V_{cd}V_{cb}^*}\right) = arctan\left(\frac{\bar{\eta}}{1-\bar{\rho}}\right) \tag{1.21}$$

$$\phi_3 = \gamma = arg\left(\frac{V_{ud}V_{ub}^*}{V_{cd}V_{cb}^*}\right) = arctan\left(\frac{\bar{\eta}}{\bar{\rho}}\right) \tag{1.22}$$

$$\pi = \alpha + \beta + \gamma \tag{1.23}$$

These parameters have been measured in various B decay modes by independent experiments. The SM description of CP violation can be tested by analysing these measurements and checking if the apex of the triangle coincides, as expected in the SM, among the various measurements. The current experimental status of these parameters are summarized in Figure 1.3. In the next chapter, we shall focus on these measurements, especially the angle β. We will also explore the sensitivity to New Physics of one observation of CP violation.

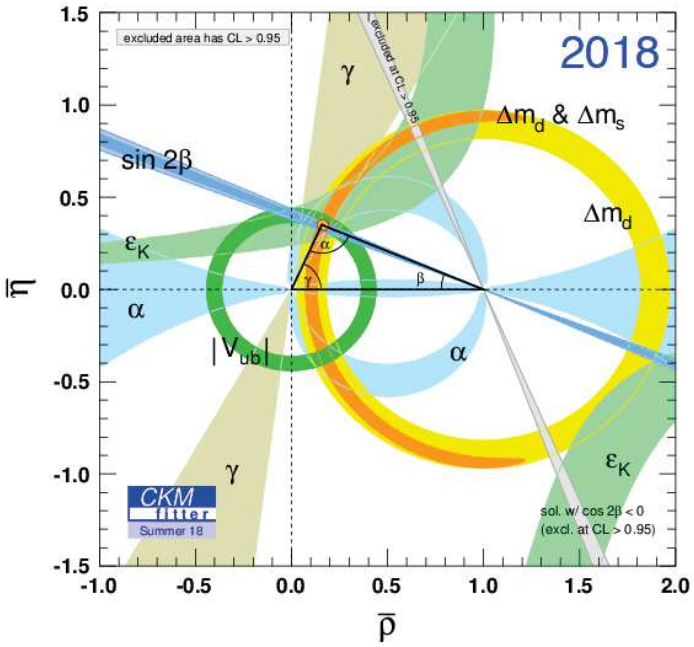


Figure 1.3: Experimental constraints of the unitarity traingle in $\overline{\rho} - \overline{\eta}$ plane, results of the most updated extrapolations from the CKM Fitter group (ICHEP 2018 conference) are shown [18].

CHAPTER 2

Mixing and CP violation in neutral B meson

This chapter presents the quantum mechanical properties of the neutral B^0 meson system, which are model independent. These properties are related to CP violation observables, and use features of the flavor and weak-interaction structure of the Standard Model. Three kinds of CP violation resulting from different processes, are distinguished allowing to extract different CP-violating quantities. The connection of these quantities with new physics in $b \to s\,\gamma$ transitions is discussed, finalizing with a summary of the previous experimental results for the CP-violating parameters for the two radiative B^0 decays channels analysis presented in this thesis.

2.1 Mixing of neutral B meson

A neutral meson state and its CP conjugate decay due to weak interactions. In order to describe the neutral meson system it is important to distinguish between different representations. On one hand, the neutral meson can be described by two flavor eigenstates, each with a definite quark content, which are useful for understanding particle production and decay processes. On the other hand, the neutral meson can be described by the two eigenstates of the Hamiltonian(mass eigenstates), with definite mass and lifetime, which are the states that propagate in space and time. Mass eigenstates are not flavor eigenstates, and so

flavor eigenstates get mixed as they propagate. Since CP is broken in the SM, the mass and CP eigenstates can differ.

The phenomenon of mixing, referring here to the process where a neutral meson turns into its antiparticle via a process involving two charged currents, has been observed in kaons [19], B_d and B_s mesons [20], and also, D mesons [21].

Let us now consider an arbitrary combination of the neutral B-meson flavor eigenstates [1]

$$|\psi(t)\rangle = a(t)|B^0\rangle + b(t)|\bar{B}^0\rangle \tag{2.1}$$

Its time evolution is given by the Schrödinger equation with the effective Hamiltonian $\mathcal{H}$

$$i\hbar\frac{\partial}{\partial t}|\psi(t)\rangle = \mathcal{H}|\psi(t)\rangle, \tag{2.2}$$

Where in the $|B^0\rangle, |\bar{B}^0\rangle$ basis,

$$|\psi(t)\rangle = \begin{pmatrix} a(t) \\ b(t) \end{pmatrix} \tag{2.3}$$

$$\mathcal{H} = M - \frac{i}{2}\Gamma = |\psi(t)\rangle = \begin{pmatrix} M_{11} - \frac{i}{2}\Gamma_{11} & M_{12} - \frac{i}{2}\Gamma_{12} \\ M_{21} - \frac{i}{2}\Gamma_{21} & M_{22} - \frac{i}{2}\Gamma_{22} \end{pmatrix} \tag{2.4}$$

$\mathcal{H}$ is composed of the mass matrix M and the decay matrix Γ, both of which are 2×2 hermitian matrices. Assuming the CPT theorem valid , the following relations hold :

$$M_{21} = M_{12}^* \;\;,\;\; \Gamma_{21} = \Gamma_{12}^* \;\;,\;\; M_{11} = M_{22} = M \;\;,\;\; \Gamma_{11} = \Gamma_{22} = \Gamma \tag{2.5}$$

that means that the mass and the total decay width of particles and antiparticles are identical. The off-diagonal terms, M_{12} and Γ_{12} are particularly important in the discussion of CP violation, since $arg(M_{12}/\Gamma_{12}) = 0$ would be implied in the case of CP conservation. The mass matrix of the Hamiltonian describes the oscillation between flavor eigenstates, where the diagonal terms in M are dominated by the flavor eigenstates masses, and the off-diagonal ones represent the transitions via virtual intermediate states. The diagonal terms of the decay part of the Hamiltonian describe the flavor eigenstates decays to different final states, i.e $B^0 \to f$ and $\bar{B}^0 \to \bar{f}$, while the off-diagonal terms describe the transition via real intermediate states. Figure 2.1 shows the Feynman diagrams representing the weak transitions between B^0 and $\bar{B}^0$ via second order transitions (transitions with two quarks), also referred to as B^0 $\bar{B}^0$ mixing. Such transitions lead to the inclusion of the three up-type quarks in the loop, since all of them couple via a CKM factor that is proportional to λ^6. However, integration of the internal degrees of freedom (the up-type quarks and the W) yields an expression that weighs the contribution of each quark by the ratio of its mass to that of the weak boson. Thus, the up and charm quarks contribution are suppressed,

[1] The flavor eigenstates of the neutral B meson are defined as $B^0 = \bar{b}d$ and $\bar{B}^0 = \bar{d}b$

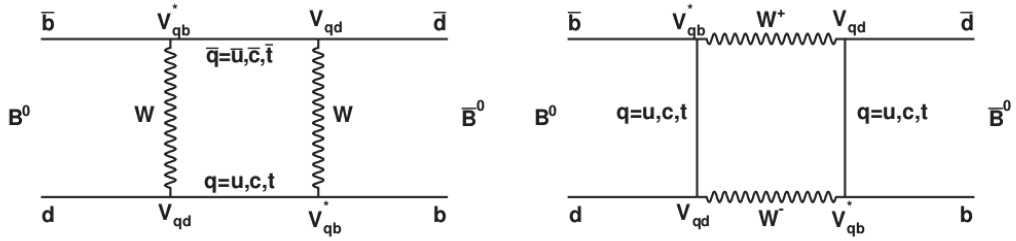


Figure 2.1: Diagrams describing the mixing phenomenon for neutral B_d mesons via a second order weak transition, usually called box diagrams.

and an evaluation of the corresponding CKM factors readily gives a phase of $(V_{td}V_{tb}^*)^2 \sim e^{-i2\beta}$. In other words, the B^0 states that oscillate into $\overline{B}^0$ pick up an extra -2β phase, called the mixing angle, with respect to the B^0 states that do not oscillate. This phase is measurable whenever both flavors decay to a common state.

Diagonalizing the Hamiltonian, $\mathcal{H}$, leads to the expression of the mass eigenstates of the neutral B meson system, which consist in a superposition of the B^0 and $\overline{B}^0$ flavor eigenstates, such as

$$|B_L\rangle = p|B^0\rangle + q|\overline{B}^0\rangle \tag{2.6}$$
$$|B_H\rangle = p|B^0\rangle - q|\overline{B}^0\rangle \tag{2.7}$$

where the index $L(H)$ refers to the lighter (heavier) mass eigenstates of the neutral and the complex coefficients p and q are constrained by a normalization condition

$$|p^2| + |q^2| = 1. \tag{2.8}$$

We can find p and q by solving

$$\begin{pmatrix} M - \frac{i}{2}\Gamma & M_{12} - \frac{i}{2}\Gamma_{12} \\ M_{12}^* - \frac{i}{2}\Gamma_{12}^* & M - \frac{i}{2}\Gamma \end{pmatrix} \begin{pmatrix} p \\ q \end{pmatrix} = \lambda_{H,L} \begin{pmatrix} p \\ q \end{pmatrix} \tag{2.9}$$

where $\lambda_\pm$ are the eigenvalues of the mass-decay matrix,

$$\lambda_L = m_L - \frac{i}{2}\Gamma_L,\ \lambda_H = m_H - \frac{i}{2}\Gamma_H \tag{2.10}$$

where m_L and m_H are the masses of the eigenstates $|B_L\rangle$ and $|B_H\rangle$, respectively. It is useful then to define the average mass and width as well as the mass and width differences between the neutral B^0 mesons as :

$$M = \frac{m_H + m_L}{2} = M_{11} = M_{22}\,,\ \ \Delta m_d \equiv M_H - m_L \tag{2.11}$$
$$\Gamma = \frac{\Gamma_L + \Gamma_H}{2} = \Gamma_{11} = \Gamma_{22}\,,\ \ \Delta\Gamma \equiv \Gamma_H - \Gamma_L \tag{2.12}$$

where Δm_d is positive and represents the mixing frequency of the $B^0\overline{B}^0$ oscillation. Finally one can derive the ratio of $\frac{q}{p}$ from Equation 2.9.

$$\frac{q}{p} = \pm\sqrt{\frac{M_{12}^* - \frac{i}{2}\Gamma_{12}^*}{M_{12} - \frac{i}{2}\Gamma_{12}}}. \tag{2.13}$$

For the B_d mesons, the difference in width, $\Delta\Gamma_{B_d}$, is expected to be small compared to Γ_{B_d}. Also one should note that $\Delta\Gamma_{B_d} \ll \Gamma_{B_d}$ is model-independent. Moreover, the B_d oscillation parameter x_d has been measured [22]

$$x_d \equiv \frac{\Delta m_d}{\Gamma_{B_d}} = 0.77 \pm 0.004 \tag{2.14}$$

which implies then, model-independently, $\Delta\Gamma_{B_d} \ll \Delta m_d$. As a consequence one gets

$$|\Gamma_{12}| \ll |M_{12}|, \tag{2.15}$$

$$|q/p| \sim 1. \tag{2.16}$$

Consider a state which is created at time $t = 0$ as an initially pure $B^0(\bar{B}^0)$, denoted as $|B^0(t)\rangle|\bar{B}^0(t)\rangle$, The time evolution of these states can be described by the eigenvalues of the Hamiltonian and the q and p parameters such as:

$$|B^0(t)\rangle = g_+(t)|B^0\rangle + \frac{q}{p}g_-(t)|\bar{B}^0\rangle, \tag{2.17}$$

$$|\bar{B}^0(t)\rangle = g_+(t)|\bar{B}^0\rangle + \frac{q}{p}g_-(t)|B^0\rangle, \tag{2.18}$$

where

$$g_\pm(t) = e^{-iMt-\frac{1}{2}\Gamma t}[1 \pm e^{-i\Delta m_d t+\frac{1}{2}\Delta\Gamma t}] \tag{2.19}$$

Here Γ fulfills the natural role of decay constant, $\Gamma = 1/\tau$. The sign of Δm_d is by definition positive, but the sign of $\Delta\Gamma$ has to be determined experimentally. Due to the close values of the B^0 meson lifetime, $\tau = (1.52 \pm 0.004)$ ps [23] and the frequency of oscillation, $\Delta m_d = (0.507 \pm 0.005)\,\text{ps}^{-1}$, the amplitude for the mixing process is rather large. Accordingly, the integrated probability of oscillation is sizable [22].

$$\chi = \frac{(\tau\Delta m_d)^2}{2(1 + (\tau\Delta M)^2} = 0.1878 \pm 0.0024 \tag{2.20}$$

which confers mixing a prominent role. An immediate consequence are the large time dependent CP asymmetries that mixing produces, and that are discussed in the next section.

2.1.1 Decay rates

In this section we extend the formalism of neutral meson oscillations, and include the subsequent decay of the meson to a final state f. We consider the following decay amplitudes:

$$A_f = \langle f|H|B\rangle \quad \overline{A}_f = \langle f|H|\overline{B}\rangle \tag{2.21}$$

and define the complex parameter λ_f

$$\lambda_f \equiv \frac{1}{\overline{\lambda}_f} \equiv \frac{q}{p}\frac{\overline{A}_f}{A_f} \tag{2.22}$$

The general expression for the time dependent decay rates is,

$$\Gamma_{B\to f(t)} = |\langle f|H|B(t)\rangle|^2 \tag{2.23}$$

which gives us the probability that the state $|B\rangle$ at $t = 0$ decays to the final state f at time t. Now and using the Equations 2.17 and 2.18 we find:

$$\Gamma_{B\to f}(t) = |A_f|^2\left(|g_+(t)|^2 + |\lambda_f|^2|g_-(t)|^2 + 2Re[\lambda_f g_+^*(t)g_-(t)]\right) \tag{2.24}$$

$$\Gamma_{\overline{B}\to f}(t) = |A_f|^2\left|\frac{p}{q}\right|^2\left(|g_-(t)|^2 + |\lambda_f|^2|g_+(t)|^2 + 2Re[\lambda_f g_+(t)g_-^*(t)]\right) \tag{2.25}$$

The terms proportional $|A|^2$ are associated with decays that occurred without oscillation, whereas the terms proportional to $|A|^2(p/q)^2$ are associated with decays following a net oscillation. The third terms, proportional to $Re(g^*g)$ are associated to the interference between the two cases. Following this, the next session we will state the classification between the various types of CP violation that may occur.

2.2 CP violation in the B meson system

To measure CP violation, we measure the asymmetry between the decays of $B^0(t)$ and $\overline{B}^0(t)$ into the CP conjugated final states, f and $\overline{f}$. This asymmetry depends on time, since decay rates also depend on time,

$$a_f(t) = \frac{\Gamma(B^0(t)\to f) - \Gamma(\overline{B}^0(t)\to \overline{f})}{\Gamma(B^0(t)\to f) + \Gamma(\overline{B}^0(t)\to \overline{f})} \tag{2.26}$$

CP violation in decay

CP violation in decay or called "Direct CP violation", which occurs when the amplitude for a decay and its CP conjugate have different magnitudes It is independent of B^0 $\overline{B}^0$ mixing effects and can also be observed in the decays of

charged B mesons.

CP violation in mixing

Another type of CP violation comes from the fact that the neutral B mesons can oscillate into its CP conjugate as described in Sec 2.1. Indeed, since the mass and the CP eigen-states are not identical in the case of neutral B mesons, an asymmetry arises between their transition probabilities, $B \to \bar{B}^0$ and $\bar{B}^0 \to B^0$ One can express these differences using the convention-free quantity $|q/p|$, since it is related to the matrix elements $M_{12} - \frac{i}{2}\Gamma_{12}$ and $M_{12}^* - \frac{i}{2}\Gamma_{12}^*$ describing $B \to \bar{B}^0$ and $\bar{B}^0 \to B^0$ transitions, respectively. If CP was conserved, the relative phase between $M_{12}$and Γ_{12} would vanish, then Equation 2.13 implies

$$|q/p| \neq 1 \implies CP \text{ violation}. \tag{2.27}$$

This type of CP violation is also known as indirect CP violation. It has been first observed in 1964 [15] in the neutral kaon system. In the B_d^0 system, effects of CP violation in mixing is expected to be small, $\mathcal{O}(10^{-4})$ and very negligible with respect to the sensitivity of the B factories, thus making $|q/p| \sim 1$ a good approximation.

CP violation in the interference between decays with and without mixing

Finally, another possibility for CP violation, also referred to as CP violation in mixing and decay, it occurs whenever

$$\Gamma(B^0 \to f) \neq \Gamma(\bar{B}^0 \to f) \tag{2.28}$$

where f is a final state accessible to both B^0 and $\bar{B}^0$, a condition that is satisfied if the final state f is a CP eigenstate. In this case CP violation arises as a consequence of the interference between the amplitudes $(AB^0 \to f_{CP})$ and $A(B^0 \to \bar{B}^0 \to f_{CP})$. Note that CP violation in the mixing and in the decay of $K^0 - \bar{K}^0$ system [15], had also been observed before the start of the B Factories.

A quantity similar to the one used to measure purely direct CP violation, given in Equation 2.26, could be applied in order to measure the CP violation here. However, in this case the flavor of neutral B mesons is not straight forward to determine since, precisely, their flavors change over time. At the B Factories, the flavor determination is facilitated by the fact that the B mesons are produced from the decay of the $\Upsilon(4S)$ resonance, i.e. $\Upsilon(4S) \to B^0\bar{B}^0$, therefore forming an entangled pair of mesons. Such states are predicted by quantum mechanics by the famous "EPR paradox" [24], where at instant t, the probability of one of the mesons to be a particle equals the probability for the other meson to be an antiparticle. Thus, if it is possible to determine the flavor of one of the B mesons at time t, the flavor of the other meson can be inferred to be the opposite at that exact same instant, and evolves afterwards independently by means of mixing. This is experimentally known as flavor tagging, which will be discussed more in

section 4.1.1. The flavor of a given B meson, B_{rec}, is determined from the observation of the other meson, called B_{tag}, decaying into a state that unambiguously determines its flavor. A precise measurement of the time elapsed between the two decays, Δt is also required in order to account for the probability for a given B meson state to oscillate. With these considerations, the CP asymmetry can be defined in a time dependent way:

$$a_{CP}(\Delta t) = \frac{\Gamma(B_{tag=B^0}(\Delta t) \to f_{CP}) - \Gamma(B_{tag=\bar{B}^0(\Delta t)\to f_{CP}})}{\Gamma(B_{tag=B^0}(\Delta t) \to f_{CP}) + \Gamma(B_{tag=\bar{B}^0(\Delta t)\to f_{CP}})} \tag{2.29}$$

In the case where no experimental biases are taken into account, such as the probability of the wrongly determining the flavor of the B_{tag} meson called mistagging, (which will be developed more later in the section), the amplitudes for the processes $B^0\,(\Delta t) \to f_{CP}$ and $\bar{B}^0\,(\Delta t) \to f_{CP}$ are given by:

$$A_{f_{CP}} = \langle f_{CP}|H|B^0\rangle \tag{2.30}$$

$$\overline{A}_{f_{CP}} = \langle f_{CP}|H|\bar{B}^0\rangle \tag{2.31}$$

First we can simplify the decay rates in Equation 2.24 and 2.25 by taking into account $\Delta\Gamma \ll \Gamma$ and the definition of λ_f and $\overline{\lambda}_f$ in Equation 2.22

$$\Gamma(B^0(t) \to f_{CP}) \propto e^{-\Gamma t}|A_{f_{CP}}|^2 \left[1 + \frac{1-|\lambda_{f_{CP}}|^2}{1+|\lambda_{f_{CP}}|^2}\cos(\Delta M t) - \frac{2Im\lambda_{f_{CP}}}{1+|\lambda_{f_{CP}}|^2}\sin(\Delta M t)\right] \tag{2.32}$$

$$\Gamma(\bar{B}^0(t) \to f_{CP}) \propto e^{-\Gamma t}|A_{f_{CP}}|^2 \left[1 - \frac{1-|\lambda_{f_{CP}}|^2}{1+|\lambda_{f_{CP}}|^2}\cos(\Delta M t) + \frac{2Im\lambda_{f_{CP}}}{1+|\lambda_{f_{CP}}|^2}\sin(\Delta M t)\right] \tag{2.33}$$

then the asymmetry in Equation 2.26 takes the form

$$a_{CP}(\Delta t) = \mathcal{S}\sin(\Delta m_d \Delta t) + \mathcal{A}\cos(\Delta m_d \Delta t) \tag{2.34}$$

where

$$\mathcal{S} = \frac{2Im\lambda_{f_{CP}}}{1+|\lambda_{f_{CP}}|^2}, \quad \mathcal{A} = \frac{|\lambda_{f_{CP}}|-1}{|\lambda_{f_{CP}}|+1} \tag{2.35}$$

Remembering that

$$\lambda_{f_{CP}} = \frac{q}{p}\frac{\overline{A}_{f_{CP}}}{A_{f_{CP}}} \tag{2.36}$$

and $|\frac{q}{p}| \sim 1$, we can see from Eqs. 2.34 and 2.35 that CP violation occurs in the case where

$$\lambda_f \neq 1 \tag{2.37}$$

Note that in both cases of CP violation in decay and of CP violation in mixing the previous relation is verified for $\frac{\overline{A}_{\bar{f}}}{A_f} \neq 1$ and $\frac{q}{p} \neq 1$ respectively. However in

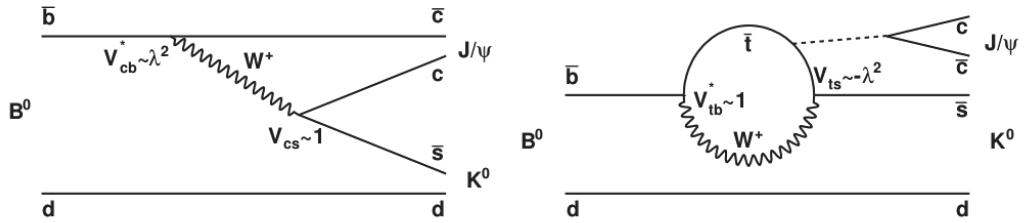


Figure 2.2: Feynman diagrams for the amplitudes contributing to the $B^0 \to J/\psi K_S^0$ decay. Left: Tree level diagram. Right: Penguin diagram, where the contribution of the light, u and c, quarks have been neglected. The dotted line corresponds to the exchange of three gluons, necessary to produce a $c\bar{c}$ pair.

this present case, even if $\frac{\overline{A}_{\overline{f}}}{A_f} = \frac{q}{p} = 1$, CP violation could still occur through

$$|\lambda_{fcp}| = 1, \;\; Img(\lambda_{fcp} \neq 0) \tag{2.38}$$

If there is only one SM contribution to the amplitudes A_f and $\overline{A}_{\overline{f}}$, the expectations are that $\mathcal{S} = -\eta_{CP} sin(2\beta)$, where the factor η_{CP} accounts for the CP eigenvalue of the final state. and $\mathcal{A} = 0$. Deviations from that imply the existence of unaccounted amplitudes that, depending on the characteristics of the mode, could originate from theoretical uncertainties in the Standard Model contributions, or could be an indication of physics beyond the SM.

2.3 CP violation in b $\to$ s γ transitions

2.3.1 Trees and Penguins

In a quantum field theory, on which is based the SM, in order to describe a given decay process, one needs to include all the possible contributing amplitudes. Each amplitude does not necessarily contribute at the same level, thus it is useful to apply a hierarchical ranking. It often happens that only the two first-order contributions to the total amplitude are sufficient to make theoretical predictions that are precise enough to be compared to experimental results. For instance, in the so-called "golden mode" $B^0 \to J/\psi K_S^0$ in which the final state is a CP eigenstate that makes it sensitive to CP violation in mixing and decay, not only one amplitude is allowed. One of the contributing amplitudes, in which the W boson is emitted and absorbed by the same quark line, is called a "loop" or, more often, a "penguin" diagram, whereas the other, is said to be a "tree-level", or simply "tree", diagram, both amplitudes sown in Figure 2.2. In the penguin diagram, the internal loop, which is formed by the W boson and a combination of up-type quarks, is dominated by the top quark due to its large mass compared to up and charmed quarks. In the hypothetical presence of new physics, new heavy particles could traverse the loop and provide new CP-odd phases that could dramatically enhance (or suppress) the amplitude [25]. As shown in Figure 2.3 candidates for such particles are for instance charged Higgs or squarks

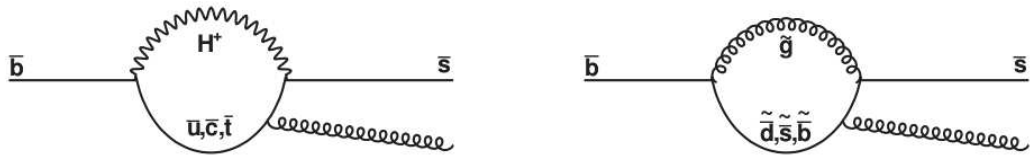


Figure 2.3: Diagrams demonstrating the potential for new physics sensitivity in $b \to s$ penguin diagrams.

and gluinos from a super symmetric model(SUSY) [26], an example of NP models that bring extra source of flavor violation.

In the considered example, the CKM factors in both amplitudes carry the same phases, as can easily be seen thanks to the powers of λ and phases that have been written next to the CKM terms on the figure. However, as in many other decays, the penguin diagram is suppressed compared to the tree diagram [27], which have SM couplings. Thus, SM contributions in the loop dominates over possible effects from non-SM couplings and a clean interpretation for the time-dependent asymmetry is obtained: $a_{CP}(\Delta t) = \sin(2\beta)\sin(\Delta m_d \Delta t)$. The measurement of CP violation in this channel constitutes one of the main achievements of the B Factories. In a general way, tree diagrams are usually cleaner in their theoretical interpretation than penguin diagrams. However, in some specific transition modes, the tree diagrams can be suppressed compared to penguin diagrams, as it is the case for $b \to s$ transitions. Furthermore, since SM parameters are now well constrained, any deviations due to unknown physics should be small compared to SM predictions. Such modes are therefore particularly interesting in the indirect search for new physics at the electroweak scale, due to the absence of a tree contribution which could overshadow effects from possible new physics. They are also complementary to direct searches performed in high-energy colliders such as in hadronic colliders like the LHC.

2.3.2 Photon polarization in radiative B^0 decays

Study of FCNC processes(flavor-changing neutral current), such as $b \to s\gamma$ transitions, can provide strong constraints on NP(New Physics). In the SM, the Glashow-Iliopoulos-Maini (GIM) mechanism implies that FCNC processes are forbidden at the tree level and only occurs through a loop or box diagrams, where heavy virtual particles can propagate. Since the presence of such heavy particles influences the predicted values of physical observables, the study of $b \to s\gamma$ processes could reveal the existence of yet unknown particles introduced by NP models. The SM predicts that photons emitted in $b \to s\gamma$ decays are left-handed, up to small corrections of order m_s/m_b, while being right-handed in $\bar{b} \to \bar{s}\gamma$. In several models beyond the SM the photon in $b \to s\gamma$ acquires an appreciable right-handed component due to the exchange of a heavy fermion in

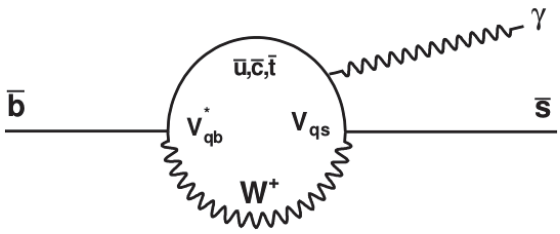


Figure 2.4: Feynman diagram of $\bar{b} \to \bar{s}\,\gamma$ transition in the SM. The loop being dominated by the top quark, the weak couplings are given by $|V_{qb}^*| \sim 1$ and $|V_{qs}| \sim \lambda^2$. In this transition since the $\bar{b} \to \bar{s}\gamma$ transition is a two-body back-to-back decay in the $\bar{b}$ rest frame, and due to the helicity conservation, the photon must be right-handed, while being left-handed in $b \to s\gamma$.

the electroweak loop process. In this context, many NP models models [28] [29] predicts right-handed component may be comparable in magnitude to the left-handed component, without affecting the SM prediction for the inclusive radiative decay rate, which motivates independent measurements of the photon helicity in several exclusive radiative decay modes.

In the SM, the quark level $b \to s\gamma$ vertex is given (without QCD corrections) by:

$$\bar{s}\Gamma_{\mu}^{b\to s\gamma} b = \frac{e}{(4\pi)^2}\frac{g^2}{2M_W^2} V_{ts}^* V_{tb} F_2 \bar{s} i\sigma_{\mu\nu} q^{\nu} (m_b P_R + m_s P_L) b, \tag{2.39}$$

where $q = q_b - q_s$ with q being the four-momenta of the b and s quarks, respectively, F_2 is the loop function, whose expression can be found in [30], V_{ts} and V_{tb} are the leading CKM matrix elements appearing in the loop diagram, and $\sigma_{\mu\nu}$ are the commutators of the Dirac γ 4×4 matrices. P_L and P_R are the projection operators defined as

$$P_L = \frac{1}{2}(1 - \gamma_5), \;\; P_R = \frac{1}{2}(1 + \gamma_5). \tag{2.40}$$

In Equation 2.39, the term proportional to m_b describes $b \to s\gamma_L$ transitions, while the term proportional to m_s describes $b \to s\gamma_R$ transitions. Therefore, due to the fact that the b quark is much heavier than the s quark (i.e. $m_s/m_b \sim 0.02$), the SM predicts that photons emitted in $b \to s\gamma$ decays are predominantly left-handed. In a similar manner, photons emitted in $\bar{b} \to \bar{s}\gamma$ decays are predominantly right-handed. Figure 2.4 shows the Feynman diagram of the quark level $b \to s\gamma$ transition in the SM.

2.4 Physical observables and experimental status

As the photon polarization is not directly measurable, there are different methods proposed to measure it in $b \to s\gamma$ processes. One of this methods, which is adopted in this thesis, is covered in this section.

2.4.1 Mixing-induced CP asymmetry

One way to probe the photon helicity is to perform an indirect measurement via a time-dependent CP asymmetry analysis in neutral B mesons. In the case of the radiative decay of a neutral B meson to a hadronic CP eigenstate f_{CP}, $B^0(t) \to f_{CP}\gamma$, where the B meson state is identified (tagged) as a B^0 (rather than a $\bar{B}^0$) a time $t = 0$, the time-dependent CP asymmetry is given by [3]

$$a_{CP}(t) = \frac{\Gamma(B^0(t) \to f_{CP}\gamma) - \Gamma(\bar{B}^0(t) \to f_{CP}\gamma)}{\Gamma(B^0(t) \to f_{CP}\gamma) + (\bar{B}^0(t) \to f_{CP}\gamma} \tag{2.41}$$

$$\simeq -\xi \sin(2\psi) \sin(\phi_M - \phi_L - \phi_R) sin(\Delta M t) \tag{2.42}$$

$$= \mathcal{S}_{f_{CP}} \sin(\Delta M t) \tag{2.43}$$

where $\mathcal{S}_{f_{CP}}$ is the mixing induced CP violation parameter, $\xi \equiv CP(f_{CP}) = \pm 1$ and

$$\Gamma(B^0(t) \to f_{CP}\gamma) = |M_L(t)|^2 + |M_R(t)|^2, \tag{2.44}$$

$$\Gamma(\bar{B}^0(t) \to f_{CP}\gamma) = |\overline{M}_L(t)|^2 + |\overline{M}_R(t)|^2, \tag{2.45}$$

with M_L and M_R corresponding to the total amplitude involving left-handed and right-handed photons, respectively. In order to obtain to obtain the second equation 2.42, both direct CP violation ($a_{f_{CP}}$) and the small width difference, compared to the mass difference between the B meson mass eigenstates, are neglected.

In Equation 2.42, $\sin(2\psi)$ parametrizes the relative amount of left-handed and right-handed photons and is defined as

$$\sin(2\psi) \equiv \frac{2|M_L M_R|}{|M_L|^2 + |M_R|^2}; \tag{2.46}$$

note that the phase ϕ_M is the one appearing in the $B^0\bar{B}^0$ mixing such as $\phi_M = 2\beta$ for B_d mesons and is almost zero for B_s mesons; $\phi_{L,R}$ are the relative CP-odd weak phases in the $b \to s\gamma$ process,

$$\phi_{L,R} = \sin^{-1}\left(\frac{Img(M_{L,R})}{|M_{L,R}|}\right) \tag{2.47}$$

In the SM, $\phi_{L,R}$ are predicted to be almost zero $\mathcal{O}(\lambda^4)$. Since the right-handed amplitude in suppressed in the SM, the time-dependent asymmetry is such as

$$a_{CP}^{SM}(t) \sim 0 \tag{2.48}$$

From this method, it appears that, although an observation of $a_{CP}(t) \neq 0$ would immediately indicate the existence of NP contributions, it is not possible to determine quantitatively the ratio M_R/M_L. Indeed $a_{CP}(t)$ measures a combination

of M_R/M_L and the CP violating phases in $b \to s\gamma$ as well as in $B\bar{B}$ mixing. Therefore in the case of an experimental result that would measure a deviation of $a_{CP}(t)$ from its predicted value in the SM, one can only fix the CP violating phases $\phi_{M,L,R}$ as given by several NP models in order to best describe the observed value of $a_{CP}(t)$.

Several exclusive radiative decay modes have been studied in time-dependent CP violation analyses. Two of such are, $B^0 \to K_S^0\pi^0\gamma$ and $B^0 \to K_S^0\pi^+\pi^-\gamma$. These analysis are very challenging in hadronic colliders, and the best results to date come from the B Factories.

2.4.2 Summary of previous experimental results for $B^0 \to K_S^0\pi^0\gamma$ and $B^0 \to K_S^0\pi^+\pi^-\gamma$

In $B^0 \to K_S^0\pi^0\gamma$ decay process, where the SM predicts $\mathcal{S} \simeq -0.028$ [3], both BABAR and Belle have have performed measurements of the mixing-induced CP asymmetry parameter $\mathcal{S}$, and reported $\mathcal{S}_{B^0\to K_S^0\pi^0\gamma} = -0.78 \pm 0.59 \pm 0.09$ [6] and $\mathcal{S}_{B^0\to K_S^0\pi^0\gamma} = -0.10 \pm 0.31 \pm 0.07$ [4],respectively. where $B^0 \to K_S^0\pi^0\gamma$ goes through K^{*0} (892). Also measurement of the direct CP asymmetry in BABAR and Belle was performed, $\mathcal{A}_{B^0\to K_S^0\pi^0\gamma} = -0.36 \pm 0.33 \pm 0.05$ and $\mathcal{A}_{B^0\to K_S^0\pi^0\gamma} = -0.2 \pm 0.2 \pm 0.06$ respectively.

In $B^0 \to K_S^0\pi^+\pi^-\gamma$ decay process, where the SM predicts $\mathcal{S} \simeq$ [], both BABAR and Belle have have performed measurements of the mixing-induced CP asymmetry parameter $\mathcal{S}$, and reported $\mathcal{S}_{B^0\to K_S^0\pi^+\pi^-\gamma} = 0.14 \pm 0.25 \pm 0.03$ [7] and $\mathcal{S}_{B^0\to K_S^0\pi^+\pi^-\gamma} = -0.09 \pm 0.27^{+0.04}_{-0.07}$ [5],respectively. where $B^0 \to K_S^0\pi^+\pi^-\gamma$ goes through K^{*0} (892). Also measurement of the direct CP asymmetry in BABAR and Belle was performed, $\mathcal{A}_{B^0\to K_S^0\pi^+\pi^-\gamma} = -0.39 \pm 0.2^{+0.03}_{-0.02}$ and $\mathcal{A}_{B^0\to K_S^0\pi^+\pi^-\gamma} = -0.2 \pm 0.2 \pm 0.06$ respectively. From the list of previous measurements and results, one can see that the measurements where statistically limited for the mixing-induced CP asymmetry parameter $\mathcal{S}$ and for the direct CP asymmetry $\mathcal{A}$ results in good agreement with the SM prediction and the assumption made in Equation 2.42.

CHAPTER 3

SuperKEKB and Belle II project

There is two ways to look for physics beyond the standard model: one way is to reach high energies in order to produce directly new heavy particles, which is known as energy frontier. Other option is to look for new physics by performing precision measurements at lower energy with the highest liuminosity, known as intensity frontier. The Large Hadron Collider at CERN, is an example of the energy frontier while electron-positron colliders at B factories belong to the intensity frontier type. B factories have been crucial in the the past decades to establish the CKM mechanism and to provide precision tests of the SM as well as a complementary tool to the energy frontier experiments for the search of forbidden processes and new physics. The Belle II detector operating at the SuperKEKB, an electron-positron collider, at KEK laboratory in Tsukuba (Japan), aims to explore new physics with an unprecedented luminosity. SuperKEKB will provide Belle II a data set which is 50 times that data provided by its predecessor KEKB [31]. In the following section 3.1 an overview of the SuperKEKB accelerator and its upgrades with respect to its predecessor KEKB is given, then a description of the different Beam-Induced Backgrounds due to the high luminosity and design upgrades are listed. The last part of the chapter 3.2 will be devoted to the description of three running phases of SuperKEKB, concluding with the luminosity prospects and future plans for the accelerator, which plays a crucial role in determining the physics reach of Belle II.

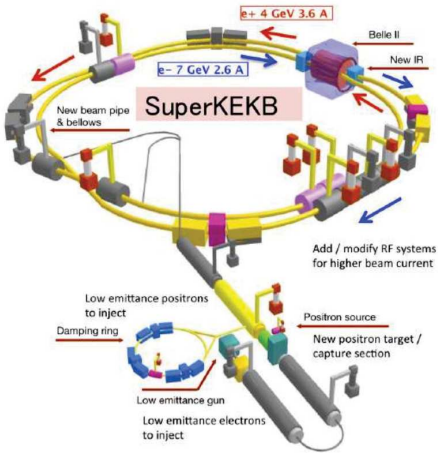


Figure 3.1: A schematic representation of the SuperKEKB asymmetric energy e^+e^- collider

3.1 SuperKEKB

SuperKEKB is an asymmetric e^+e^- collider, that operate at a center-of-mass energy $\sqrt{s}$ = 10.58 GeV, corresponding to the invariant mass of the Y(4S) resonance, which is a bound state (bottomonium) of the beauty quark and its antiparticle, the antiquark $\bar{b}$. Beauty hadrons can be produced both in e^+e^- interactions and in hadronic interactions, for instance in $p\bar{p}$ collisions at 13 TeV at LHC that offers a large cross-section and a full spectrum for beauty mesons and baryons, while electron-positron colliders provide instead an extremely clean environment and a well and coherent initial state Y(4S). The asymmetric e^+e^- B factory concept at SuperKEKB, uses different energies for the electron and positron beams so that the Y(4S) acquires a boost in the laboratory frame and the decay products are pushed forward in the direction of the electron beam. Figure 5.29 shows an schematic overview of SuperKEKB collider. It consists of two major parts: the linear accelerator and the storage ring which includes the high energy ring (HER) for electrons and the low energy ring (LER) for the positrons. The electrons and positrons were brought to collision at the interaction point (IP), which was surrounded by the Belle II detector. SuperKEKB aims at a peak lumonisity of $8 \times 10^{35} cm^{-2} s^{-1}$ which correspond to an integrated luminosity of 50 ab^{-1}, 40 times larger then the luminosity produced at Belle as shown in table 3.2. However to reach the designed instantaneous luminosity, several modification were needed, these modifications are listed in more in the following section 3.1.1 as well as in table 3.2.

The event rate for a process with cross section σ can be written

$$\frac{dN}{dt} = \mathcal{L} \, . \, \sigma,$$

where the instantaneous luminosity $\mathcal{L}$ for two beams with a gaussian profile of horizontal and vertical size σ_x and σ_y, is given by:

		KEKB	SuperKEKB
Energy (LER/HER) [GeV]	E	3.5/8.0	4.0/7.0
Instantaneous luminosity [$10^{34}\,\mathrm{cm}^{-2}\mathrm{s}^{-1}$]	$\mathcal{L}$	2.11	80
Beam current (LER/HER) [A]	I	1.64/1.19	3.60/2.62
Vertical Beta Function at IP [mm]	β_y^*	5.9/5.9	0.27/0.41
Beam crossing angle [mrad]	ϕ_c	22 ($\approx 1.3°$)	83 ($\approx 4.8°$)
Horizontal beam size at IP [μm]	σ_x^*	90	9
Vertical beam size at IP [nm]	σ_y^*	1900	60
Boost	$\beta\gamma$	0.425	0.287

Figure 3.2: Fundamental parameters at KEKB and at SuperKEKB

$$\mathcal{L} = \frac{N_{e^+} N_{e^-} f_c}{4\pi\sigma_x\sigma_y} \,.\, R_L,$$

where N_{e^+} and N_{e^-} are the number of particles in a positron and in an electron bunch, f_c is the bunch crossing frequency, and R_L is a reduction factor accounting for a geometrical effects associated with the finite crossing angle and the bunch length. To increase the luminosity, SuperKEKB increases the beam currents $I_{e^+/e^-} \propto N_{e^-/e^+} f_c$ by a factor of two compared to KEKB, reduces the beam sizes:

$$\sigma_{x/y}(s) = \sqrt{\epsilon_{x/y}\beta_{x/y}(s)},$$

where ϵ is the emittance being a constant of motion along the orbit. β the is the so called "β function " that describes the displacement of a particle beam due to oscillations in the transverse plane xy with respect to its nominal trajectory in a given point (s) along the orbit. To achieve a low emittance, a new damping ring 5.29 was constructed for the positrons in order to cool their transverse momentum since it is easier to achieve a low emittance with a higher energy, the beam energies at SuperKEKB were modified to further reduce the emittance of the positron beam.

3.1.1 Nano-beam scheme

The major new feature in the luminosity upgrade of SuperKEKB is the so-called nano beam scheme, where the vertical β function at the IP "interaction point" called β_y^* is squeezed down to about 0.3 mm (around 20 times smaller than at KEKB) resulting in a vertical beam size of only $\sigma_y^* \simeq 60$ nm. To achieve the nano beam scheme, the beam crossing angle ϕ_c was increased by about a factor of four compared to KEKB. Figure 3.3 shows a schematic view of the beam crossing at KEKB and at SuperKEKB. At SuperKEKB, the size of the interaction region in z-direction σ_z is about 20 times smaller than at KEKB. As stated before, the important running mode of SuperKEKB is at the Y(4S), and due to the asymmetric beam energies, the Y(4S) is produced with a boost $\beta\gamma$. The boost depends on the

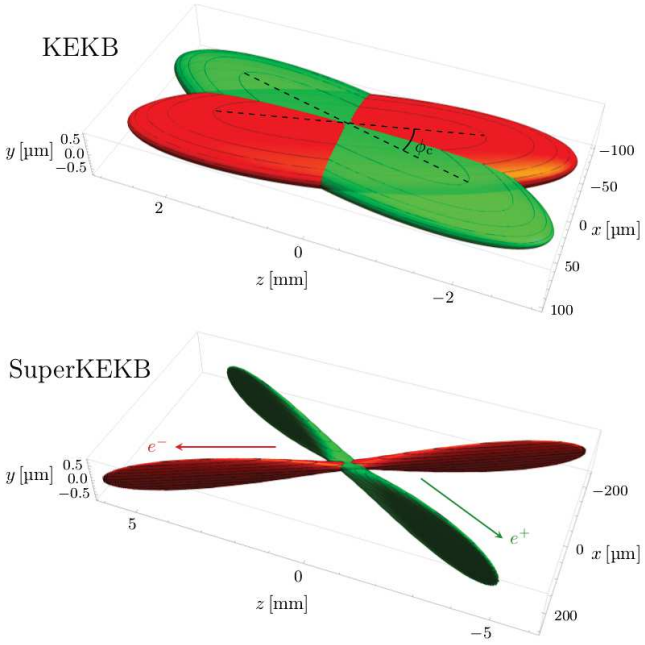


Figure 3.3: Schematic view of the beam crossing at KEKB (top) and at SuperKEKB (bottom). The crossing angle is shown in the top. The beam directions are shown in the bottom scheme. The size of the interaction region in z-direction at KEKB was around 10 mm, while at SuperKEKB it is around 0.5 mm

beam energies and on the crossing angle between them. For a head-on collision, the boost magnitude is given by:

$$\beta = \frac{p_{\Upsilon(4S).c}}{E_{\Upsilon(4S)}} = \frac{E_{HER} - E_{LER}}{E_{HER} + E_{LER}}, \quad \gamma = \frac{1}{\sqrt{1-\beta^2}}, \quad \beta\gamma = \frac{E_{HER} - E_{LER}}{\sqrt{s}}$$

The boost $\beta\gamma$ is needed to measure the time difference between the decays of the two B^0 mesons produced at the $\Upsilon(4S)$, since $\Delta t = \Delta z/\beta\gamma$. Due to the reduction of the beam-energy asymmetry at SuperKEKB, the boost is reduced by factor $\simeq 2/3$ compared to KEKB. Thus, the average distance Δl (Δz in boost direction) of about 190 μm at KEKB, is reduced to about 130 μm at SuperKEKB. To avoid a deterioration of the Δt resolution, the new Belle II experiment has a novel vertex detector, as well as improved track and vertex reconstruction algorithms.

The new SuperKEKB upgrades needed to increase the luminosity has a counter effect appearing in the beam-induced background, this type of background is crucial in Belle II and increases relatively with the nano-beam scheme upgrade.

3.1.2 Beam-Induced Background

The tracking detectors presented in 3.3.1, rely on the measurement of the deposited energy of the produced final state particles. Unfortunately, in most of these detectors the number of background-induced energy depositions is equal

or even higher than the number of the ones coming from signal. Thus background hits mimic typical signal hits and pose a severe problem for event reconstruction. Most of these background sources are unique to e+ e- colliders and cannot be seen at proton colliders like LHC experiments.The main beam background sources at SuperKEKB are five.

Tousckek scattering Touschek scattering is highly enhanced due to the nanobeam scheme technique and squeezed beams since it is proportional to the beam size. It is an intra-bunch process which consists in the coulomb scattering of two particles within the same bunch, implying as result a shift in the energies of the particles involved, one getting higher and one decreasing of the same amount, therefore deviating from the nominal energy and from the stable orbit. Fortunately, the rate of Touschek scattering also scales with the beam energy E as E^{-3} so increasing the energy of the LER compared to Belle is a first countermeasure.

Beam-gas scattering The interactions of the accelerated bunches with residual gas in the beam-pipe causes bremsstrahlung and Coulomb scattering. This changes the kinematic properties of the beam particles making them deviate from their nominal values. These disturbed particles hit the walls of the beam pipe or the surrounding magnets producing secondary showers of particles, which can leave measurable traces in the detector.

Synchrotron Radiation (SR) This type is emitted due to the transversal acceleration of the electrons and positrons in the storage ring, the leptons emit synchrotron radiation with high intensity. This is especially the case in the interaction region with its strong focusing magnets. The produced photons have an energy high enough to cause ionization in the detector material of the inner detector layers.

The last two types of beam background are generated during collisions and are luminosity dependent.

Radiative-Bhabha process The cross section for Bhabha interactions of the accelerated electrons and positrons is much enhanced compared to the one of signal processes. These radiative processes do not only produce collision events, which must be filtered out by the trigger system, but also produce photons and beam particles with non-nominal kinematic properties. The production rate is proportional to the luminosity, therefore it is expected to be 40 times the background level at KEKB.

Electron-Positron Pair Production The most severe background for the innermost detector layer are low-momentum electron-positron pairs resulting from the two-photon processes in e+ e- $\rightarrow$ e+ e- e+ e- reactions. The number of background energy depositions on just the first PXD layer in one readout can go up to 14000 hits with the planned luminosity compared to around ten anticipated

signal hits.

3.2 SuperKEKB commissioning and running phases

The commissioning of SuperKEKB has been carried out in three phases. In **Phase 1** (2016) the accelerator rings have been commissioned without the final focusing system at the interaction point and without the Belle II detector. The main goals were to ensure beam background levels are safe to install Belle II, to provide feedback for the accelerator optimization on how the machine parameters affect background levels and validate the simulation studies on expected backgrounds, which are crucial to reliably estimate detector lifetimes. These goals have been achieved thanks to the BEAST II detectors system [32], composed of eight sub-detectors devoted to the measurement of many properties of SuperKEKB backgrounds at the interaction region. During the **Phase 2** commissioning (2018), the final focusing and the positron damping ring were in place, together with the Belle II detector, except for the vertex detector, Instead of the final PiXel Detector (PXD) and Silicon Vertex Detector (SVD) (detailed in section 3.3.1 3.3.1), a special cartridge was installed close to the interaction region, which included the BEAST II detectors and one single ladder per each layer of PXD and SVD detectors, a schematic view is provided in Figure 3.5. The goal for such a configuration was double: to commission the machine by measuring beam background rates and providing feedback for accelerator tuning and to ensure the radiation safety of Belle II to run at higher luminosity with the final vertex detector installed, without damaging it. Also, additional collimators to protect the Belle II detector have been installed before the beginning of the data taking. The first physics collisions were detected on April 26^{th}, 2018. The data taking continued until Ju ly 2018, with a maximum achieved instantaneous luminosity of $5 \times 10^{33} cm^{-2} s^{-1}$ and a total integrated luminosity of $\sim 0.5\,\text{fb}^{-1}$ as shown in Figure 3.4. These data have been used to prove the understanding of the detector through performance measurements and several rediscoveries. In **Phase 3**, the full vertex detector has been installed and started taking data with Belle II in March 2019. The application of the final nano-beam scheme will allow to reach the design luminosity and collect in the next ten years 50 ab^{-1}. Thanks to such a dataset a very rich physics program can be pursued [33], which includes the measurement of time dependent CP violation and CKM parameters with a precision below the current threshold of percent level, hadronic charmless B decays and direct CP violation, charm and quarkonium physics, τ and low multiplicity studies as well as the search for physics beyond the SM through precision measurements.

3.3 Belle II detector

The Belle II detector is described in detail in the Technical Design Report [34]. In this section, a general description of each sub-detector is listed. The changes and

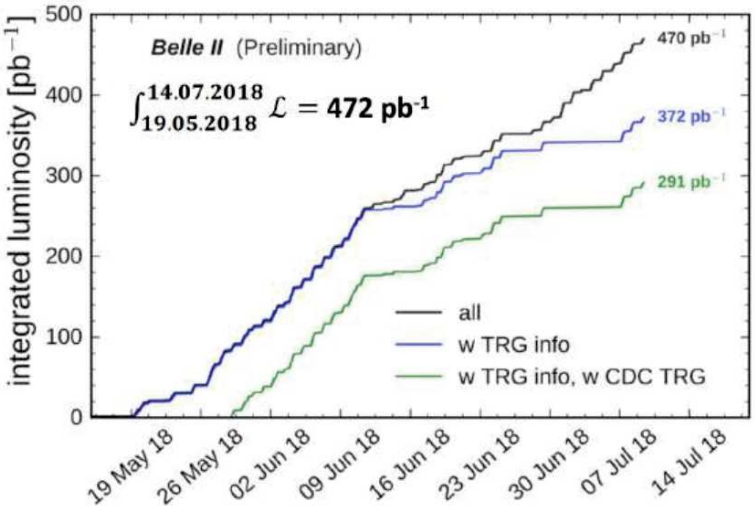


Figure 3.4: The integrated luminosity collected during the **Phase 2** run, April-July 2018, is shown. The various curves refer to the trigger information available for each data set

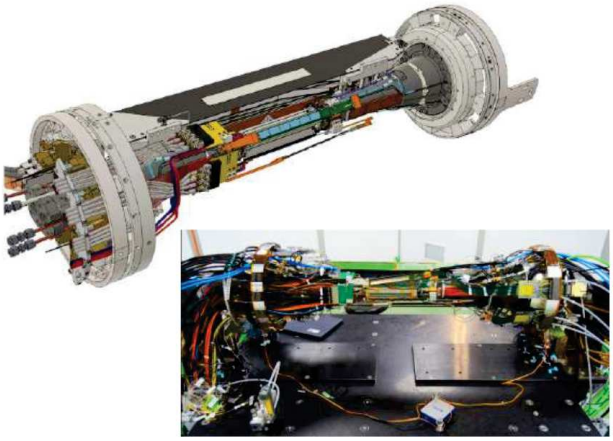


Figure 3.5: The CAD rendering and a real image of the vertex detector cartridge and BEAST II monitoring setup installed during **Phase 2** at the interaction point.

improvements with respect to the Belle detector are highlighted. In Section 3.3.5 the Belle II trigger system is described, followed by an overview of the software framework developed to analyze the collected data sets

Compared to Belle, the Belle II detector will be taking data at an accelerator with a 40 times higher luminosity, and thus has to be able to operate at 40 times higher event rates, as well as with backgrounds rates higher by a factor of 10 to 20 [34]. To maintain the excellent performance of Belle II, the critical issue will be to mitigate the effects of higher background levels, thus the following modification to the Belle II detector design are taken:

- Inner part of the vertex silicon strip detector, next to the beam pipe, is replaced by a two-layer silicon pixel detector based on DEPFET technology with a very light material budget, these layers are placed at a smaller radius ($r_{L1} = 14, r_{L2} = 22$) then in Belle.
- Silicon strip detector are placed after the pixel detector and occupies a larger radius (140 mm) than in Belle (88 mm), the silicon strips readout is based on APV25 chips which have a shorter shaping time with respect to Belle VA1TA chips to cope with higher background
- Central drift chamber tracking device extends to a larger radius (1130 mm) then Belle (880 mm). It has smaller drift cells than the one used in Belle to be able to operate at high event rates with increased background.
- New particle identification devices, both in the barrel and in the endcaps, are more compact and highly performing, exploiting the Cherenkov image detection method and a very fast readout electronics.
- Electronics of the electromagnetic calorimeter is replaced with a fast waveform-sampling circuit.
- The two layers of the barrel part and in the end-caps of the muon and K_L detector, Resistive Plate Chambers (RPCs) are replaced by scintillators readout with wavelength shifting fibers and Silicon Photomultiplier (SiPM). field after a discharge significantly reduces the detection efficiency under such background fluxes.
- New data acquisition system for handling the higher event rate is provided.

These changes will permit a better Belle II performance in several way, especially the vertex resolution improvement due to the two innermost pixel layers, a better reconstruction efficiency for the K_S decaying to charged pions, which is crucial for the analysis of the golden mode $B \to J/\psi K_s$ exploited in CP asymmetries measurements. In addition, the new particle identification devices ensure a better pion/kaon separation in the whole kinematics range of the experiment. Finally, a better performing electronics for the calorimeter readout reduces the pile up, improving missing energy measurements.

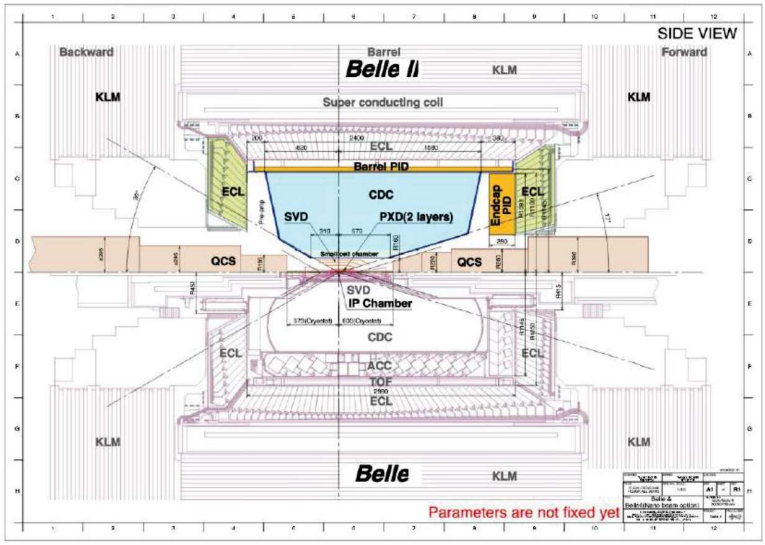


Figure 3.6: Illustration showing in the top, the upgraded Belle II detector as designed in the Belle II Technical design report [34], while in the bottom, the longitudinal view of the old Belle detector is shown.

3.3.1 Tracking Detectors

Pixel vertex detector

The PiXel Detector (PXD) [35] concept implemented at Belle II is based on the DEPFET (Depleted Field Effect Transistor) technology which allows to have very thin pixel (50 μm) with readout electronics moved outside the acceptance region covering a polar angle from 17 $^\circ$ to 155 $^\circ$, therefore reducing the material budget that contributes to the multiple scattering.

DEPFET is a semiconductor detector concept able to combine detection and amplification in one device. A DEPFET pixel consists in a p-channel MOSFET structure integrated onto a fully depleted silicon substrate. The MOSFET has an internal gate where the electrons generated when a charged particle passes through the device are collected. The internal gate modulates the current at readout time allowing the detection of the collected charge.

The DEPFET sensors are organized into planar modules, the ladders, which compose the two layers of the PXD, with radii respectively of 14 and 22 mm. The sensitive lengths of each layer are determined by the acceptance requirements of the detector: a polar angular coverage from 17 $^\circ$ to 155 $^\circ$ ensured. The total amount of pixels composing the PXD is around 8 million organized into arrays. Each DEPFET pixel represents a cell, a monolithic structure with internal amplification, therefore much thinner than other devices which need additional amplification. Pixel sizes have to meet the vertex resolution requirement (20 μm), and the thinning feasibility, resulting in a 50 $\times$ 50 μm^2 and 50 $\times$ 75 μm^2 cells respectively for the inner and outer layers. Another challenging requirement is the short frame readout time, that is achieved by splitting the readout on both sides of the pixel matrix and introducing high level of parallelization

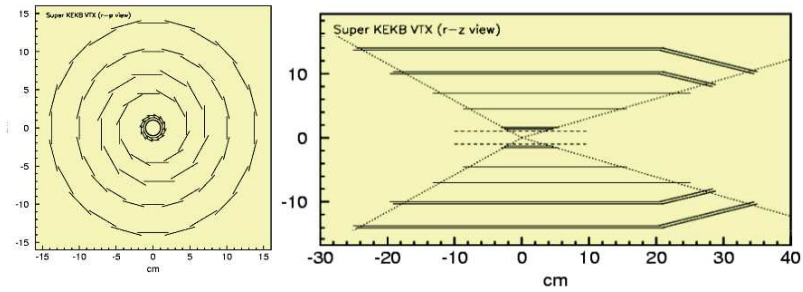


Figure 3.7: A shematic view of the Belle II vertex detector, two pixelated layers and four layers with silicon strip sensors

(a four-row simultaneous readout): the processing time for each pixel row is of order 100 ns, and all the 1600 rows can be read in a total frame time of 20 μs. The sensors are finally mounted on the supporting structure which is able to slide on the beam pipe to accommodate for thermal expansion.

Vertex installation in Phase 3

For the early Phase 3 started in March 2019 after the installation of the vertex detector, due to problems in the assembling of the PXD ladders, only half of the designed PXD has been installed, consisting in the full first layer and 2 ladders of the second one. The PXD installation is expected to be finalized in 2021.

Silicon strip vertex detector SVD

The SVD is composed of four layers as shown in Figure 3.9, each SVD layer is composed of ladders of 2-5 DSSD (double-sided silicon strip detector) sensors. The four layers are called L3-6. Ladders in the outer layers have more sensors to cover the wider acceptance region. To effectively cover the asymmetrically wide acceptance in the forward side, most forward (FW) sensors in L4-6 ladders are slanted towards z-axis. The ladders are placed in a windmill shape to make the edges overlap. To ensure a good performance of the Silicon Vertex detector in Belle II, it requires a very low material budget and short shaping time in order to limit the occupancy.The former issue is solved by adopting the largest possible silicon wafers and equipping the forward region with trapezoidal slanted sensors, while for the latter, the solution came from inheriting the APV25 chips first used in the tracker of the CMS experiment (LHC), equipped with 128 channels each and a shaping time of 50 ns. Moreover, the multi-peak operational mode of the APV25, where six (or three) consecutive samples along the shaping curve are recorded with each trigger, ensures a time resolution of order of 3 ns. The excellent SVD performance results in a innermost layer occupancy smaller than 1 %.

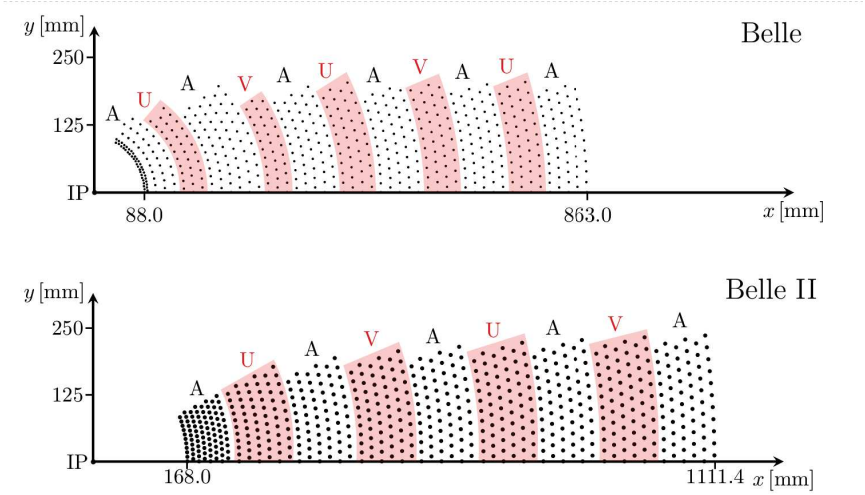


Figure 3.8: Layer configuration of the CDC at Belle (top) and at Belle II (bottom). The letter A stays for axial superlayers; the letter U for stereo superlayers with positive stereo angle; and the letter V for stereo superlayers with negative stereo angle.

Central Drift Chamber

The central tracking device, surrounding the SVD system, completing the tracking system. The (CDC) has three main functions. It contributes to the reconstruction of charged particles and momentum measurements. Second, It helps in particle identification thanks to the measurements of the energy loss ($\frac{dE}{dx}$) due to ionization in the gas volume. Finally, it provides reliable trigger signals for charged particle events. As stated is section 3.3, CDC in Belle II covers a larger radius and has 56 layers of sense wires, 6 more than the Belle CDC.

The CDC is a large gaseous detector (50 % He, 50 % C2H6) composed by 56 cylindrical layers of wires, divided into 9 super-layers. The super-layers alternate between stereo and axial layers; the stereo angles goes from 45 mrad to 74 mrad and is necessary to measure the z coordinate of the tracks. Super-layer are composed of six layers, except for the innermost one which has two additional layers with smaller drift cells to cope with the higher background level. The radial cell size is 10 mm for the innermost super-layer and 18.2 mm for the other super layers. The chamber inner radius is 16 cm while the outer radius is 113 cm, . The CDC provides a position resolution of 2 mm in z and 100 μ m in r. The resolution on the energy loss by a charged particle inside the chamber is 12 %, for incoming particles at $\theta = 90\,^{\circ}$. There are three main structural components of the CDC: a carbon-fiber inner cylinder, two aluminum end plates and a carbon-fiber outer cylinder. The two aluminum end plates have complex conical shapes to maximize acceptance avoiding excessive rates coming mainly from Bhabha scattering.

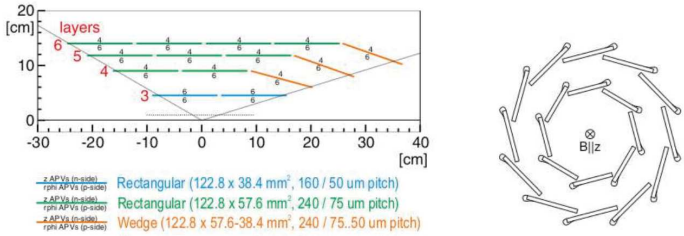


Figure 3.9: Left: Schematic view of the SVD longitudinal section, showing the sensors geometry for each layer and the number of APV25 chips on each side of the sensors. Right: the windmill structure of the inner sensors, with the Origami concept applied on the upper edge of silicon modules, is shown.

3.3.2 Particle Identification devices

Particle identification is crucial for distinguishing between final state hadrons and leptons, Belle II has a PID system consisting of the TOP (Time Of Propagation counter) in the barrel region and the ARICH (The Aerogel Ring-Imaging Cherenkov counter) detector located at the forward endcap.

Time Of Propagation counter (TOP)

The Time-Of-Propagation counter conceptual overview is shown in Figure 3.10. It consists of array of quartz bars surrounding the outer wall of the CDC divided into 16 modules in ϕ in the baseline geometry. When a charged particle passes through the quartz bars, Cherenkov radiation is emitted with an angle θ_C with respect to the direction of motion of the particle. The cosine of θ_C is inversely proportional to the speed of the particle and to the refractive index of the material. Thus Cherenkov photons are emitted at different angles, depending on the mass of the incoming particle. The time of propagation of the Cherenkov photons internally reflected by a mirror at the forward end of the bars, is measured 3.11. The Cherenkov image is reconstructed from the 3-dimensional information provided by two coordinates (x, y) and precise timing, which is determined by micro-channel plate (MCP) PMTs at the end surfaces of the quartz bar.

The PID power is limited by the broadening of the time resolution due to the chromaticity of Cherenkov photons. To minimize the chromatic effect, we introduce a focusing system which divides the ring image according to the wavelength of Cherenkov photons. Figure 3.12 shows the schematic set-up. A focusing mirror is introduced at the end of the quartz bar. The PMT is aligned to measure the position of the photon impact in x and y. The cross section of the quartz bar is a rectangle, we can therefore expand the light trajectory into the mirror-image region and create a virtual readout screen. The TOP counter requires photo-sensors with a single photon time resolution of about 100 ps, which can be achieved with a 16-channel MCP PMTs specially developed for this purpose. For precision timing required in this type of counter, a custom-made waveform sampling read-out electronics is used. Note that for this identification method

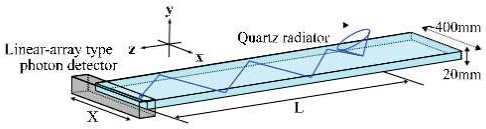


Figure 3.10: Conceptual overview of TOP counter

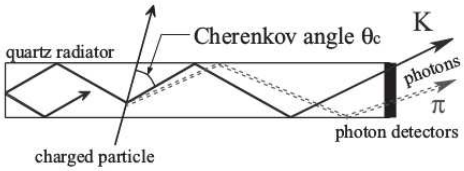


Figure 3.11: Schematic side-view of TOP counter and internal reflecting Cherenkov photons.

the starting (particle production) time has to be known with a precision of about 50 ps; this is indeed challenging, but was already achieved for the time-of-flight (TOF) counter of Belle.

The Aerogel Ring-Imaging Cherenkov counter

In the forward end-cap region, ARICH, a proximity focusing Cherenkov ring imaging detector with aerogel as Cherenkov radiator has been designed to separate kaons from pions over most of their momentum spectrum. It consists of 2 layers of aerogel producing Cherenkov photons, when a charged particle passes through its volume as shown in Figure 3.13, an expansion volume of 20 cm divides the aerogel tile from the photon detector surface and allows the Cherenkov photons to enlarge into rings. The array of position sensitive photon detectors provides single photon detection in a high magnetic field (1.5 T) with optimal resolution in two dimensions.

The main parameters describing the detector are the number of detected photons N_γ and the resolution on the Cherenkov angle σ_θ. Increasing the radiator thickness, the number of detected photons increases and the resolution per charged track improves as $\sigma_\theta/\sqrt{N_\gamma}$, but the angular resolution on the single photon (σ_θ) degrades due to the uncertainty of the emission point. Combining two layers with appropriately tuned refractive indices in order to have

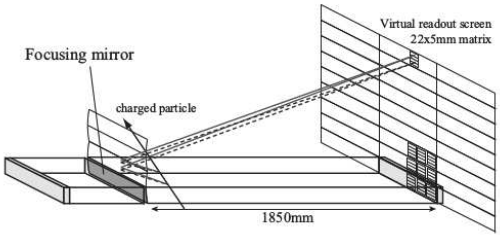


Figure 3.12: Schematic side-view of TOP counter and internal reflecting Cherenkov photons.

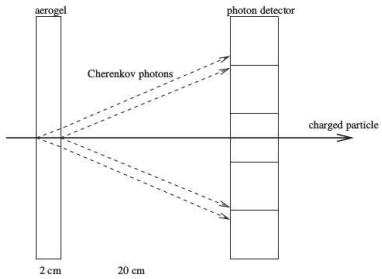


Figure 3.13: Proximity focusing ARICH - principle

two overlapping rings will reduce the spread due to the emission point uncertainty, achieving a resolution on the Cherenkov angle $\sigma_\theta \simeq 16$ mrad. The performance is optimized for charged tracks with momentum larger than 3.5 GeV/c, but no significant degradation is shown also for lower momentum tracks. A non-homogeneous aerogel radiator (Figure 3.13) has been devised, with a global acceptance covering the azimuthal angular region from 15 ° to 30 °. The proximity focusing technique is applied by choosing as upstream layer the aerogel with lower refractive index (n_1 = 1.046) and increasing the refractive index of the downstream layer (n_2 = 1.056). Studies have shown that a twice as thick layer of homogeneous aerogel radiator would provide the same number of photons, but with a worse resolution $\sigma_\theta \simeq 20$ mrad. The development of reliable photo sensors with good efficiency for single-photon detection in the high magnetic field is achieved with the Hybrid Avalanche Photo-Detectors (HAPD) by Hamamatsu Photonics. Finally, considering the studies on Cherenkov angle resolution and on average 12.7 detected Cherenkov photons as measured during for Phase 3, the precision achieved is

$$\sigma_{track} = \sigma_\theta / \sqrt{N_\gamma} \simeq 4.5 mrad.$$

In Figures 3.14 and 3.15 show the latest performances of the charged kaon and pion identification based on Phase 3 data. Precisely studies the binary likelihood ratio, defined as, $R_{K/\pi} = \mathcal{L}_K \ (\mathcal{L}_K + \mathcal{L}_\pi)$. The two figures shows the kaon/muon identification efficiency defined as:

$$\epsilon_K / \epsilon_\pi = \frac{\text{number of kaon(pion) tracks identified as kaon(pion)}}{\text{number of kaon (pion) tracks}} \tag{3.1}$$

while the π mis-identification rate (mis-ID rate) is defined as:

$$\pi \text{ mis-ID rate} = \frac{\text{number of pion tracks identified as kaon}}{\text{number of pion tracks}} \tag{3.2}$$

These figures shows good performances when comparing data with MC, simulated data.

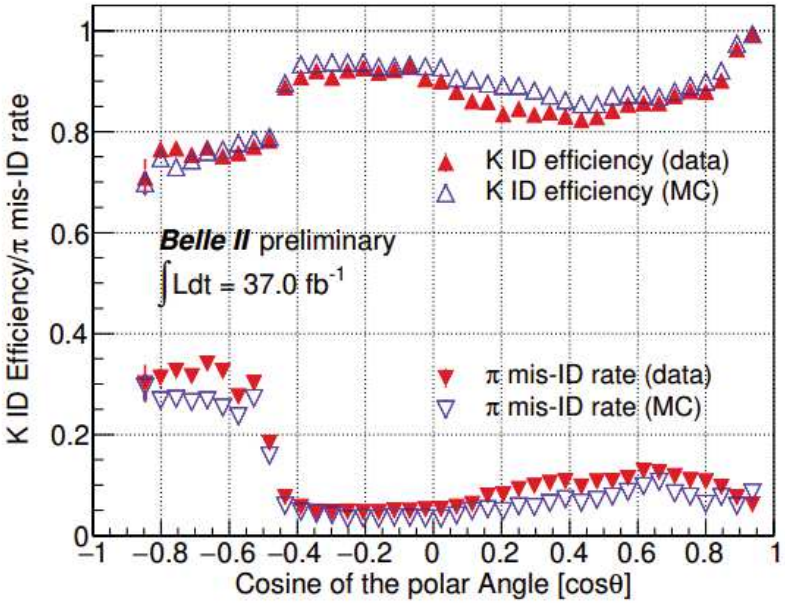


Figure 3.14: Kaon efficiency and pion mis-ID rate for the PID criterion $R_{K/\pi} > 0.5$ using the decay $D^{*+} \to D^0[K^-\pi^+]\pi^+$ in the bins of laboratory frame momentum of the tracks.

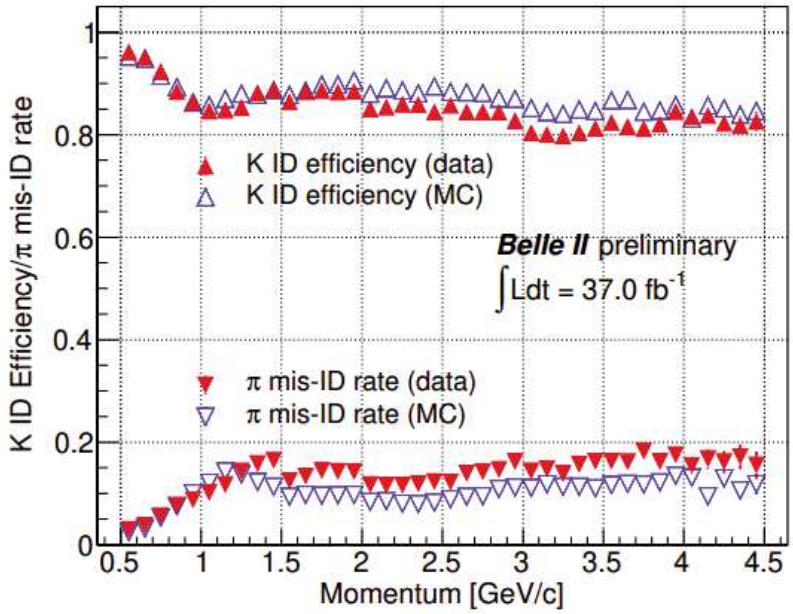


Figure 3.15: Kaon efficiency and pion mis-ID rate for the PID criterion $R_{K/\pi} > 0.5$ using the decay $D^{*+} \to D^0[K^-\pi^+]\pi^+$ in the bins of polar angle (laboratory frame) of the tracks.

3.3.3 Electromagnetic calorimeter

Since the tracking systems can only measure charged particles, an electromagnetic calorimeter (ECL) is needed to measure the energy deposition of the neutral photons using scintillating CsI(Tl) crystals. Neutral π^0 particles are measured via their decay into photons. By measuring the energy and the radiative energy deposition caused by bremsstrahlung for electrons and positrons, additional information is gained for particles which were already reconstructed by the tracking system. In addition, the calorimeter provides luminosity measurements, proper trigger signal generation refsec:trigger and together with the KLM 3.3.4 ensures K_L^0 detection. As for the structure of the ECL, a total of 8736 scintillator crystals cover a polar angle range of $\sim 12^\circ < \theta < 155^\circ$, with 6624 and 2112 divided between the barrel and end-caps, respectively. When ionising particles enter the scintillator crystals, their energy is absorbed and re-emitted in the form of photons, which are then detected via photo-diodes glued to each crystal. The same crystals have been inherited for the Belle II ECL, due to only minimal damage received during the run-time of KEKB. At present, the crystals are made of Thallium-activated Cesium Iodide, CsI(Tl), a scintillating material with a considerably large light output. The ECL electronics have also been significantly upgraded since Belle, with major improvements to the readout time achieved.

3.3.4 The neutral kaon and muon detector

Finally, the K_L^0 and μ detector, the outermost layer of the detector similarly sectioned into the barrel and endcap regions, is designed for the detection and identification of muons and neutral K_L^0 mesons. It is located outside of the superconducting solenoid used to provide the 1.5 T magnetic field to the detector, which occupies the space between the ECL and the KLM, as can be seen in Figure 3.6. The angular coverage of the KLM is comparable to that of the ECL with a $\sim 12^\circ < \theta < 155^\circ$ range in polar angle, and polyethylene sheets that shield the KLM from multiple backgrounds including neutrons produced from beam background processes. Resembling closely the successful Belle KLM, detector elements known as resistive plate chambers (RPCs) are wedged between 4.7 cm thick iron plates in the barrel.When hadrons deposit energy into the ECL or collide with the iron plates, they interact strongly such that a characteristic shower of secondary hadrons is produced. These traverse the iron plates and are detected by the RPCs via the charged hadrons present in the shower.Each RPC consists of two parallel electrode sheets made from an insulating substance known as float glass across which a high voltage is applied. Charged particles can ionize the gas between the electrodes, with electrons and ions accelerated to the anode and cathode, respectively. At the end-caps, however, RPCs are no longer optimal when contending with the higher luminosity beam background effects, and polystyrene scintillator strips are used in lieu of the RPCs within both the forward and backward end-caps.

Much like photons, neutral hadrons including K_L^0 mesons cannot be detected by the charged particle tracking sub-detectors, and are only able to deposit energy within the ECL and/or the KLM. Given this, clusters registered only in the KLM, or aligned clusters in both the ECL and KLM that cannot be matched to any charged particle track, strongly indicate the presence of a neutral hadron.

The nature of the momentum of the muons produced at Belle and Belle II is such that the muons are most often low ionizing, and can traverse the ECL and even the iron plates with minimal energy loss. As such, muons produce non-shower hits in the KLM that can be matched to tracks in the CDC. This provides a useful feature for the discrimination between muons and other charged hadrons, particularly pions, that do generate hadronic showers within the KLM. For high-purity samples of muons(for example from the reactions $e^+e^- \rightarrow \mu^+\mu^-(\gamma)$), it has been estimated that the barrel section of the KLM provides a μ -reconstruction efficiency of 89 % for particle momenta above 1 GeV/c.

3.3.5 Trigger

Although the number of particles in a single bunch is high, not every collision produces an interesting signature, especially not a B meson decay. The collision rate is dominated by elastic Bhabha scattering processes, which are not of interest for the physics studies performed on the Belle II data. As the high number of those physically uninteresting processes cannot be stored or transported and they are also not needed for later analyses, early filter stages on hardware and software are necessary. Additionally, the detector readout of the sub-detectors needs to be synchronized to make sure that each device records the data of the same collision event. The full readout chain is shown in Figure 3.16 More detailed information is stated in the following sections.

Detector Readout and Hardware Trigger

Belle II's online trigger (also called Level 1 or L1 trigger) system gathers many sub-trigger systems which provide information from various subdetectors, merged by the global reconstruction logic (GRL), whose output is sent to the global decision logic (GDL), responsible for issuing the trigger signal. The first combination of detector information is performed by the GRL and it is mainly based on the drift chamber trigger and on the ECL trigger. The CDC trigger finds and characterizes the tracks detected in the drift chamber. The 2D tracking basically follows the same implementation as Belle. The Belle II CDC detection improvement with the 3D tracking, which adds the information on the z-coordinate, allows to reject the most part of the background coming from Touchshek intra-bunch scattering. In fact, these scattering events show a large displacement in their z-position with respect to the nominal interaction region. The maximum 5 μs latency of the L1 trigger system requires a very fast z-vertex reconstruction, to be performed in no more than 1 μs, which is achieved thanks to neural networks techniques.

The calorimeter trigger system adopts two complementary trigger schemes: a total energy trigger and an isolated cluster counting technique, the former being sensitive to events with high electromagnetic energy deposition, the latter to multi-hadronic physics events with low energy clusters and/or minimum ionizing particles. Moreover, the ECL trigger is able to recognize the back-to-back topology of Bhabha scattering with a high purity, which is fundamental for ensuring a high trigger efficiency of low multiplicity processes.

The L1 trigger can sustain a maximum instantaneous rate of 30 kHz, however the goal is to keep the trigger rate as low as possible, while ensuring a high efficiency (larger than 99 %) for physics targets, mainly hadronic events. The L1 output is then forwarded to the High Level Trigger for further background rejection based on fully reconstructed objects.

The High Level Trigger

The decision whether to finally keep the event after the software trigger is based on variables calculated on the event topology and the physical properties of the particles. This implies, that the particles are fully reconstructed using the detector data, which is a highly demanding task. This task cannot only be implemented on low-level hardware but needs software running on a server farm. The HLT is a software trigger developed to improve the backgrounds suppression and main purpose to reduce the load of data written on permanent storage at a maximum design output event rate of 10 kHz. Events preselected by using only the information provided by CDC and ECL triggers undergo the full offline reconstruction, involving all output from the subdetectors except the PXD. The physics trigger is then able to classify the event category ($B\bar{B}, e^+e^- \rightarrow \tau^+\tau^-$, etc.) and once this has been assigned, the HLT processing results containing the event tag and the track parameter estimate are combined with the information from the PXD, which enables to calculate the Region of Interest (ROI), A rectangular-shaped region around the extrapolated positions on each sensor plane, where a particle is expected to travel through the detector. Only the pixels belonging to that region are readout and the selected PXD hits are used to complete the event reconstruction.

During the recording of the collisions, the data needs to be monitored to assure a constant data quality without degradation in neither the detector systems, the triggers nor the online reconstruction. A defined fraction of triggered events together with the PXD information is not only sent to the storage system, but also to the ExpressReco farm, which executes the default offline reconstruction and extracts a set of monitoring plots, which are shown integrated over multiple events to the control room shifters. Software for automatic deviation detection helps to identify possible failures of hardware and software.

Storage and Offline Reconstruction

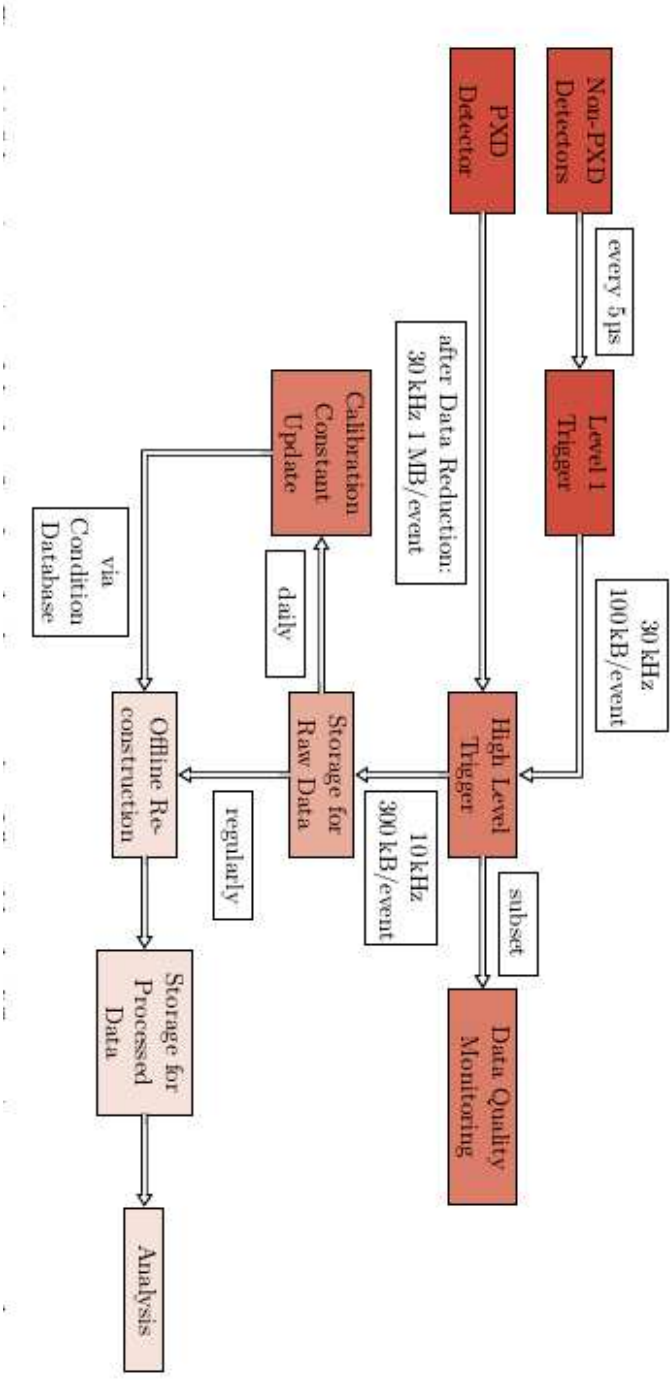


Figure 3.16: Schematic overview of the data flow from the detector readout followed by the different trigger stages up to storage devices. The stored data is then processed and used for physics analysis. The shown data rates are preliminary and are taken from the current software simulation using the physics rates in [].

The combined subdetector data of the events, that survive the different trigger stages is stored to disk afterwards. Asynchronously to the data taking, the recorded data is reprocessed using a slower but more precise offline reconstruction running on a large computing cluster. During this reconstruction, information on the detector conditions (alignment and calibration constants) during the data acquisition is taken into account. Those constants are calculated on the data itself by using well-known physics processes with a distinct topology that allows to measure e.g. the displacement of the different detector layers among each other. The process of calibration and alignment is repeated regularly on the recorded data and the result is fed into a database, which is both used for the reprocessing of the data as well as for future online software runs. The output of the offline reconstruction is a summary of the reconstructed particles suitable for physics analyses known as mDST. Skimming campaigns sort the data according to their HLT tags and other variables calculated on the reconstructed particles to make physics analyses faster. The reconstructed as well as the raw data is distributed to different computing centers around the world for better accessibility and data backup.

CHAPTER 4

TDCPV Analysis of $B^0 \to K^0_S \pi^+ \pi^- \gamma$ and $B^0 \to K^0_S \pi^0 \gamma$

In this chapter, we introduce the Time dependent CP violation of $B^0 \to K^0_S \pi^+ \pi^- \gamma$ and $B^0 \to K^0_S \pi^0 \gamma$ analysis done using Belle II simulated data. The chapter starts by covering the concepts, details, analysis techniques used in the analysis. Then, I present the analysis steps followed to investigate the sensitivity of Belle II to non-zero values of $\mathcal{S}$ the two TDCPV channels.

4.1 Principle of measurement

In the following section, the main principles used by Belle II are described, this principles have enabled to perform time dependent CP violation measurements.

At Belle II, the electron-positron collisions provide a clean environment for studying B^0 physics. The center of mass energy of colliding electron and positron beams is at the $\Upsilon(4S)$ resonance of 10.58 GeV which decays to a B^0 $\bar{B}^0$ pair and this pair is practically at rest in the $\Upsilon(4S)$ center of mass system (CMS).

The $B^0\bar{B}^0$ meson pair is produced in a quantum coherent state (quantum entangled). When propagating, each B meson undergoes flavor mixing. But the

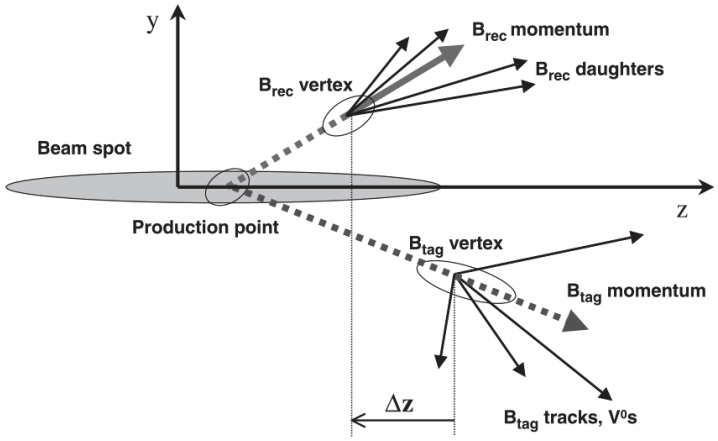


Figure 4.1: B_{rec} denotes the reconstructed decaying into states of interest. Evaluation of the CP violating asymmetries requires knowing the flavour of the B^0 meson at its decay time. This is achieved by identifying the decay channel of the other B^0 meson, B^0_{tag}, inclusively reconstructed, the knowledge of the difference between the decay times of both B mesons allows us to infer the flavour of B^0_{sig}. The time elapsed between the two decays can be calculated from the distance Δz measured between the two B decay vertices along the beam direction z.

pair coherence insures that if one meson changes flavor, the other automatically changes flavor too. Hence, the opposite flavor is preserved within the pair until one meson decays. This fact allows the so-called flavor tagging technique. In this analysis, we note one of the meson B^0_{tag}, to decay at time t_{tag} into a flavor specific final state, experimentally identified through inclusive reconstruction. By quantum entanglement we know that the other B meson of the pair, noted in this analysis B^0_{sig}, was in the opposite flavor eigenstate at the same time t_{tag}. Then as B^0_{sig} evolves in time, it decays into the states of interest $B^0 \to K^0_S \pi^+ \pi^- \gamma$ and $B^0 \to K^0_S \pi^0 \gamma$ at t_{tag} + Δt, B^0_{sig} could decay before B^0_{tag} decays, resulting in negative Δt. In order to infer Δt, the distance between the decay vertices of B^0_{tag} and B^0_{sig} is measured benefiting from the asymmetric colliding beam energies.

At SuperKEKB collider, the electron beam energy is 7 GeV, while the positron beam energy is 4 GeV. The resulting $\Upsilon(4S)$ resonance is boosted along the beam direction[1] with a boost factor $\beta\gamma = 0.28$. The already mentioned fact that a B^0 meson pair is practically at rest in the $\Upsilon(4S)$ center of mass frame, allows to derive the following conversion between the time difference Δt and the distance between the two B^0 decay vertices Δz:

$$\Delta t \simeq \frac{\Delta z}{\gamma \beta c}, \tag{4.1}$$

Taking into account the known value of the B meson lifetime $\tau_{B^0} \sim 1.5$ ps, Δz is about 136 μm. The z vertex position is related to the proper time t by:

[1] In fact, the two beam collides with a very small angle of 83 mrad or 4.76 degrees, which is neglected in this analysis and the beam is assumed to follow the z-axis.

$$z = \gamma(\alpha\cos\theta + \beta\sqrt{1+\alpha^2})ct \tag{4.2}$$

where γ and β are the boost parameters from the $\Upsilon(4S)$ frame to the lab frame and θ and $\alpha = p^*_B c/m_B c^2$ are the polar angle and boost factor of the B in the $\Upsilon(4S)$ frame. Since no tracks originate from the production vertex, the sensitivity to the decay time difference of the B^0 mesons comes mainly through the difference in the z positions of the decay vertices. As the polar angles of the two B mesons are exactly opposite, the difference in the z positions can be expressed as

$$\Delta z = \gamma\beta\sqrt{(1+\alpha^2)}c(t_1 - t_2) + \gamma\alpha\cos\theta_c(t_1 + t_2). \tag{4.3}$$

since the parameter $\alpha \sim 0.06$, it is ignored, and one obtains the well known approximation in eq 4.1. Consequently, the experimental resolution on the B meson decay time-difference is dominated by the resolution on the decay vertex position. To measure the time dependent CP violation Δz has to be determined with the resolution of about 136 μm, or better. Belle II targets 60 μm for this resolution, thanks to the pixel layers of the VXD 3.7.

The described principle of measurement is summarized in Figure 4.1. It can be summarized by four main steps:

1. Determine (by tagging) the flavour of one of the B mesons (B^0_{tag}).
2. Reconstruct the associated B^0_{sig} decaying into either $B^0 \to K^0_S\pi^+\pi^-\gamma$ or $B^0 \to K^0_S\pi^0\gamma$.
3. Measure the distance between the decay vertices of B^0_{tag} and B^0_{sig}.
4. Extract the TDCPV parameters from the obtained decay time distribution.

The principle presented in the previous section is promising, but the real world is not ideal. Each step requires method and tool that is discussed in the following text.

4.1.1 Flavor tagging

As discussed before, flavour tagging is required for the measurements of CP violation, where the decay of B^0_{sig} is fully reconstructed and the flavour of the other B^0 meson, B^0_{tag} has to be determined. The task of the flavour tagger is to determine the flavour of B^0_{tag} at the time of its decay. The algorithm used is common to most of Belle II measurements and is described in detail in [33]. Since B^0 mesons exhibit a large number of possible decay channels, many of them provide unambiguous flavour signatures through flavour-specific final states. Flavour signatures correspond to signed characteristics of the decay products that are correlated with the charge sign of the b-quark in the B meson. Because of the wide range of possible decay channels it is not feasible to fully reconstruct

a large fraction of flavour-specific B^0_{tag} decays. Instead of a full reconstruction, the flavour tagger applies inclusive techniques based on multivariate methods to maximally exploit the information provided by the different flavour-specific signatures. The Belle II flavour tagger was developed by using several useful concepts of previous algorithms used by the Belle and the BaBar collaborations [36].

Tagging categories

Flavour tagger is based on flavour-specific decay modes with relatively high branching fractions > 2 %). Each decay mode exhibits a particular decay topology and provides a flavour-specific signature. Some additional signatures are obtained by combining similar or complementary decay modes. Within a so-called category, a particular flavour signature is considered separately. The current flavour tagger is based on 13 categories which are presented in Table 4.1.

Categories	Targets for B^0
Electron	e^-
Intermediate Electron	e^+
Muon	μ^-
Intermediate Muon	μ^+
Kinetic lepton	l^-
Intermediate Kinetic lepton	l^+
Kaon	K^-
Kaon-Pion	K^-, π^+
Maximum P^*(CMS)	l^-, π^+
Fast-Slow-Correlated (FSC)	l^-, π^+
Fast Hadron	π^+, K^-
Lambda	Λ

Underlying decay modes

$\overline{B}^0 \to D^{*+}\ \overline{\nu}_\ell\ \ell^-$
$\quad\hookrightarrow D^0\ \pi^+$
$\quad\quad\hookrightarrow X\ K^-$

$\overline{B}^0 \to D^+\ \pi^-\ (K^-)$
$\quad\hookrightarrow K^0\ \nu_\ell\ \ell^+$

$\overline{B}^0 \to \Lambda_c^+\ X^-$
$\quad\hookrightarrow \Lambda\ \pi^+$
$\quad\quad\hookrightarrow p\ \pi^-$

Table 4.1: Tagging categories and their targets(left) with some characteristic examples of the considered decay modes (right). $l^\pm$ stands for charged leptons (μ or e).

The flavour-specific final state particles in the considered decay modes are treated as targets since their charges are correlated with the flavour of B^0_{tag}. In order to extract these flavour-specific signatures, the targets have to be identified among all available particle candidates. To accomplish this task, discriminating variables are calculated for each particle candidate. An overview of the discriminating variables for each category is presented in details in [33]. The Flavor tagger algorithm combines the results of all categories and tracks considered, and returns two parameters, flavour tag q, and flavour dilution factor r. The output y with a range between 0 and 1, is equivalent to $y = q.r$, where $y = -1(1)$ if B^0_{tag} is perfectly tagged as $\overline{B}^0$ (B^0) respectively.

A schematic overview of the information flow in the algorithm is presented in Figure 4.2. The algorithm has an event-and combiner-levels. The event-level process is performed within each individual category. On this level, a multivariate method based on Fast boosted decision tree (FBDT) [37] assigns to each

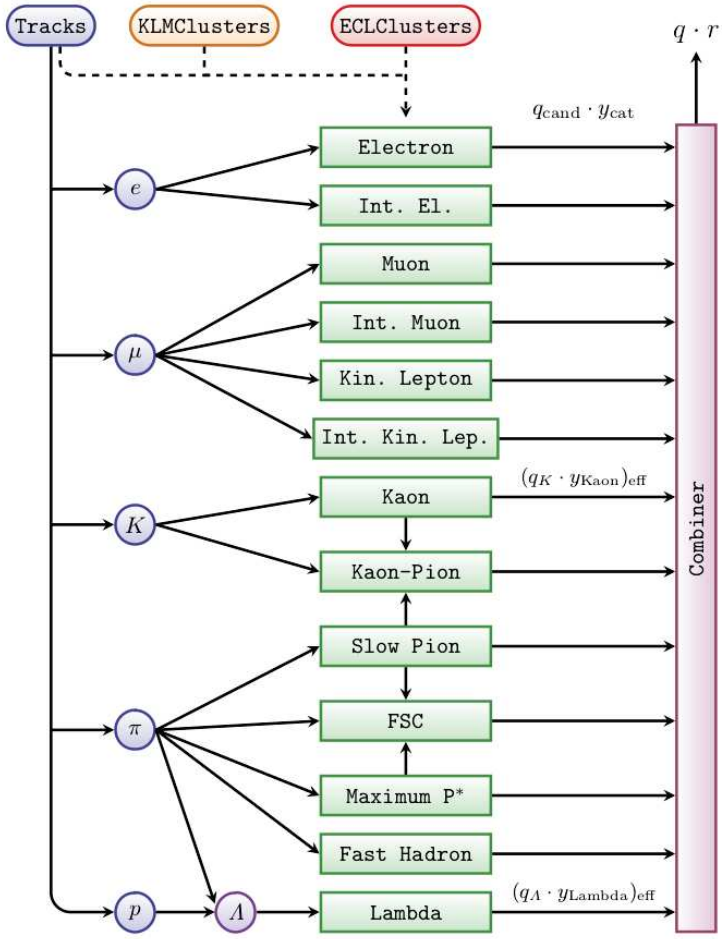


Figure 4.2: Schematic overview of the Flavour Tagger: Reconstructed tracks are available for five different mass hypotheses. Each green box corresponds to a category. The event-level process is performed within each individual category. Then to each particle candidate a probability y_{cand} is assigned, then combined to provide the final $q.r$ output.

particle candidate a probability y_{cat}, which is the probability of being the target of the corresponding category providing the correct flavour tag.

Beside q and r the fraction of wrongly tagged candidates (w), called mistag probability and the difference in fraction of wrongly tagged B^0 and $\bar{B}^0$ candidates (Δw), is also needed for the TDCPV analysis. The categories are characterized by their average efficiencies ϵ as well as the effective tagging efficiency defined as $Q = \epsilon(1-2w)^2$.

Performance

The performance of the Belle II flavour tagger has been evaluated using Belle II simulated data, and real data. Also an comparison between both Belle II simulated and real data with Belle provides interesting insight to assess Belle II's performance. The output $y = q.r$, which corresponds to the product of tagged flavour q and the dilution factor r, can be found in Figure 4.3 (left) for the FBDT

combiner on MC. Figure 4.3 (right) also shows a linearity check between the true dilution r_{MC} determined using MC information and the mean $\langle r \rangle$ of the dilution provided by the combiners. The mean dilution $\langle r \rangle$ of the combiner output is simply the mean of $|q.r|$ for each r-bin. Thus Figure 4.3(right) shows the results of the linearity check for events where B^0_{tag} is a B^0, for events where B^0_{tag} is a B^0, and in average. The FBDT combiner achieves a total effective efficiency ϵ_{eff} of $(36.67 \pm 0.5)\%$ on Belle II MC and $34.26 \pm 0.03\%$ on Belle MC. Where

$$\epsilon_{eff} = \sum_i \epsilon_i.(1 - 2w_i)^2 \tag{4.4}$$

ϵ_i is the partial efficiencies(in each r-bin) and w_i is the wrong-tag fractions.

In comparison with previous Belle flavour tagger, which reached an effective efficiency of $(30 \pm 0.4)\%$ on Belle data [36], the Belle II flavour tagger reaches an effective efficiency of $(33 \pm 0.5)\%$ on Belle data. An additional increase of about 3% in effective efficiency is observed due to the improved track reconstruction and the improved PID performance at Belle II. In Figure 4.4, I show one of the newest studies, the comparison of efficiencies obtained with the Belle II flavor tagger for 2019 Belle II data and with the Belle flavor tagger in Belle data. The performance of the Belle II flavor tagger is comparable with the best one obtained by the Belle experiment, thanks to the new Belle II category-based flavor tagger considering more flavor signatures and more input variables.

4.1.2 Extraction of CP violation parameter

To extract the values of the CP parameters, $\mathcal{A}$ and $\mathcal{S}$, neglecting the experimental effects, the following probability density function (PDF), obtained from the decay rates in equation 2.45 is used to fit the time distribution,

$$\mathcal{P}(\Delta t, q) = \frac{e^{-|\Delta t|/\tau_{B^0}}}{4\tau_{B^0}}[1 + q\mathcal{A}\cos(\Delta M \Delta t) + \mathcal{S}\sin(\Delta M \Delta t)] \tag{4.5}$$

where $q = +1$ when $B^0_{tag} = B^0$ and $q = -1$ when $B^0_{tag} = \overline{B^0}$. Indeed, in order to obtain correct $\mathcal{S}$ and $\mathcal{A}$, we need to include the experimental effects, Equation 4.5 may be re-written in term of the tagging information as:

$$\begin{aligned}\mathcal{P}(\Delta t, q) = f_{sig}\frac{e^{-|\Delta t|/\tau_{B^0}}}{4\tau_{B^0}}[1 - q\Delta w + (1 - 2w)q\mathcal{A}\cos(\Delta M \Delta t) + \\ \mathcal{S}\sin(\Delta M \Delta t)] \otimes \mathcal{R}_{sig}(\Delta t) - (1 - f_{sig})\mathcal{P}_{bkg}(\Delta t)\end{aligned} \tag{4.6}$$

where $\mathcal{P}_{bkg}(\Delta t)$ is the PDF describing Δt distribution of background candidates, and $\mathcal{R}_{sig}(\Delta t)$ Δt resolution function for signal candidates. In order to obtain unbiased values of CP parameters, it is important to have good understanding and estimations of f_{sig}, w, Δw, $\mathcal{R}_{sig}$, and $\mathcal{P}_{bkg}$. Then we construct a likelihood function and maximize it to get the best estimates for $\mathcal{A}$ and $\mathcal{S}$.

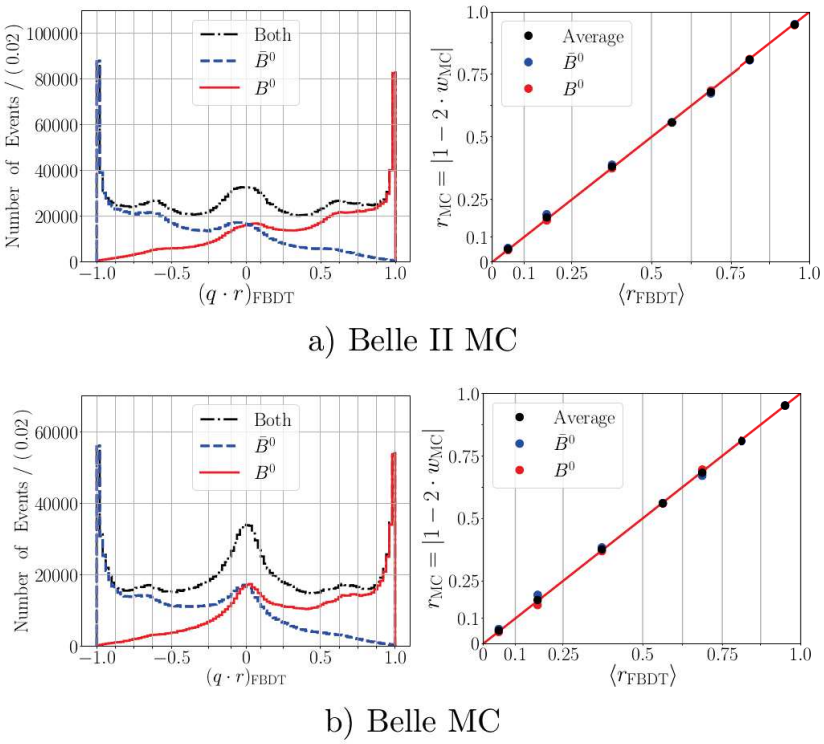


Figure 4.3: Results of the Flavor tagger FBDT combiner using a) Belle II MC and b) Belle MC. Left: Distribution of the $q.r$ output. Right: Truth matched dilution $r_{MC} = 1 - 2w_{MC}$ taken from MC truth in each r-bin. The errors on both axes are not visible due to their small size. The red diagonal line is a guideline and the vertical grey lines correspond to the limits of the r-bins.

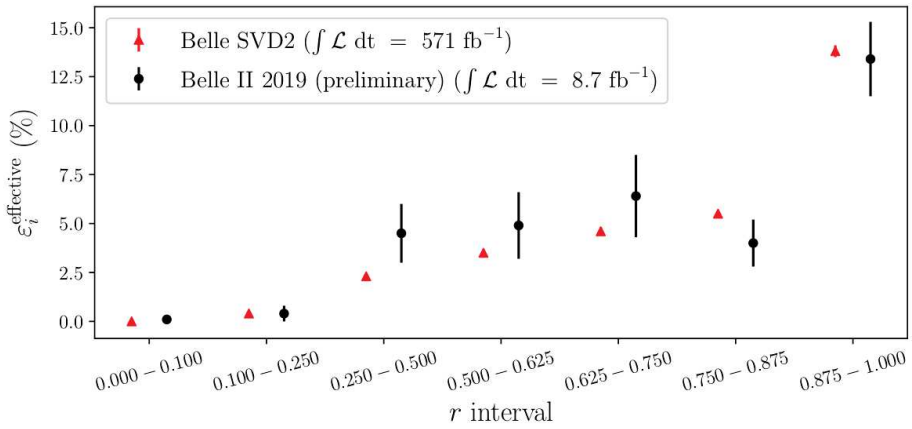


Figure 4.4: Performance of the Belle II flavor tagger in 2019 Belle II data and of the Belle flavor tagger in Belle data [36] taken with the second silicon-vertex detector configuration(SVD2)

4.2 Preparation of measurement procedure

In this section, the analysis procedure is described in detail.

4.2.1 Data samples

Signal MC: dataset of simulated signal events, where $\Upsilon(4S) \to B^0\overline{B}^0$ process, with one B^0 meson decaying to $B^0 \to K^0_S\pi^+\pi^-\gamma$ or $B^0 \to K^0_S\pi^0\gamma$.

Generic BB MC: dataset of simulated events containing $\Upsilon(4S) \to B^+B^-$ or $B^0\overline{B}^0$ process, with both B mesons decaying generically excluding the signal decay. These events are treated as background in this analysis.

Continuum MC: dataset of simulated continuum events $e^+e^- \to q\overline{q}$ $(q = u, d, s, c)$. No B mesons are produced in these events and they are also background for this analysis.

Full MC: dataset of simulated events obtained by merging signal MC, generic $B^0\overline{B}^0$ MC and continuum MC with fraction as expected in data according to specific luminosity.

4.2.2 $B^0 \to K^0_S\pi^+\pi^-\gamma$ and $B^0 \to K^0_S\pi^0\gamma$ decays

The branching fraction of the decays $B^0 \to K^0_S\pi^+\pi^-\gamma$ and $B^0 \to K^0_S\pi^0\gamma$ taken from [38] [39] are

$$\mathcal{B}(B^0 \to K^0_S\pi^+\pi^-\gamma) = 6.47 \times 10^{-6}, \quad \mathcal{B}(B^0 \to K^0_S\pi^0\gamma) = 9 \times 10^{-6}. \tag{4.7}$$

$B^0 \to K^0_S\pi^+\pi^-\gamma$ decays through several kaonic resonances called X_d which contain also non-CP eigenstates, while $B^0 \to K^0_S\pi^0\gamma$ goes through several kaonic resonances and K^{*0} that contain only CP eigenstates which make it more sensitive to TDCPV measurement.

4.3 Reconstruction and selection cuts

In this section we describe the reconstruction of the two decay channels and the criteria used to reduce the number of B^0 candidates coming from the background events.

For candidate selection, a skim is first applied, as will be described in 4.3.1. After skimming, several cuts are used 4.3.2. At first order, the candidate selection for the present analysis relies on the selection criteria from the previous BABAR and Belle analysis, then this criteria is optimized. For $B^0 \to K^0_S\pi^+\pi^-\gamma$, we reconstruct $X_{sd} \to K^0_S\ \pi^+\ \pi^-$, where $K^0_S \to \pi^+\ \pi^+$. As well as for $B^0 \to K^0_S\pi^0\gamma$, we reconstruct $K^0_S \to \pi^+\ \pi^-$ and $\pi^0 \to \gamma\ \gamma$. Therefore, each of the two decay

modes is reconstructed by combining the event charged pion tracks and photon candidates, as these are the only final state particle species in our decay. Blindly combining particles would be useless, since there is an abundance of events containing charged tracks and photon hits. Thus we impose the selection criteria that will be satisfied by a large fraction of signal candidates, and at the same time reject a significant amount of background candidates. Having a large amount of background candidates, even if correctly described in the PDF used for the fit, results in a lower sensitivity to the fitted parameters (larger statistical uncertainty). On the other hand, since there is no distribution in which the signal and background candidates are completely separated, by imposing the selection criteria we are also loosing some fraction of signal candidates. Because the goal of this analysis is to obtain the values of TDCPV parameters with the smallest possible uncertainty, we optimize the selection criteria to achieve this goal.

4.3.1 Skim

In order to reduce the size of the data sample and hence gain in processing time, a skim is applied before any other selection criteria. It consist of loose requirements, which can be used by various analysis. In the present analysis, we use the $TDCPV_{skim}$ available in the Belle II collaboration. This skim selects events passing the filter that requires at least three tracks. The skim also requires high-energy photon, consistent with a radiative B decay, and that the CM energy of the highest-energy photon candidate in the event falls between 1.5 and 3.5 GeV.

4.3.2 Selection cuts

High-energy photon selection

The high-energy photons, which are taken from the the loose standard photon lists and further required to pass the following selection criteria:

- $0.3 < \theta_\gamma < 2.6$, where θ_γ is the polar angle in radians.
- Photon Energy $1.7 < E < 4$ GeV.

$\pi^\pm$ and π^0 selection

The $\pi^\pm$ are selected from the standard pion list in Belle2 software, with no additional cuts, For π^0, the two photon are required to have an energy > 0.08, and an invariant mass 0.124 < M < 0.140.

Reconstruction of K^0_S

To reconstruct the K^0_S two charged pion tracks are combined, they are chosen from the K^0_S default list with a PID cut larger then 0.005. The geometric fit performed by "TreeFitter" that determines the K^0_S decay vertex, allows to evaluate

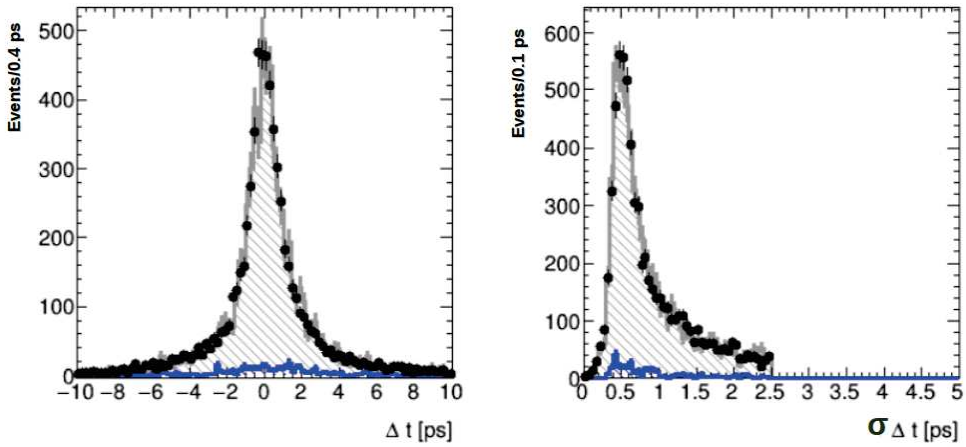


Figure 4.5: Distributions of Δt (left) for $B^0 \to K^0_S\pi^+\pi^-\gamma$, and $\sigma_{\Delta t}$ (right) for signal MC events (blue), data challenge (black dots), full simulated data sample (Gray).

the K^0_S candidate four momentum and trajectory. Its mass is also computed using π^+ π^- track momenta evaluated at the vertex. In order to determine the trajectory, the K^0_S production vertex (i.e. the B decay vertex) is also required. The displaced decay of the K^0_S is useful for rejecting background, especially $q\bar{q}$ events. Thus, we compute the decay length significance, $d_{K^0_S}/\sigma(d_{K^0_S})$, defined as the ratio of the three dimensional length of the K^0_S trajectory divided by the error on that quantity obtained from the vertex fit. We also compute θ_{flight} corresponding to the angle between the K^0_S trajectory and its momentum vector. The following cuts are applied on K^0_S candidates:

- $|m_{\pi^+\pi^-} - m_{K^0_S}| < 11\,\text{MeV}/c$
- $\cos\theta_{flight} > 0.995$
- $d_{K^0_S}/\sigma(d_{K^0_S}) > 9$

These cuts are chosen first from Belle and Babar analysis but their values have been optimized for the present analysis as discussed more in section 4.3.5

Δt and $\sigma_{\Delta t}$

Very loose cuts are applied to the variables Δt and $\sigma_{\Delta t}$. These cuts were first taken from previous $B^0 \to K^0_S\pi^+\pi^-\gamma$ analysis and then demonstrated using Belle II simulated data. The two distributions are shown in Figure 4.5 and the cuts follows :

- $|\Delta t| \leq 20$ ps
- $\sigma_{\Delta t} \leq 2.5$ ps

$m_{\pi\pi}$ and $m_{K\pi\pi}$

In order to increase the proportion of $B^0 \to K^0_S\pi^+\pi^-\gamma$ we apply cuts on the $m_{\pi\pi}$ as well, we restrict the $K^0_S\pi\pi$ resonance mass to be below 1.8 GeV/c^2, since it is not expected to contain a large number of signal events, while significant number of background events.

- $0.6\,\text{GeV}/c^2 \leq m_{\pi\pi} \leq 0.9\,\text{GeV}/c^2$,
- $m_{K\pi\pi} < 2\,\text{GeV}/c^2$

Vetos of π^0 and η

As in our signal mode we have a high energy photon, most of our photon background originates from misreconstructed π^0 and η. Indeed, these fake isolated photons either come from asymmetric decays of π^0 and η (one of the photons takes most of the energy of the decaying particle) or from merged photons (the decaying particle has a high momentum in the CM frame therefore the two outgoing photons cannot be properly separated in the EMC). To reduce these backgrounds, the photon candidate γ_1 is associated with all other photons γ_2. Then we construct the π^0 and η likelihood functions, defined as

$$\mathcal{LR} = \frac{p(m_{\gamma_1\gamma_2}, E_{\gamma_2}|\theta)}{p(m_{\gamma_1\gamma_2}, E_{\gamma_2}|K^0_S\pi^+\pi^-\gamma) + p(m_{\gamma_1\gamma_2}, E_{\gamma_2}|\theta)} \tag{4.8}$$

where θ is either the π^0 or η hypothesis, and p is a probability density function in terms of $m_{\gamma_1\gamma_2}$ and the energy of γ_2 in the lab frame, E_{γ_2}. The $\mathcal{LR}$ of π^0 and η is between zero and one, and the larger the value is, the more likely it is that γ_1 comes from the π^0 or η decay. We select then respectively:

- For $B^0 \to K^0_S\pi^+\pi^-\gamma$: $\mathcal{LR}_{\pi^0} < 0.82$ and $\mathcal{LR}_{\eta} < 0.954$.
- For $B^0 \to K^0_S\pi^0\gamma$: $\mathcal{LR}_{\pi^0} < 0.84$ and $\mathcal{LR}_{\eta} < 0.91$.

These cuts where optimized using the procedure described in Section 4.3.5.

4.3.3 Reconstruction of B^0 meson

Taking advantage of the well know initial state, e^+e^-, at B Factories, combined with the fact the $b\bar{b}$ pair is produced via the decay of the $\Upsilon(4S)$ resonance, two kinematical variables can be constructed in order to discriminate signal from continuum and generic $B^0\overline{B}^0$ events. Namely, these two variables are the energy difference ΔE and the energy-substituted mass M_{bc}. As well a variable based on the event shape to separate signal from background.

The energy difference ΔE

The energy difference, ΔE, can be expressed in a Lorentz invariant form as

$$\Delta E = (2q_B q_0 - s)/2\sqrt{s}, \tag{4.9}$$

where $q_0 = q + q = (E_0, p_0)$ are the Lorentz vectors representing the of the initial e^+e^- system,and q_B represents the momentum of the B-meson system and $\sqrt{s} = 2E^*_{beam}$ denotes the CM energy. In the CM frame, ΔE can be expressed as

$$\Delta E = E^*_B - \sqrt{s}/2, \tag{4.10}$$

where E^*_B reconstructed energy of the B candidate without applying any constraint. Since ΔE is by construction related to the mass hypotheses for each of the tracks, its distribution will strongly depend on the nature of the final state particles. For instance, in the case where a kaon is misidentified as a pion, its reconstructed energy, and consequently that of the B candidate, will be smaller than expected, and the event will be shifted towards negative values of ΔE. On the other hand, the distribution for correctly reconstructed signal events will peak at zero. This makes ΔE especially helpful in isolating backgrounds from misreconstructed B decays. Moreover, since continuum events do not originate from B decays, their distribution in this variable is expected to be linear in the whole dynamical range, excluding acceptance effects and phase space.

The energy-substituted mass M_{bc}

The momenta of the

$$M_{\mathrm{bc}} = \sqrt{E^*_{beam} - p^{*2}_B} \tag{4.11}$$

where p^{*2}_B is the CM momentum of the B candidate. Since the candidate is formed from a number of tracks and neutral objects whose energies are not as accurately measured as are the beam conditions, the B-candidate energy is here substituted by E^*_{beam}. This allows to improve the mass resolution by using our knowledge of the initial kinematics. Due to the annihilation of the electron and the positron, which creates a $B\bar{B}$ pair, and to the fact that the masses of the particle and of the antiparticle are equal, for signal events, M_{bc} yields the mass of the B^0 meson and shows a clean peak. Thus we select respectively candidates with:

- For $B^0 \to K^0_S\pi^+\pi^-\gamma$, $M_{bc} > 5.2\,\mathrm{GeV}/c^2$ and $|\Delta E| < 0.2\,\mathrm{GeV}$
- For $B^0 \to K^0_S\pi^0\gamma$, $M_{bc} > 5.2\,\mathrm{GeV}/c^2$ and $-0.25 < \Delta E < 0.2\,\mathrm{GeV}$

Figure 4.6 illustrates the discriminating power of these two variables.

4.3.4 Event-shape variables

As already stated in 4.3.3, a strong variable based on the event shape is used to separate signal event from continuum events, since due to the kinematics of the decay products in $e^+e^- \to \Upsilon(4S) \to B\bar{B}$ and $e^+e^- \to q\bar{q}$, $q = u, d, s, c$ processes, strong differences arise in the angular correlations among the $B\bar{B}$ decay daughters and continuum events. $B\bar{B}$ events follow the spin-1 $\Upsilon(4S)$ resonance decay

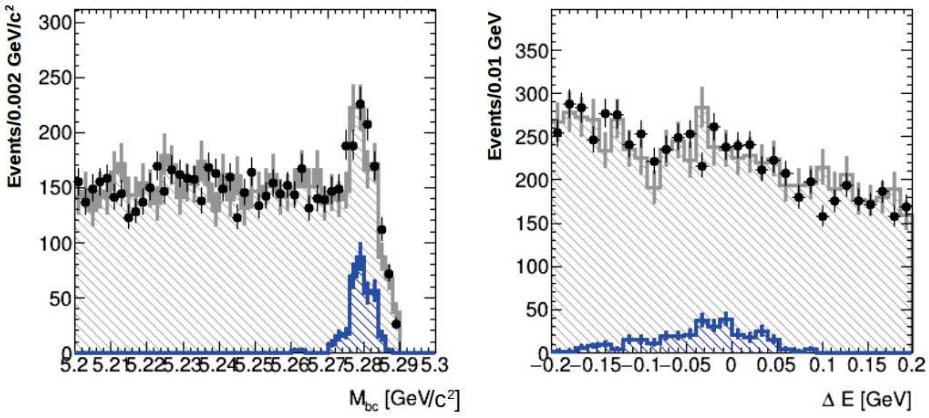


Figure 4.6: Distributions of the two kinematical variables for $B^0 \to K^0_S\pi^+\pi^-\gamma$, M_{bc} (left) and ΔE (right) for signal MC events (blue), full simulated data (black), full MC sample (Gray).

into two spin-0 B mesons, resulting in a $\sin^2\theta$ distribution, where θ is the angle between the B direction and the z-axis. While in continuum events, a small amount of the initial energy is invested in the rest masses of the quarks. As a result most of the available center-of-mass energy will be carried as kinetic energy, which implies that the event will have a two-jet-like structure and will roughly follow a $(1+\cos^2\theta)$ dependence, where θ is the center-of-mass angle of a jet with respect to the beam axis. Taking advantage of these differences, several variables discussed below are useful to separate between these two event species.

Thrust Axis

The thrust of an ensemble of particles is defined as the direction, $\hat{t}$, in which the sum, $\hat{T}$, of the projections of the momenta of the particles is maximized:

$$\hat{T} = max\left(\frac{\sum_i |\hat{t}_i.p_i^*|}{\sum_i |p_i^*|}\right) \tag{4.12}$$

where the index i runs over all the particles in the ensemble. For $B\bar{B}$ events, $\hat{T}$ takes almost random values, as the events are mostly isotropic as shown in Figure 4.7. For $q\bar{q}$ events, on the other hand, $\hat{T}$ follows the direction of the formed jets, and is therefore strongly directional.

Thrust angles

Employing the thrust axis, several other variables can be employed, such as the cosine of the angle between the thrust axis of the momenta of the B candidate and the z axis, $\cos\theta_{\hat{T}}$, or the cosine of the angle between the thrust axis of the B candidate and the rest of the event, $\cos\theta^{ROE}_{\hat{T}}$. For a $B\bar{B}$ event, decay particles are isotropically distributed and their thrust axis are randomly distributed. Therefore, $\cos\theta^{ROE}_{\hat{T}}$ follows a uniform distribution in the range [0, 1], while for $\cos\theta_{\hat{T}}$, it is uniformly distributed. In contrast, for $q\bar{q}$ events, the thrusts of both the B

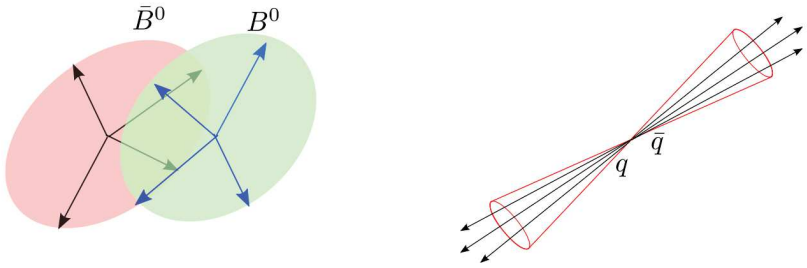


Figure 4.7: Decay products of B mesons are distributed isotropically, forming the event with spherical geometry. Particles from continuum events form the jet-like geometry of an event

candidate and the ROE are strongly directional, yielding a $\cos\theta^{ROE}_{\hat{T}}$ distribution strongly peaked at large values.

CLEO Cones

The CLEO collaboration introduced variables based on the sum of the absolute values of the momenta of all particles within angular sectors around the thrust axis, resulting in 9 concentric cones []. The cone in the direction of the thrust axis is merged with the respective cone in the opposite direction. There are two options for constructing the CLEO cones in Belle II, they can be calculated from all final state particles in the event, or from only ROE particles.

Fox-Wolfram moments

For a collection of N particles, the Fox-Wolfram moment H_L is defined as

$$H_L = \sum_{i,j}^{N} |p_i||p_j| P_L(\cos\theta_{i,j}), \tag{4.13}$$

where p_i and p_j are the momenta of the i^{th} and the j^{th} particle in the event, P_L is the l^{th} order Legendre polynomial and θ_{ij} is the angle between the momenta of particles i and j. The ratio between the 2-nd and 0-th $\mathbf{R_2} = \mathbf{H_2}/\mathbf{H_0}$, order moments of the rest-of-event is used to describe the event topology in e^+e^- collisions and presents a strongly discriminating variable. In the case of a $q\bar{q}$ event, $\mathbf{R_2}$ are expected to be closer to 1, which indicates a jet-like event. In contrast, for $B\bar{B}$ events, values of $\mathbf{R_2}$ are expected to be closer to 0, indication of a nearly isotropic event.

Modified Fox-Wolfram moments

The Belle II collaboration has also developed the modified Super-Fox-Wolfram moments H^{so}_{xl} and H^{oo}_{l} ($l \in [0,4]$), where all reconstructed particles in an event are divided into two categories: B candidate daughters (denoted as s) and particles from ROE (denoted as o). The H^{so}_{xl} moments are decomposed into an additional three categories (denoted as x) depending on whether the particle is

charged ($x = c$), neutral ($x = n$), or $missing (x = m)$. Additionally, for H^{so}_{xl}, the missing momentum of an event is treated as an additional particle.

$$H^{so}_{xl} = \sum_i \sum_{jx} |p_{jx}| P_l(\cos\theta_{i,jx}), \tag{4.14}$$

where i runs over the B daughters; jx runs over the ROE in the category x; p_{jx} is the momentum of the particle jx; and $P_l(\cos\theta_{i,jx})$ is the l^{th} order Legendre polynomial of the cosine of the angle between particles i and jx.

Fisher discriminant

Since the event-shape variables described above exploit different aspects of the same physical principle, some correlations might appear among them. Thus Fisher discriminant (put ref) is constructed taking into account the correlations between them, defined as a linear combination of several discriminating variables x_i, taking the advantage of all of them to maximize the separation power.

$$\mathcal{F} = \sum_i a_i x_i = \mathbf{a}^T\mathbf{x}, \tag{4.15}$$

where a^T is a line vector. The parameter a_i are optimized with the use of the signal and continuum simulated data to give the best separation between candidates from true B^0 decays and from the continuum events.

In the current analysis a multivariate analysis (TMVA) is trained using as inputs the thrust, Cleo Cones, and Fox-Wolfram moments variables and produces as a output the Fisher discriminant variable called "CSMVA" that varies from 0 to 1 depending on whether the event is continuum-like or $B\overline{B}$-like.

Vertex selection

The B^0 candidates are formed by fitting the vertex of all the final state particles, using tracks or cluster information in case of charged particles or the photon respectively. The fit on the decay products of the reconstructed $B^0 \to K^0_S\pi^0\gamma$ is performed with a "iptube", constrained to be on the IP, tube along the tag B line of flight. while no constraint is done for the $B^0 \to K^0_S\pi^+\pi^-\gamma$. Although the high-energy photon is included in the fit in order to get higher constraints on the B candidate kinematics, it will not contribute to the vertex information.

In order to reduce combinatorial backgrounds, a cut on the vertex probability, which results from the vertex fit, is applied. From the optimization procedure, described below, we select candidates with a vertex probability greater than 0.0001.

4.3.5 Cuts Optimization

$B^0 \to K^0_S\pi^+\pi^-\gamma$ cuts optimization

Table 4.6 shows all the selection cuts used in the analysis. In order to maxim ize the sensitivity on the CP asymmetry parameters $\mathcal{S}$ and $\mathcal{C}$, cut optimization is done by maximizing the Significance, called Figure of merit. This significance defined as $\frac{S}{\sqrt{S+B}}$, where S is the signal yield, signed as truth matched in the simulated data and B denotes the background, the total yield signified as non-truth matched in belle II software. The optimization procedure was done inside the signal region (i.e. in $M_{bc} > 5.26\,\text{GeV}/c^2and-0.2 < \Delta E < 0.1$), using a set of eight variables,

- $m_{K\pi\pi}$, $\mathcal{LR}_{\pi^0}$, $\mathcal{LR}_{\eta}$, B vertex probability
- $\cos\theta_\gamma$, K^0_S decay length significance
- π_1 PID, π_2 PID

Steps

- First for each variable, the significance $\frac{S}{\sqrt{S+B}}$is measured as function of the variable cut values, as shown in Figure 5.31.
- The variable reaching the highest significance, $d_{K^0_S}/\sigma(d_{K^0_S}) > 20$ is chosen with a $\frac{S}{\sqrt{S+B}} = 7.2$
- All cuts are applied and again the $\frac{S}{\sqrt{S+B}}$of the variable chosen, $d_{K^0_S}/\sigma(d_{K^0_S})$ is varied to obtain a larger maximum significance, this step showed for $d_{K^0_S}/\sigma(d_{K^0_S}) > 9$, $\frac{S}{\sqrt{S+B}} = 20$ is reached.
- In the third step, the cut $d_{K^0_S}/\sigma(d_{K^0_S}) > 9$ is only applied, then the cut with 2^{nd} highest Significance ranked in step 2, $\mathcal{LR}_{\pi^0} < 0.71$ is varied to reach a higher significance, thus for $\mathcal{LR}_{\pi^0} < 0.82$ we obtain $\frac{S}{\sqrt{S+B}} = 20.46$. Then we fix the value of the cut, $\mathcal{LR}_{\pi^0} < 0.82$ and vary the the 3^{rd} ranked cut to get a highest Significance again. Similarly done for the rest of variables.
- In the last step, all the optimized cuts after step 3 are applied, again expect the first ranked cut in step 2, $(d_{K^0_S}/\sigma(d_{K^0_S}) > 20)$ and vary it again to obtain a max significance. In this step, approximately the cut values remain the same for the same highest significance.

After all, a $\frac{S}{\sqrt{S+B}}$ 20.9 is reached in the signal region. In addition, test is done on the range of ΔE and Fisher discriminant $\mathcal{F}$, where the fitted errors of the CP-asymmetry parameters are compared for $\Delta E \in [-0.2, 0.2]$ and $\mathcal{F} > 0.3, 0.2, 0.1, 0$ and it showed that the range chosen for ΔE and $\mathcal{F} > 0$ is a good choice and compromise between background suppression and CP parameters.

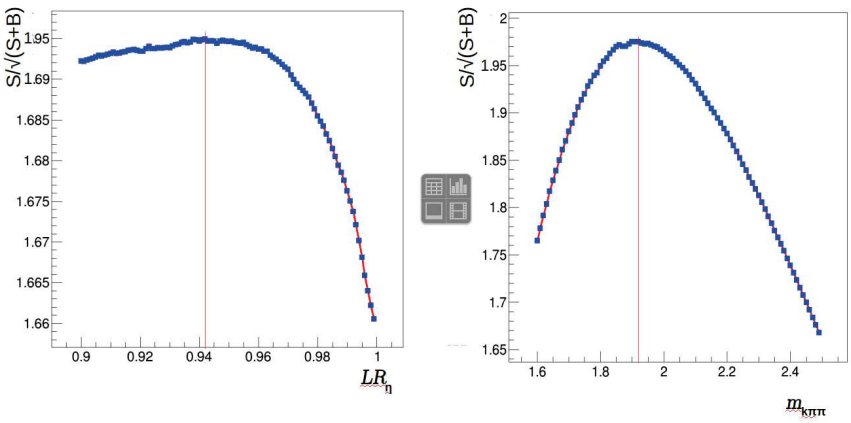


Figure 4.8: The $\frac{S}{\sqrt{S+B}}$distributions as function of the cuts variables range

Cut	**Value**
$m_{k\pi\pi}$(GeV/c^2)	x $<$ 1.8
$\mathcal{LR}_{\pi^0}$	x $<$0.82
$\mathcal{LR}_{\eta}$	x$<$ 0.954
B vertex probability	x$>$0.0001
ΔE (GeV)	-0.2 $\leqslant$ x $\leqslant$ 0.2
m_{ES} (GeV/c^2)	5.2 $<$ x
Fisher	x $>$ 0.0
$B_{\Delta t}$ (ps)	-20 $\leqslant$ x $\leqslant$ 20
$B_{\sigma_{\Delta T}}$ (ps)	x $<$ 2.5
$cos\theta_{\gamma}$	-0.65 $\leqslant$ x $\leqslant$ 0.85
$\lvert m_{\pi^+\pi^-} - m_{K^0_s}\rvert$ (GeV/c^2)	x $<$ 0.011
$cos\theta_{flight}$	0.995 $<$ x
$d_{k^0_s}/\sigma(d_{K^0_s})$	x $>$ 9
π_1 PID	π_1 PIDpi $>$ 0.34
π_2 PID	π_2 PIDpi $>$ 0.34
$m_{\pi^+\pi^-}(\rho^0(770)$selection) (GeV/$c^2$)	0.6 $\leqslant$ x $\leqslant$ 0.9

Table 4.2: List of the selection cuts used for $B^0 \to K^0_S\pi^+\pi^-\gamma$

Cut	Value
$\mathcal{LR}_{\pi^0}$	x $<$ 0.84
$\mathcal{LR}_{\eta}$	x$<$ 0.91
ΔE (GeV)	-0.25 $\leqslant$ x $\leqslant$ 0.2
m_{ES} (GeV/c^2)	5.2 $<$ x
Fisher	x $>$ 0.0
$B_{\Delta t}$ (ps)	-20 $\leqslant$ x $\leqslant$ 20
$B_{\sigma_{\Delta T}}$ (ps)	x $<$ 2.5
$cos\theta_{\gamma}$	-0.6 $\leqslant$ x $\leqslant$ 0.85
$\lvert m_{\pi^+\pi^-} - m_{K^0_s}\rvert$	x $<$ 0.016
$M_{K_s\pi 0}$ (GeV/c^2)	x $<$ 1.2
$d_{k^0_s}/\sigma(d_{K^0_s})$	x $>$ 5
π_1 PID	π_1 PIDpi $>$ 0.34
π_2 PID	π_2 PIDpi $>$ 0.34
Photons Energy from π^0 (GeV)	x $>$ 0.04

Table 4.3: List of the selection cuts used for $B^0 \to K^0_S\pi^0\gamma$

$B^0 \to K^0_S\pi^0\gamma$ cuts optimization

The method used to optimize the cuts for $B^0 \to K^0_S\pi^0\gamma$ channel is the same used for $B^0 \to K^0_S\pi^+\pi^-\gamma$, where in the signal region (i.e $M_{bc} > 5.26\,\text{GeV}/c^2$ and $-0.2 < \Delta E < 0.1$) the cut with highest $\frac{S}{\sqrt{S+B}} = 20$, $\mathcal{LR}_{\pi^0} < 0.8$ is optimized as well as all the cuts used for $B^0 \to K^0_S\pi^0\gamma$ selection from table 4.3, expect M_{bc}, ΔE, Δt, $\sigma_{\Delta t}$ and CSMVA. After the same full optimization method, a $\frac{S}{\sqrt{S+B}} = 20.6$ is reached.

Cuts Optimization result

As will be shown in the next section, a four dimensional fit to M_{bc}, ΔE, Δt and Fisher is done to extract the CP parameters $\mathcal{S}$ and $\mathcal{A}$. This fit has been done before and after the optimization of the cuts. The final result shown in section 4.4 shows the results using the optimized cuts. These results of the CP parameters statistical uncertainties have been decreased by 10% of their values after fitting using the optimized cuts.

4.3.6 Multiple candidate selection

To select a single candidate in each event where more than one is reconstructed and passes the selection criteria, χ^2 the "B-vertex-probability" cut is used to select the best candidate. The technique is mainly carried out by ranking the candidates for each event according to their probability, then choosing the best candidate corresponding to the best χ^2). This method is used for both TDCPV channels.

4.4 Fit to M_{bc}, ΔE, Δt and Fisher

In this section, we present the fit performed on M_{bc}, ΔE, the Fisher discriminant and Δt in order to extract the CP asymmetry parameters of the signal. The section 4.4.1 and 4.4.2 detail the PDFs used in the fit model for the signal and background categories, respectively. Same PDFs are used in both channels, In section 4.4.4 gives the CP asymmetries extracted by the fit.

4.4.1 Signal PDFs

PDFs for truth matched signal events are constructed using the signal MC sample, where the M_{bc} PDF, $\mathrm{P}_{M_{bc}}$ is described by a Crystal Ball function, the ΔE PDF, $\mathrm{P}_{\Delta E}$ by also a Crystal Ball and the Fisher discriminant, P_{CS} by sum of two Crystal Ball functions. The Δt signal PDF is defined in 5.7, where Δt resolution $\mathcal{R}_{sig}(\Delta t)$ is modeled by three Gaussians.

4.4.2 Background PDFs

Here we present the probability density functions of the two background categories, $B\bar{B}$ background and continuum background. The same functions have been used for both channels, while parameters extracted from the individual fits to each contribution changes and get fixed in the final four dimensional fit. Starting with the $B\bar{B}$ background, the M_{bc} PDF, $\mathrm{P}^{B\bar{B}}_{M_{bc}}$ is described by a sum of a gaussian and argus functions. ΔE PDF, $\mathrm{P}^{B\bar{B}}_{\Delta E}$ by a first order chebychev function. The Fisher discriminant, $\mathrm{P}^{B\bar{B}}_{CS}$ by a Crystal Ball. The Δt $B\bar{B}$ background PDF is described by a sum of three Gaussian distributions. The continuum $\mathrm{P}^{cont}_{M_{bc}}$ is modeled by an Argus function, ΔE $\mathrm{P}^{cont}_{\Delta E}$ by Chebychev function and P^{cont}_{CS} by a Gaussian. The Δt $B\bar{B}$ background PDF is described by a sum of three Gaussian distribution.

4.4.3 Signal to background fraction fit

In order to fit the CP violation parameters, the four dimensional fit, requires estimation of the fraction of the signal candidates among all candidates reconstructed in the full simulated data. First as discussed above, we model the distributions of signal and background candidates for M_{bc} and ΔE, where the specified models are used in this fit. Then we build a PDF as a sum of these two models

$$P(M_{bc}, \Delta E) = f_{sig} P_{sig}(M_{bc}, \Delta E) + (1 - f_{sig}) P_{bkg}(M_{bc}, \Delta E) \tag{4.16}$$

4.4.4 Results

In this section, we present the projections and CP violation parameters obtained from the four-dimensional fit already presented above. Figure 4.10 and 4.9 shows

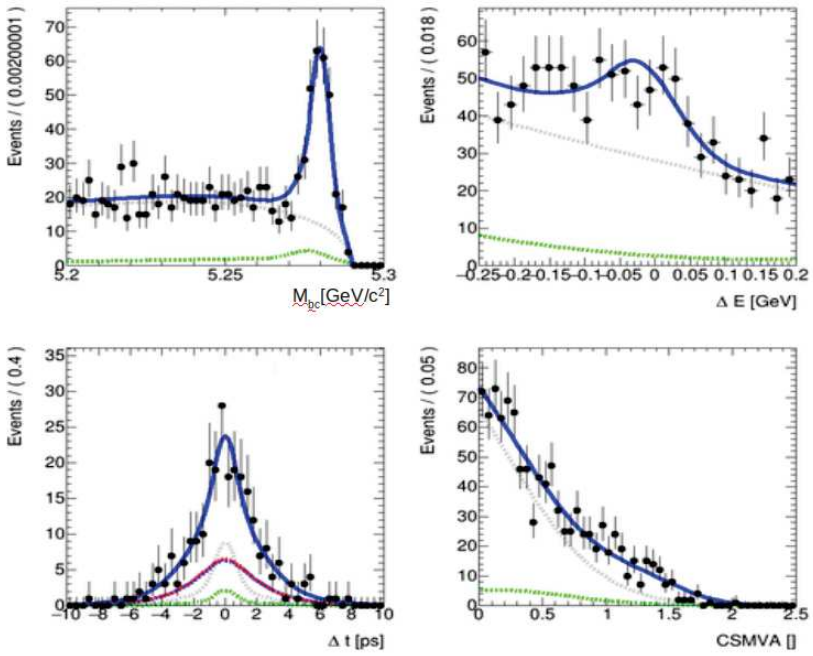


Figure 4.9: Projection of the four dimensional fit to each of M_{bc}, ΔE, Δt, CSMVA for $B^0 \to K^0_S\pi^0\gamma$. The fit is done using simulated data of 1 ab^{-1}. The combined probability distribution function is represented by the solid blue line while the two components are represented by a dotted green for $B\overline{B}$ background and dotted gray for continuum background.

the projection of fit on each of M_{bc}, ΔE, Δt and CSMVA for the both $B^0 \to K^0_S\pi^+\pi^-\gamma$ and $B^0 \to K^0_S\pi^0\gamma$ channels.

The full PDF used in the fit is as follows:

$$P_{full} = f_{sig}P_{sig}(M_{bc}, \Delta E, \Delta t, CSMVA) + (1 - f_{sig})[f_{BB}P_{\overline{b}}(M_{bc}, \Delta E, \Delta t , CSMVA) + (1 - f_{BB})P_{cont}(M_{bc}, \Delta E, \Delta t, CSMVA)] \tag{4.17}$$

where f_{sig} is the fraction of the signal events in the sample, it is calculated using two dimensional fit of M_{bc} and ΔE. f_{BB} is the fraction of the $B\overline{B}$ events, it is fixed in the final fit using also the 2D fit. P_{sig} is the four dimensional pdfs of the signal M_{bc}, ΔE, CSMVA, Δt obtained as a product

$$P_{sig}(M_{bc}, \Delta E, \Delta t, CSMVA) = P_{sig}(M_{bc}) \times P_{sig}(\Delta E) \times P_{sig}(\Delta t) \times P_{sig}(CSMVA) \tag{4.18}$$

the same form takes the BB pdf background P_{BB} and continuum P_{cont}. The CP violation parameters appear in $P_{sig}(\Delta t)$ defined in 5.7, where in P_{full} $\mathcal{A}$ and $\mathcal{S}$ are left free, while all other parameters are fixed from simulated data, plus some other parameters left free to account possible difference between data used in the final fit and simulated one. The fitted CP violation parameters are shown in table 4.4.

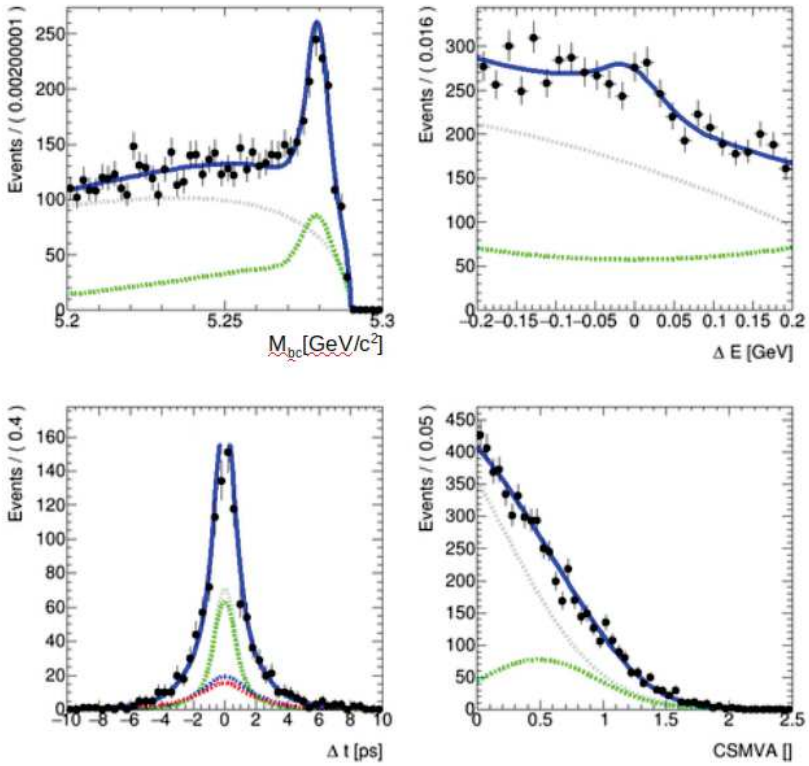


Figure 4.10: Projection of the four dimensional fit to each of M_{bc}, ΔE, Δt, CSMVA for $B^0 \to K^0_S\pi^+\pi^-\gamma$. The fit is done using simulated data of 1 ab^{-1}. The combined probability distribution function is represented by the solid blue line while the two components are represented by a dotted green for $B\overline{B}$ background and dotted gray for continuum background.

Parameter	Value
$\mathcal{S}_{B^0\to K^0_S\pi^+\pi^-\gamma}$	-0.09 ± 0.2
$\mathcal{A}_{B^0\to K^0_S\pi^+\pi^-\gamma}$	-0.21 ± 0.17
$\mathcal{S}_{B^0\to K^0_S\pi^0\gamma}$	0.02 ± 0.30
$\mathcal{A}_{B^0\to K^0_S\pi^0\gamma}$	0.03 ± 0.19

Table 4.4: *CP* violation parameters fitted from the four dimensional fit shown in Figures 4.10 and 4.9

4.5 Systematics $B^0 \to K^0_S \pi^0 \gamma$

One of my main contributions to the TDCPV analysis, in addition to the cuts optimization is the systematic study. Several sources need to be studied in order to measure the expected systematic uncertainty on the fitted CP violation parameters $\mathcal{S}$ and $\mathcal{A}$. In this section, the different sources are listed and discussed as follows and then finally summarized in table 4.5.

- **Flavor tagging**: In order to take into account the systematics due to flavour tagging, the parameter dw, the fraction of wrongly tagged candidates is varied by 0.1 %.
- **Fitting procedure**: Several parameters are fixed in the four dimensional fit done using P_{all}, we need to take into account the possible effects of fixing these parameters, thus they are varied by 1 sigma, where sigma is the error taken from the separate fits done to model each distribution component. Eor each varied parameter, the difference between the nominal $\mathcal{S}$ and $\mathcal{A}$ is obtained. Then these differences are added in quadrature to obtain a single uncertainty due to fixing these parameters.
- **Signal and Background fraction**: Signal fraction f_{sig} is obtained using a two dimensional fit to M_{bc} and ΔE, to study the impact of fixing it in the final four the fraction is varied by 10% and the difference between the obtained value of $\mathcal{S}$ and $\mathcal{A}$ and the initial one is taken as systematic uncertainty.
- **Resolution function parametrization**: The resolution function used in the analysis is modeled by three gaussians functions, when fitted on simulated data, some parameters are extracted and fixed in the final fit, thus to study this effect, these parameters by 1 sigma, then the uncertainties are summed in quadrature to obtain a single uncertainty.
- CP **violation effect from** $B\bar{B}$ **background**: The expected amount of $B\bar{B}$ events in the K* region (where $M_{K^0_S \pi^0}$) is very small 6 % of total signal, where only neutral B (especially $B^0 \to X_{s0}\gamma$) can contribute to an uncertainty in $\mathcal{S} \sim 0.008$ this value was taken from previous experiments(Belle and Babar), and small contribution for $C \sim 0.002$.
- **Physics parameters**: Parameters such as B^0 lifetime τ, and mixing parameter Δm are fixed in the final fit in $P_{sig}(\Delta t)$, thus they are varied by an errors taken from the PDG (2016) and take the difference between the new values of $\mathcal{S}$ and $\mathcal{A}$ after shifting the two parameters, then sum them in quadratic.
- **SVT alignment**: The K^0_S momentum direction is determined from the information from the silicon vertex detector (SVD), thus mistakes in its alignment would affect the results, this source is mode independent. The uncertainties are taken from Belle analysis studies assuming having the same effect as in Belle II.

Source	Δ S	ΔA
SVT Alignment	0.006	0.004
Physics Parameters	0.0066	0.008
Flavor tagging	0.005	0.002
Fitting procedure	0.015	0.016
Signal and Bkg fraction	0.00506	0.00680
Resolution function	0.0016	0.0015
CP from BB bkg	0.008	0.002
Tag Side interference	0.001	0.015
Total	0.02	0.024

Table 4.5: Table summarizing the different systematic sources and the systematic uncertainty assigned to each one, for the channel $B^0 \to K^0_S\pi^0\gamma$

Source	Δ S	ΔA
Physics Parameters	0.002	0.001
Flavor tagging	0.005	0.002
Fitting procedure of ΔE, m_{es} , Fisher discriminant	0.02	0.023
Signal and Bkg fraction	0.01	0.008
ΔT fitting procedure and Resolution function	0.012	0.007
Tag Side interference	0.001	0.015
CP violation effect from $B\bar{B}$ background	0.008	0.002
Total	**0.027**	**0.03**

Table 4.6: Table summarizing the different systematic sources and the systematic uncertainty assigned to each one, for the channel $B^0 \to K^0_S\pi^+\pi^-\gamma$

- **Tag side interference**: The interference between CKM-favored $b \to c\bar{u}d$ and doubly CKM suppressed $b \to uc\bar{c}d$ amplitudes in the tagging side B can effect time dependent CPV measurements. The uncertainties are taken from Belle that measures this effect by using the $D^{*+}L^-\overline{\nu}$ decay.

All these sources are summarized and summed in quadraticure in table 4.5, where the highest uncertainty comes from fitting procedure source, which shows thate importance of modeling the PDFs using real data is cricial to minimize the effects of fixing these PDFs in the final fit. Also the systematics in the $B^0 \to K^0_S\pi^+\pi^-\gamma$ have been studied and summarized in the next section.

4.5.1 Systematics $B^0 \to K^0_S\pi^+\pi^-\gamma$

The same sources as above have been studied the same way for $B^0 \to K^0_S\pi^+\pi^-\gamma$. tTable 4.6 summaries all the sources and the uncertainties and sum them in quadraticure assuming they are not correlated. The fitting procedure also has the highest uncertainty.

$\mathcal{S}$ **parameter**	$\mathcal{S}_{B^0\to K^0_S\pi^0\gamma}$	$\mathcal{S}_{B^0\to K^0_S\pi^+\pi^-\gamma}$
Belle II statistical uncertainty using 1 ab^{-1}	0.30	0.219
Belle statistical uncertainty	0.31	0.27
Expected uncertainty with Belle II 50 ab^{-1}	0.04	0.03
Belle II systematic uncertainty using 1 ab^{-1}	0.02	0.027
Belle systematic uncertainty	0.07	+0.04 /-0.07

Table 4.7: $\mathcal{S}$ parameter statistical uncertainty comparison between the current Belle II analysis on simulated data and Belle latest results on the two channels $B^0 \to K^0_S\pi^+\pi^-\gamma$ and $B^0 \to K^0_S\pi^0\gamma$, plus the expectations with the full Belle II planned data set of 50 ab^{-1}.

4.5.2 Conclusion

As a conclusion to this analysis, a comparison with the statistical uncertainties reached by Belle is done. Table 5.14, reports the statistical uncertainties obtained in this analysis using Belle II simulated data of 1 ab^{-1} and the obtained uncertainties from latest Belle analysis for the same channels. The Belle II results are similar or slightly better than the Belle ones. This is an important finding, which demonstrates that the new Belle II vertex detector has the ability, in the simulation, to overcome the penalty of the lower boost available in SuperKEKB compared to the one prevailing at KEKB-Belle. The next chapter will explore the current status of vertexing in Belle II with a measure on real data.
Regarding expectations for the full Belle II data set of 50 ab^{-1}, it appears that the measurement will still be statistically limited. Of course, this a preliminary investigation into the Belle II experiment performances. Already more advanced analysis tools are developed and they shall naturally increase the statistical power of TDCPV measurements.

CHAPTER 5

B^0 lifetime

5.1 Introduction

In this chapter, a new full analysis is presented, the B^0 lifetime measurement. As already revealed in Chapter 4, in TDCPV measurement, vertexing is the key to increase the sensitivity to time dependent analysis. To demonstrate the vertexing ability in Belle II, an analysis that measures the B^0 lifetime measurement, τ using the time difference measured between the two B^0 and $\bar{B}^0$ pair will be a tool to cross-check the vertex fitting tools and time resolution modeling. This measurement is done using the early Phase3 dataset and fully reconstructed hadronic final states.

We follow a standard analysis procedure sharing similarities with the TDCPV analysis according to the following overview. Similar to the TDCPV analysis, *signal side B* meson candidate is fully reconstructed but with hadronic decay final states. The rest-of-event technique allows to reconstruct the vertex position of the other B meson, still called *tag side* even if it is not used for tagging as the case in TDCPV analysis. The signal fraction estimation method is similar to the one used in TDCPV analysis, using a 2D fit to the M_{bc} and ΔE distributions. Lifetime parameter τ is measured using a one dimensional fit to the time distribution. Each of the three time distributions, for signal, continuum and $b\bar{b}$ background are modeled. Nevertheless we developed a common functional for the time resolution model, adjusting the parameters specifically for each contributions. The functional form of the resolution model is set to be simple as it is

the first modeling in starting Belle II analysis.

5.2 Datasets used

Simulations correspond to the Phase3 generic $\Upsilon(4S)$ `MC13` sample, with 100 fb^{-1}. For real data, early Phase3 experiments of 2019 processing which amount to an integrated luminosity of about 10 fb^{-1} is used.

5.3 Event selection and reconstruction

5.3.1 Signal side

In this section, the reconstruction part of the analysis is presented in detail, starting from the final state particles reconstructed. Table 5.1 lists the hadronic final states, charge conjugate are implicitly assumed all along this chapter. Information on the vertex fit method and cuts specific to the channel are also provided. Whenever the `TreeFitter` is mentioned as the vertex fit tool, it is used without constraint from the interaction point and without constraining the mass of the intermediate particles.

Pions and kaons are identified as follows:

- The distance from the charged particle track to the interaction point in the $r-\phi$ plane transverse to the beam is required to be less than 0.50 cm, and the track's z position from the interaction point is less than 3.0 cm. A selection based on particle identification likelihoods is used to identify $\pi^{\pm}$ and $K^{\pm}$.
- Charged pions coming from the $\rho^{\pm}$ or directly from the B_d meson have an additional requirement: the momentum in the $\Upsilon(4S)$ center-of-mass frame of the mother particle must be larger than 0.20 GeV/c.
- π^0 candidates are formed from pairs of photons, with each photon having an energy greater than 30 MeV, 80 MeV, or 120 MeV if reconstructed in the barrel region, backward end-cap region, or forward end-cap region, respectively. The angle difference between the momenta of the two photons is required to be less than 0.90 radians and less than 1 radian for the angle in the $r-\phi$ plane. The π^0 mass is required to be between 121 and 142 MeV/c^2; subsequently, a mass constrained fit is then performed and only candidates surviving the fit pass through the selection.

D^0 and D^- reconstruction

Three decay modes $D^0 \to K^-\pi^+$,$D^0 \to K^-\pi^+\pi^0$,$D^0 \to K^-\pi^+\pi^+\pi^-$ are used to reconstruct D^0, and $D^- \to K^+\pi^-\pi^-$ is used to reconstruct D^-. The standard deviation of the invariant mass distributions is ~ 15 MeV/c^2.

Decay	Selection Criteria
	B^0 decays
$B^0 \to D^- \pi^+$ $B^0 \to D^- \rho^+$ $B^0 \to D^{*-} \pi^+$ $B^0 \to D^{*-} \rho^+$	$M_{bc} > 5.2\,\text{GeV}/c^2$ and $-0.2 < \Delta E < 0.2\,\text{GeV}$
	D decays
$D^{*+} \to D^0 \pi^-$	$0.143 < m_{D^{*+}} - m_{D^0} < 0.147\,\text{GeV}/c^2$
$D^- \to K^+ \pi^- \pi^-$	$\lvert m - m_{PDG} \rvert < 0.015\,\text{GeV}/c^2$
$D^0 \to K^- \pi^+$ $D^0 \to K^- \pi^+ \pi^0$ $D^0 \to K^- \pi^+ \pi^+ \pi^-$	$\lvert m - m_{PDG} \rvert < 0.015\,\text{GeV}/c^2$
	ρ decay
$\rho^+ \to \pi^+ \pi^0$	$\lvert m - m_{PDG} \rvert < 0.10\,\text{GeV}/c^2$

Table 5.1: List of hadronic final states used to reconstruct B-meson decays.

D^{*+} reconstruction

D^{*+} candidates are formed by combining D^0 and a soft π^+, To demonstrate the selection cuts used for in the table for D^{*+}, distributions of the mass difference ΔM $(M_{D^0\pi^+} - M_{D^0})$ for D^{*+} candidates is shown in Fig 5.1 where the cut choice is taken according to the signal contributions in these distributions.

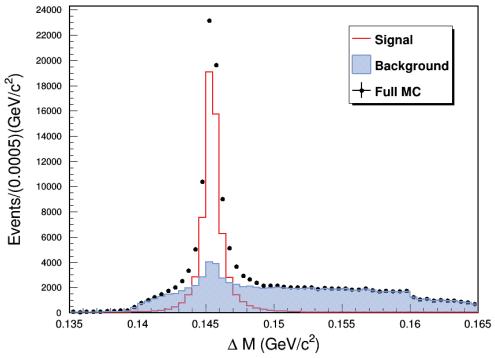


Figure 5.1: Distribution of mass difference $\Delta M_{D^{*+}} = M_{D^0\pi^+} - M_{D^0}$ for D^{*+} candidates in simulated data.

5.3.2 Tag side

In order to reconstruct the vertex of the second $B^0/\bar{B}^0$ in the event. An algorithm that uses all candidates left after reconstruction of the signal side, the vertex is reconstructed if two or more tracks are available with quality track cuts.

5.3.3 Signal and Tag side vertex fit

The fit to the signal and tag side vertices is performed as follows. The *signal side* vertex is reconstructed from the hadronic decays listed in Table 5.1 using a kinematic fit of the whole signal decay chain [40]. The *tag side* vertex position is determined from the tracks not used to reconstruct the signal side with an adaptive vertex fitter that accounts for the bias due to secondary decays [41].

5.3.4 Efficiencies

Efficiencies for reconstructing and selecting a given decay chain are evaluated with simulated data of 1 million signal events samples . The absolute efficiency is reported for each channel in table 5.2.

Decay	Selection efficiency %
$B^0 \to D^- \pi^+$	51.5 ± 0.2
$B^0 \to D^- \rho^+$	21.4 ± 0.2
$B^0 \to D^{*-} \pi^+$	22.8 ± 0.2
$B^0 \to D^{*-} \rho^+$	38.4 ± 0.22

Table 5.2: Selection efficiencies of studied processes, calculated using Phase 3 simulated data.

5.3.5 Continuum suppression

Rejection of the continuum events is done using two cuts, applied for all final states. Figure 5.2 shows the powering separation of these two variables, where R2 is the ratio between the 2-nd and 0-th Fox-Wolfram moments and $\cos\theta_{\text{thrust}}$ are defined and detailed in section 4.3.4.

- $R_2 < 0.3$,
- $\cos\theta_{\text{thrust}}$(cosine of angle between thrust axis of the signal B^0 and thrust axis of rest of event) < 0.8.

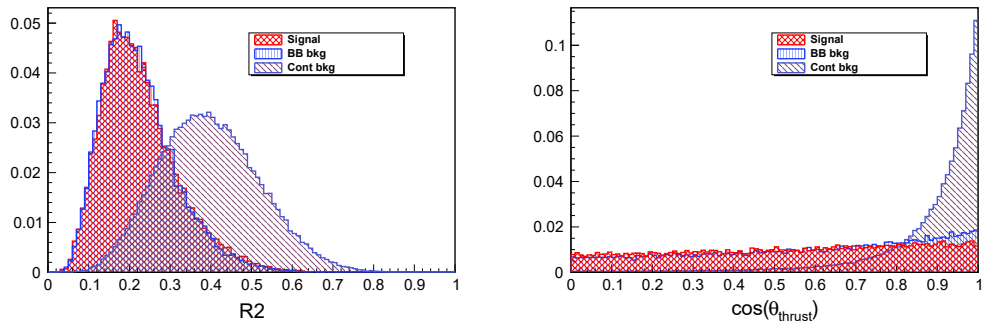


Figure 5.2: (*left*) R2 and (*right*) $\cos\theta_{\text{thrust}}$ distributions in simulated data

5.3.6 Regions defined

The fitted region, signal region, and sideband region are defined as follows:

- Fit region $M_{bc} \in [5.20, 5.29]$ GeV/c^2 and $\Delta E \in [-0.20, 0.15]$ GeV
- Signal region: $M_{bc} \in [5.27, 5.29]$ GeV/c^2 and $\Delta E \in [-0.07, 0.05]$ GeV
- Sideband region: $M_{bc} \in [5.20, 5.26]$ GeV/c^2 and $\Delta E \in [-0.20, -0.10] \cup [0.10, 1.50]$ GeV and $R_2 > 0.4$ and $\cos\theta_{\text{thrust}} < 0.8$

5.3.7 Multiple candidates

After the full selection about 10% of events present multiple candidates in the region that will be used for the M_{bc}–ΔE fit of Section 5.4. This number decreases to 5% in the signal region used for the lifetime fit of Section 5.5 (Figure 5.3). Thus, the effect of this multiple candidates will be negligible enough to ignore and in the following sections all the candidates are kept.

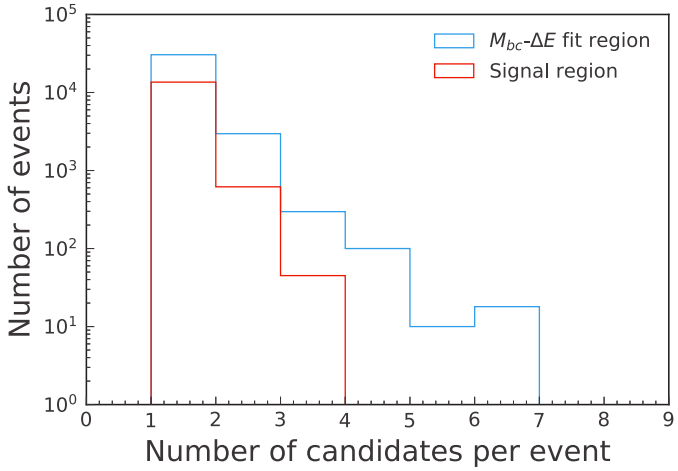


Figure 5.3: Distribution of the number of events with multiple candidates at the end of the selection in simulated data .

5.3.8 Time difference between the two B mesons

Recalling the definition of the proper time difference $\Delta t = t_{sig} - t_{tag}$ between the two B meson candidates (*signal* and *tag*) is approximated from the distance Δz_{boost} between the two reconstructed vertices along the collision boost direction $\vec{\beta}$ as follows;

$$\Delta t = \frac{\Delta z_{\text{boost}}}{\beta\gamma\, c}. \tag{5.1}$$

The $\Upsilon(4S)$ boost in the center of mass momentum yields an event-independent value of $\gamma\beta_\Upsilon = 0.28$.

For each event, the uncertainty $\sigma_{\Delta t}$ on the calculated Δt is computed. Candidates are required to pass two additional cuts,where the cut on $\sigma_{\Delta t}$ can be verified in Figure 5.4.

- $|\Delta t| < 8\,\text{ps}$,
- $\sigma_{\Delta t} < 3.5\,\text{ps}$.

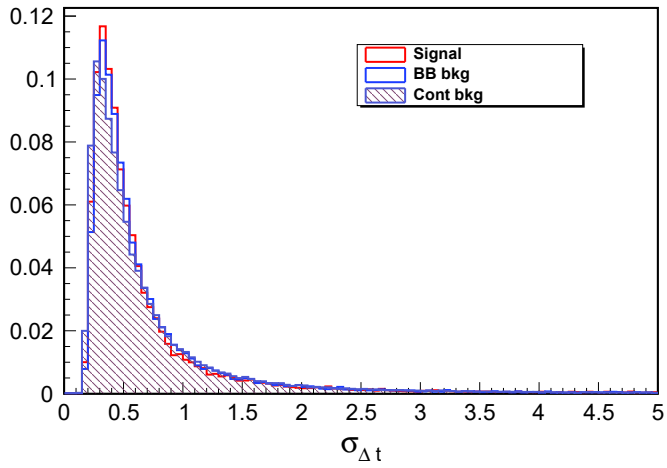


Figure 5.4: $\sigma_{\Delta t}$ distribution for simulated data

5.4 Fit to get signal and background fractions

In order to fit the time distribution model Δt, unbinned likelihood performed and defined later in equation 5.8, this PDF requires the number of events for each population in the data sample. Three different populations contribute to the selected sample: signal, $b\bar{b}$ background and continuum background. The contribution from each population is thus estimated from a 2D unbinned maximum likelihood fit of the B-meson constrained mass M_{bc} and ΔE distribution, this 2D fit has been developed by the Belle II-France member Giulio Dujany. In section 5.4.1, the probability distribution functions used to describe the three populations are presented, these PDFs are chosen using simulated samples containing only one population. Projections of the 2-D fit to each population is shown in Figures 5.5, 5.6 and 5.7 for all decay channels together, as well, their corresponding tables listing the parameters extracted from the fit. In section 5.4.2, the fit to extract the signal and background yields is presented, using simulated data and real data, plus a comparison between the yields obtained is shown.

The fits are performed over all decay channels used in this analysis considered without using a different distribution for each different decay channel. To check against possible biases, fits are also performed separately for each decay channel (see Table 5.3) and the sum of the yields coming from the different channels are compared with the yields from the common fit and found to be compatible. The fit projections for the fit on simulated data to the individual decay

channels can be found in Appendix 5.8. In the separate fits, due to the smaller sample size and the different shapes simpler distributions are often used as detailed in the sections.

Channel number	Decay channel
2	$B_d \to D^- \rho^+$
3	$B_d \to D^- \pi^+$
7	$B_d \to D^{*-} \rho^+ \, (D^0 \to K^- \pi^+)$
8	$B_d \to D^{*-} \rho^+ \, (D^0 \to K^- \pi^+ \pi^0)$
10	$B_d \to D^{*-} \pi^+ \, (D^0 \to K^- \pi^+)$
11	$B_d \to D^{*-} \pi^+ \, (D^0 \to K^- \pi^+ \pi^0)$

Table 5.3: Decay channels

5.4.1 Population distirbutions for M_{bc} and ΔE

Signal distribution for M_{bc} and ΔE

The signal is described by a Johnson's S_U distribution for both M_{bc} and ΔE distributions parameterized as

$$\mathcal{J}(x;\mu,\sigma,\gamma,\delta) \propto \frac{e^{-\frac{1}{2}\left(\gamma+\delta \, \sinh^{-1}(z)\right)^2}}{\sqrt{1+z^2}} \quad \text{with} \quad z = \frac{x-\mu}{\sigma}$$

Figure 5.5 shows the projections in M_{bc} and ΔE of the fit of all the channels together while the plots of the separate components can be found in section .4. The fit parameters are collected in Tables 5.4.

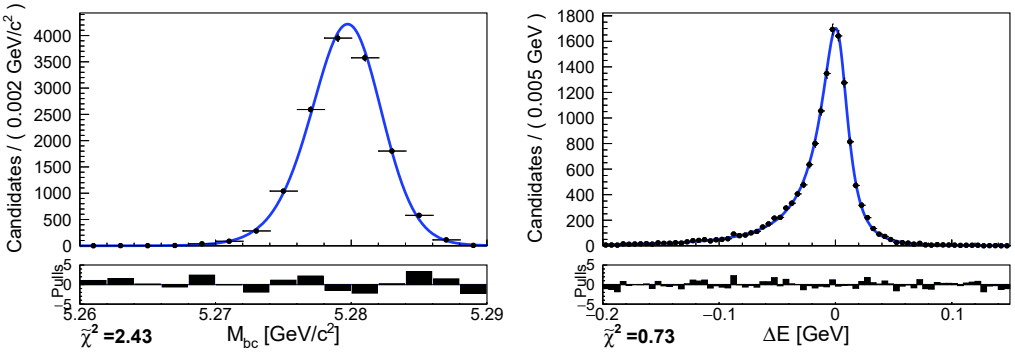


Figure 5.5: Projections of the 2-D fit to the signal MC sample for all the decay channels together: (*left*) M_{bc}, (*right*) ΔE.

	M_{bc}				ΔE			
Channel	μ [GeV/c^2]	σ [GeV/c^2]	γ	δ	μ [GeV]	σ [GeV]	γ	δ
2	5.2814 ± 0.0006	0.0070 ± 0.0008	0.68 ± 0.20	2.60 ± 0.27	0.0069 ± 0.0015	0.0273 ± 0.0017	0.81 ± 0.05	1.11 ± 0.05
3	5.2811 ± 0.0005	0.0081 ± 0.0009	0.61 ± 0.20	3.23 ± 0.34	0.00206 ± 0.00029	0.00788 ± 0.00028	0.278 ± 0.025	0.796 ± 0.018
7	5.285 ± 0.004	0.014 ± 0.004	2.0 ± 1.4	4.9 ± 1.6	0.0015 ± 0.0024	0.0244 ± 0.0029	0.67 ± 0.09	1.01 ± 0.09
8	5.2820 ± 0.0009	0.0069 ± 0.0012	0.91 ± 0.34	2.6 ± 0.4	-0.002 ± 0.004	0.047 ± 0.006	0.70 ± 0.13	1.49 ± 0.15
10	5.27961 ± 0.00007	0.0087 ± 0.0017	0.00 ± 0.28	3.4 ± 0.6	0.0017 ± 0.0006	0.0086 ± 0.0006	0.24 ± 0.05	0.85 ± 0.04
11	5.2842 ± 0.0027	0.014 ± 0.004	1.7 ± 1.1	5.6 ± 1.6	-0.0004 ± 0.0017	0.0268 ± 0.0020	0.49 ± 0.07	1.29 ± 0.08
All	5.28125 ± 0.00031	0.0078 ± 0.0005	0.64 ± 0.12	2.99 ± 0.19	0.00383 ± 0.00028	0.01200 ± 0.00032	0.580 ± 0.017	0.796 ± 0.014

Table 5.4: Fit parameters signal MC fits

$b\bar{b}$ background distribution for M_{bc} and ΔE

To better describe the correlation between M_{bc} and ΔE of the $b\bar{b}$ population, its distribution is separated in two components: one with a peaking shape and other one with a a continuum shape. That two components are then summed together (the parameter f denotes the relative normalization of the peeking component) as:

$$P_{b\bar{b}} = f\, P_{b\bar{b},\,peak} + (1-f) P_{b\bar{b},\,cont}$$

$P_{b\bar{b},\,peak}$ is described by a Johnson's S_U distribution in M_{bc} and by the sum of three Gaussian distributions in ΔE, parameterized as

$$f_1 \cdot \mathcal{G}(\Delta E; \mu, \sigma) + f_2 \cdot \mathcal{G}(\Delta E; \mu + d\mu, s \cdot \sigma) + (1 - f_1 - f_2) \cdot \mathcal{G}(\Delta E; \mu + d\mu', s' \cdot \sigma)$$

Where $\mathcal{G}(x; \mu, \sigma)$ denotes a Gaussian distribution with mean μ and width σ.

$P_{b\bar{b},\,cont}$ is described by an Argus distribution in M_{bc} as:

$$Argus(x) \propto t \cdot \sqrt{1-t^2} \cdot \exp[-\chi(1-t^2)] \quad \text{with} \quad t = \frac{x}{x_0}.$$

with $x_0 = 5.29\ \mathrm{GeV}/c^2$. The continuum shape is described by an exponential distribution in ΔE: $\exp(\alpha \cdot \Delta E)$.

In the separate fits only one or two Gaussian is used to describe the ΔE peeking component. Moreover for $B_d \to D^- \rho^+$the correlation between M_{bc} and ΔE is neglected and peeking and continuum components are added separately for M_{bc} and ΔE with different fractions (f for M_{bc} and f' for ΔE). Figure 5.6 shows the projections in M_{bc} and ΔE of the fit of all the channels together while the plots of the separate components can be found in Appendix .4. The fit parameters are collected in Tables 5.5.

Continuum background distribution for M_{bc} and ΔE

The continuum background is described by an Argus distribution for M_{bc} and an exponential distribution for ΔE. Figure 5.7 shows the projections in M_{bc} and ΔE

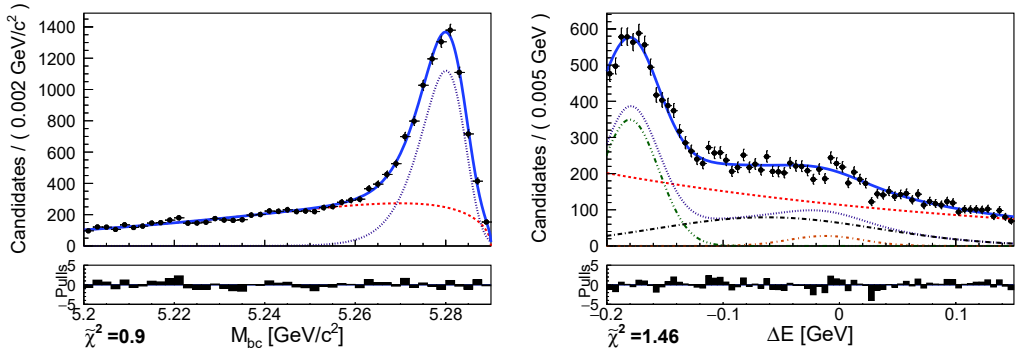


Figure 5.6: Projections of the 2-D fit to the $b\bar{b}$ MC sample for all the decay channels together: (*left*) M_{bc}, (*right*) ΔE.

	Peaking						Continuum		
	M_{bc}				ΔE		M_{bc}	ΔE	
Channel	μ [GeV/c^2]	σ [GeV/c^2]	γ	δ	μ [GeV]	σ [GeV]	χ	α [GeV^{-1}]	f
2	5.2900 ± 0.0014	0.0070 ± 0.0014	2.7 ± 0.5	2.00 ± 0.16	-0.1784 ± 0.0027	0.0105 ± 0.0020	-55 ± 7	-2.93 ± 0.17	0.31 ± 0.04
3	5.2900 ± 0.0006	0.0086 ± 0.0006	2.87 ± 0.30	2.61 ± 0.11	-0.0519 ± 0.0032	0.0600 ± 0.0019	-65 ± 4	-3.72 ± 0.25	0.546 ± 0.014
7	5.2896 ± 0.0018	0.0070 ± 0.0018	5.0 ± 2.6	4.1 ± 0.6	-0.011 ± 0.004	0.038 ± 0.004	-100 ± 5	-2.7 ± 0.4	0.227 ± 0.022
8	5.2842 ± 0.0026	0.0035 ± 0.0017	2.2 ± 1.7	2.0 ± 0.6	-0.019 ± 0.005	0.0600 ± 0.0030	-97 ± 4	-2.70 ± 0.33	0.273 ± 0.021
10	5.289 ± 0.014	0.0089 ± 0.0020	2.9 ± 1.4	2.9 ± 0.7	-0.034 ± 0.007	0.049 ± 0.014	$(-1.2 \pm 0.5) \times 10^2$	-2.0 ± 3.1	0.943 ± 0.030
11	5.288 ± 0.004	0.0072 ± 0.0015	2.7 ± 1.6	2.4 ± 0.7	-0.032 ± 0.006	0.060 ± 0.005	-125 ± 14	-4.0 ± 0.9	0.69 ± 0.05
All	5.2900 ± 0.0006	0.0082 ± 0.0007	2.93 ± 0.09	2.58 ± 0.11	-0.012 ± 0.009	0.0316 ± 0.0032	-65.3 ± 2.3	-2.84 ± 0.14	0.450 ± 0.010

Channel	$d\mu$ [GeV]	s	$d\mu'$ [GeV]	s'	f_1	f_2	f'
2	–	–	–	–	–	–	0.030 ± 0.008
3	-0.1274 ± 0.0034	0.427 ± 0.019	–	–	0.291 ± 0.012	–	–
10	-0.145 ± 0.009	0.62 ± 0.24	–	–	0.25 ± 0.04	–	–
11	-0.142 ± 0.007	0.45 ± 0.06	–	–	0.458 ± 0.026	–	–
All	-0.052 ± 0.013	3.00 ± 0.14	-0.168 ± 0.009	0.78 ± 0.10	0.060 ± 0.022	0.472 ± 0.020	–

Table 5.5: Fit parameters $b\bar{b}$ MC fits

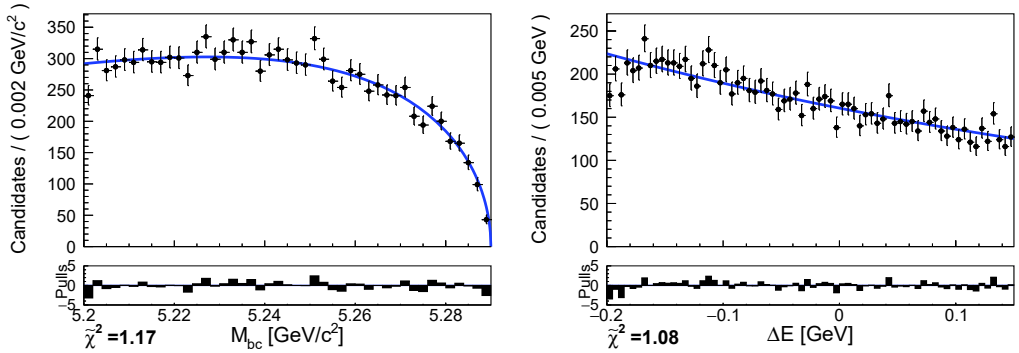


Figure 5.7: Projections of the 2-D fit to the continuum MC sample for all the decay channels together: (*left*) M_{bc}, (*right*) ΔE.

of the fit of all the channels together while the plots of the separate components can be found in Appendix .4. The fit parameters are collected in Table 5.6.

	M_{bc}	ΔE
Channel	χ	α [GeV^{-1}]
2	-23.8 ± 1.6	-1.73 ± 0.14
3	-20.1 ± 1.6	-1.84 ± 0.14
7	-17 ± 6	-1.0 ± 0.5
8	-1 ± 6	-1.2 ± 0.4
10	-22 ± 6	-2.1 ± 0.6
11	-21 ± 5	-0.8 ± 0.4
All	-20.7 ± 1.0	-1.69 ± 0.09

Table 5.6: Fit parameters continuum sample fits

5.4.2 Fit to M_{bc} and ΔE to extract the signal and background contributions

In the fit to extract the yields of the three different populations the distributions for the three components are fixed to the ones described in the previous sections. All the parameters are fixed except for the three yields and the mean and the width of a Gaussian of the signal population to account for the possible data-MC difference. The mean of the other peaking components are also shifted by fixing their differences with respect to the mean left floating to the values from simulation. The scaling value between the width of the peeking components and the width left floating is also fixed from simulation. Figure 5.8 shows the projections in M_{bc} and ΔE of the fit on MC while Figure 5.9 shows the projections of the fit on data. The fit projections for the fit on MC to the individual decay channels can be found in Appendix .4. Table 5.7 collects the fit parameters. Table 5.8 compares the yields of the three components obtained from the fit

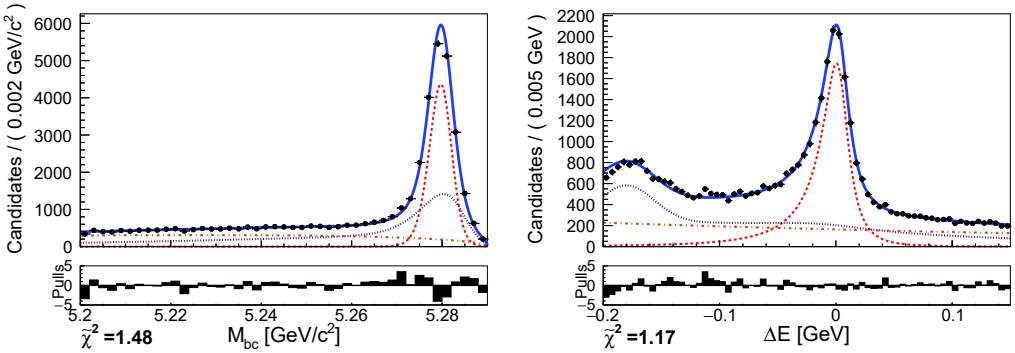


Figure 5.8: Projections of the 2-D fit to the MC sample for all the decay channels together to extract the yields of the different components: (*left*) M_{bc}, (*right*) ΔE. The combined probability distribution function is represented by the solid blue line while the three components are represented by a dashed red for the signal, a dotted purple for the $b\bar{b}$ background and a dashed-dotted orange for the continuum background.

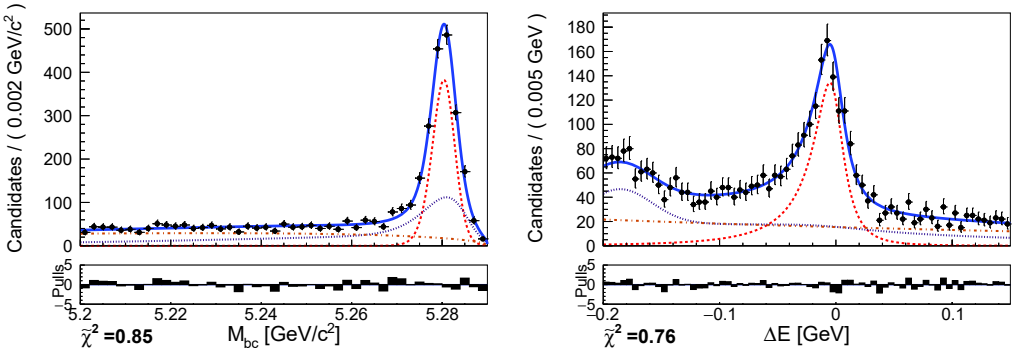


Figure 5.9: Projections of the 2-D fit to the data sample for all the decay channels together to extract the yields of the different components: (*left*) M_{bc}, (*right*) ΔE. The combined probability distribution function is represented by the solid blue line while the three components are represented by a dashed red for the signal, a dotted purple for the $b\bar{b}$ background and a dashed-dotted orange for the continuum background.

to the true ones from simulation. Table 5.9 contains the same information but for the signal region ($5.25 < M_{bc} < 5.29\,\text{GeV}/c^2$ and $-0.07 < \Delta E < 0.05\,\text{GeV}$) that is shown in Figure 5.11. A satisfactory agreement between fit and true value is obtained in every decay channel and also combining all the decay channels together (Figure 5.10). Moreover there is a good agreement between the yields obtained from the common fit and the sum of the yields of the individual fits.

				M_{bc}		ΔE	
Channel	n_{sgn}	$n_{b\bar{b}}$	n_{cont}	μ [GeV/c^2]	σ [GeV/c^2]	μ [GeV]	σ [GeV]
2	$(3.11 \pm 0.08) \times 10^3$	$(5.95 \pm 0.20) \times 10^3$	$(4.82 \pm 0.18) \times 10^3$	5.28121 ± 0.00007	0.00648 ± 0.00012	0.0068 ± 0.0006	0.0246 ± 0.0007
3	$(5.18 \pm 0.08) \times 10^3$	$(5.96 \pm 0.12) \times 10^3$	$(4.95 \pm 0.11) \times 10^3$	5.28105 ± 0.00004	0.00789 ± 0.00008	0.00216 ± 0.00017	0.00775 ± 0.00012
7	$(8.3 \pm 0.5) \times 10^2$	$(9.5 \pm 0.8) \times 10^2$	$(3.3 \pm 0.5) \times 10^2$	5.28491 ± 0.00019	0.0133 ± 0.0004	0.0015 ± 0.0010	0.0227 ± 0.0010
8	$(1.16 \pm 0.06) \times 10^3$	$(1.54 \pm 0.10) \times 10^3$	$(5.7 \pm 0.5) \times 10^2$	5.28199 ± 0.00010	0.00681 ± 0.00020	-0.0017 ± 0.0012	0.0459 ± 0.0018
10	$(1.40 \pm 0.04) \times 10^3$	520 ± 27	307 ± 20	5.27959 ± 0.00007	0.00855 ± 0.00015	0.00170 ± 0.00033	0.00861 ± 0.00024
11	$(1.78 \pm 0.05) \times 10^3$	$(1.06 \pm 0.05) \times 10^3$	547 ± 32	5.28401 ± 0.00010	0.01383 ± 0.00026	-0.0003 ± 0.0006	0.0259 ± 0.0007
All	$(1.352 \pm 0.014) \times 10^4$	$(1.574 \pm 0.024) \times 10^4$	$(1.171 \pm 0.020) \times 10^4$	5.281140 ± 0.000028	0.00744 ± 0.00005	0.00390 ± 0.00016	0.01155 ± 0.00014
Data	$(1.22 \pm 0.04) \times 10^3$	$(1.29 \pm 0.07) \times 10^3$	$(1.14 \pm 0.06) \times 10^3$	5.28184 ± 0.00009	0.00746 ± 0.00017	-0.0013 ± 0.0006	0.0133 ± 0.0005

Table 5.7: Fit parameters of the fit to extract yields

Channel	n_{sgn}	$n_{b\bar{b}}$	n_{cont}	n_{sgn}^{true}	$n_{b\bar{b}}^{true}$	n_{cont}^{true}	$pull_{sgn}$	$pull_{b\bar{b}}$	$pull_{cont}$
2	$(3.11 \pm 0.08) \times 10^3$	$(5.95 \pm 0.20) \times 10^3$	$(4.82 \pm 0.18) \times 10^3$	3262	5794	4815	-2.1	0.76	0.01
3	$(5.18 \pm 0.08) \times 10^3$	$(5.96 \pm 0.12) \times 10^3$	$(4.95 \pm 0.11) \times 10^3$	5203	5958	4932	-0.33	0.032	0.2
7	$(8.3 \pm 0.5) \times 10^2$	$(9.5 \pm 0.8) \times 10^2$	$(3.3 \pm 0.5) \times 10^2$	866	905	345	-0.75	0.6	-0.26
8	$(1.16 \pm 0.06) \times 10^3$	$(1.54 \pm 0.10) \times 10^3$	$(5.7 \pm 0.5) \times 10^2$	1155	1555	560	0.023	-0.13	0.2
10	$(1.40 \pm 0.04) \times 10^3$	520 ± 27	307 ± 20	1395	525	308	0.15	-0.19	-0.029
11	$(1.78 \pm 0.05) \times 10^3$	$(1.06 \pm 0.05) \times 10^3$	547 ± 32	1811	1041	538	-0.58	0.41	0.27
Sum	$(1.345 \pm 0.015) \times 10^4$	$(1.599 \pm 0.027) \times 10^4$	$(1.153 \pm 0.022) \times 10^4$	13692	15778	11498	-1.6	0.76	0.14
All	$(1.352 \pm 0.014) \times 10^4$	$(1.574 \pm 0.024) \times 10^4$	$(1.171 \pm 0.020) \times 10^4$	13692	15778	11498	-1.2	-0.14	1
Data	$(1.22 \pm 0.04) \times 10^3$	$(1.29 \pm 0.07) \times 10^3$	$(1.14 \pm 0.06) \times 10^3$	–	–	–	–	–	–

Table 5.8: Fit yields. The row *Sum* contains the sum of the yields of the individual modes, the raw *All* contains the yields considering together all the modes while the raw *Data* contains the result of the fit to the data. The columns $pull_i$ are defined as $(n_i - n_i^{true})/\sigma_{n_i}$.

Channel	n_{sgn}	$n_{b\bar{b}}$	n_{cont}	n_{sgn}^{true}	$n_{b\bar{b}}^{true}$	n_{cont}^{true}	$pull_{sgn}$	$pull_{b\bar{b}}$	$pull_{cont}$
2	$(2.77 \pm 0.07) \times 10^3$	$(1.19 \pm 0.09) \times 10^3$	$(6.1 \pm 0.6) \times 10^2$	2840	1094	608	-0.99	1.1	-0.0081
3	$(5.03 \pm 0.08) \times 10^3$	$(1.00 \pm 0.05) \times 10^3$	$(6.0 \pm 0.4) \times 10^2$	5016	984	592	0.17	0.27	0.23
7	$(7.4 \pm 0.4) \times 10^2$	$(3.5 \pm 0.5) \times 10^2$	40 ± 17	764	302	36	-0.64	1.1	0.24
8	$(9.8 \pm 0.6) \times 10^2$	$(5.2 \pm 0.6) \times 10^2$	58 ± 17	970	506	59	0.17	0.31	-0.074
10	$(1.37 \pm 0.04) \times 10^3$	98 ± 12	38 ± 7	1350	99	42	0.43	-0.052	-0.61
11	$(1.69 \pm 0.05) \times 10^3$	297 ± 25	68 ± 11	1715	266	74	-0.48	1.2	-0.5
Sum	$(1.257 \pm 0.014) \times 10^4$	$(3.46 \pm 0.13) \times 10^3$	$(1.41 \pm 0.08) \times 10^3$	12655	3251	1411	-0.58	1.6	0.011
All	$(1.253 \pm 0.014) \times 10^4$	$(3.41 \pm 0.11) \times 10^3$	$(1.43 \pm 0.07) \times 10^3$	12655	3251	1411	-0.95	1.4	0.33
Data	$(1.10 \pm 0.04) \times 10^3$	270 ± 32	140 ± 21	–	–	–	–	–	–

Table 5.9: Fit yields in signal region. The row *Sum* contains the sum of the yields of the individual modes, the raw *All* contains the yields considering together all the modes while the raw *Data* contains the result of the fit to the data. The columns $pull_i$ are defined as $(n_i - n_i^{true})/\sigma_{n_i}$.

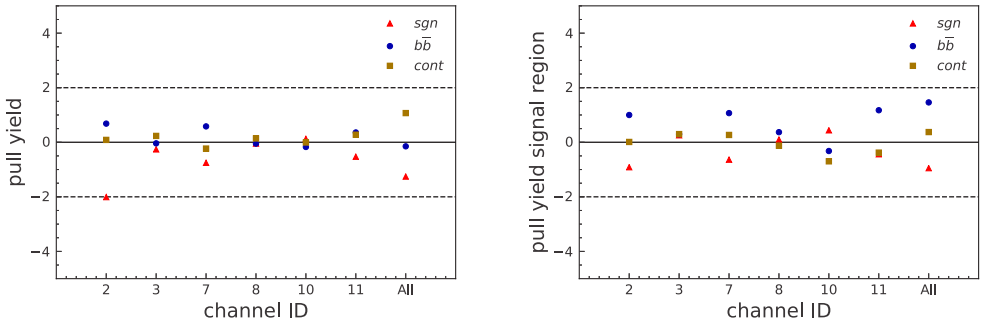


Figure 5.10: Difference between the yields estimated from the fit and the real ones divided by error on the yield estimated from the fit in (*left*) the full fit range and (*right*) the signal region.

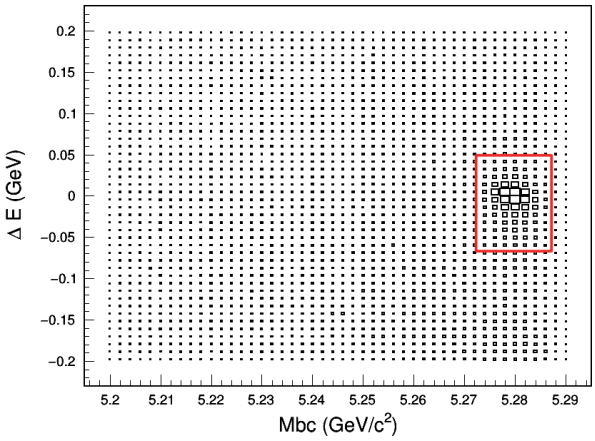


Figure 5.11: ΔE vs. M_{bc} two dimensional plots for all channels combined in simulated data. The region delimited by the red rectangle is the signal region used for the evaluation of the lifetime.

5.5 Lifetime extraction method

To measure B^0 lifetime from the selected candidates, an unbinned likelihood fit is performed on the overall Δt distribution. The probability distribution in equation (5.8) describes this overall distribution by combining the contribution yields measured in Section 5.4.

$$\mathrm{P}_{all}(\Delta t) = n_{sgn}\mathrm{P}_{sgn}(\Delta t) + n_{b\bar{b}}\mathrm{P}_{b\bar{b}}(\Delta t) + n_{cont}\mathrm{P}_{cont}(\Delta t). \tag{5.2}$$

The Δt distribution analytical models for the three main contributions to the candidate sample are described in section 5.5.1. The fits to Δt corresponding to each component is also shown. In section 5.5.2, the full Δt fit on simulated data using the model in equation 5.8 is presented as well parameters used and extracted from this fit. In section 5.5.3, the continuum modeling study on data is discussed. Finally, the lifetime full fit on real data is shown in section 5.6.

An important ingredient of the fit to extract the B lifetime is the resolution function $\mathcal{R}$ that describes the smearing introduced by various effects during the

reconstruction. In this analysis $\mathcal{R}$ is modeled by the sum of three Gaussian distributions (5.9).

$$\begin{aligned}\mathcal{R}(\delta_{\Delta t}) = f_1\mathcal{G}(\delta_{\Delta t};\mu_1,\sigma_1) + f_2\mathcal{G}(\delta_{\Delta t};\mu_1+dm,s_2\times\sigma_1)\\ +(1-f_1-f_2)\mathcal{G}(\delta_{\Delta t};\mu_1,s_2\times s_3\times\sigma_1)\end{aligned} \tag{5.3}$$

A universal resolution function is used and not a candidate-by-candidate one, depending for example on the uncertainty on Δt due to the small sample size considered in this analysis.

5.5.1 Modeling of Δt component for the three components

Continuum background and Δt distribution P_{cont}

Background candidates coming from light continuum events are not expected to display any specific time behavior. Their distribution can thus be described with same functional form than the resolution of equation (5.9): a sum of three Gaussian distributions. The candidates coming from $c\bar{c}$ events, that are considered in the continuum background, contain $D^{(*)}$ mesons which have a sizeable lifetime. However as the background coming from this sample is combinatorial in nature (there are no real B^0 so the $D^{(*)}$ mesons are associated with particles with the other side of the event) and the sample size considered is limited, three Gaussian distribution still provides a good description of the full combinatorial background as will be see by the goodness of the fit obtained.

The fit of the Δt distribution to a MC sample of continuum-events candidates is shown in Figure 5.12. Another fit is performed to a sideband designed to be dominated by continuum background defined by selecting $M_{bc} < 5.26$ GeV/c^2 and $|\Delta E| < 0.1$ GeV and inverting the continuum background selection to $R_2 > 0.4$ and $\cos\theta_{\text{thrust}} > 0.8$. In this region only 1% contamination from $b\bar{b}$ candidates is expected and there is a good agreement between the fit to the continuum sample selected using MC information and the fit to the sideband.

In the final fit (5.8) all the parameters of P_{cont}, the probability distribution function describing the continuum component, will be fixed from this sideband fit. This will be also be the strategy for the fit on data. There however, due to the limited sample size, only μ_1 and σ_1 will be left free in the data sideband fit while the others will be fixed to the value from the MC sideband fit. More details on the fit to the continuum Δt fit on data can be found in Section 5.5.3

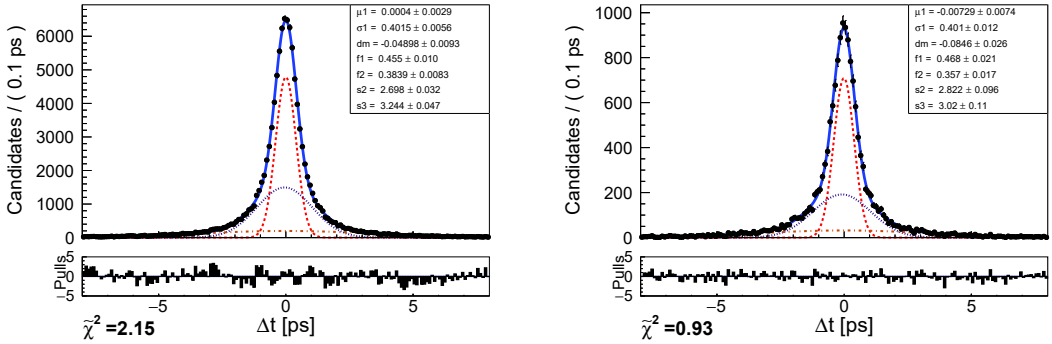


Figure 5.12: (*left*) Fit to the Δt distribution of only continuum background events and (*right*) fit to the Δt distribution of the sideband events in a full simulated data sample.

Signal Δt distribution Models P_{sgn}

The signal distribution, P_{sgn}, is modeled by the convolution between the distribution describing an exponential decay, $\mathcal{P}_{th}$ (5.4), and the resolution function $\mathcal{R}$ described in (5.9) as shown in equation (5.5).

$$\mathcal{P}_{th}(\Delta t) = \frac{1}{2\tau_B} \exp\Big(-\frac{|\Delta t|}{\tau_B}\Big). \tag{5.4}$$

$$P_{sig}(\Delta t) = \int_{-\infty}^{+\infty} \mathcal{P}_{th}(\Delta t')\mathcal{R}(\Delta t - \Delta t')\mathrm{d}\Delta t'. \tag{5.5}$$

To check potential bias in the reconstruction, the profile distribution of the residual on Δz (distance along z between the signal and tag vertex in the event) versus the true Δz for true reconstructed signal candidates is shown in Figure 5.13. A bias toward negative values is clearly visible. The reason for this

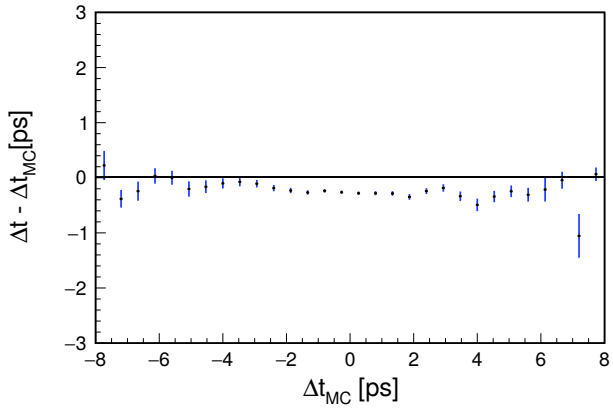


Figure 5.13: Profile plot of the Δt residual versus the true Δt in the simulation. Error bars correspond to the uncertainty on the mean.

bias can be understood considering separately the z vertex residuals for the signal and tag vertices. Figure 5.32 shows the two distributions fitted with the sum of three Gaussian distributions and the parameters are shown in table 5.10. It can be seen that the width and mean parameters for the tag side are wider than

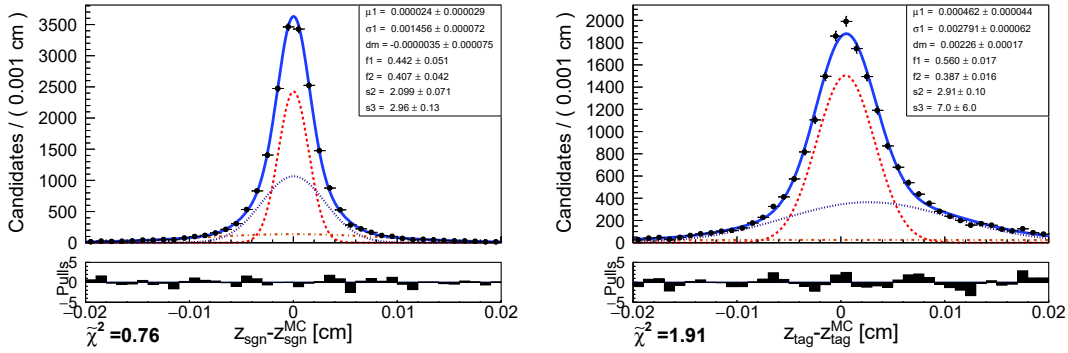


Figure 5.14: Fit to the z vertex residual for (*left*) the signal B and (*right*) the tag B.

for the signal. This effect is caused by the fact that on the signal side we have exclusive decays where the fitter `TreeFitter` takes correctly into account the charm meson lifetime since it simultaneously fits an entire decay chain. On the tag side, the inclusive decay of the other B is with `Rave`. A method to reduce the contributions from secondary decays is implemented in `Rave`, this method however is not perfect and leads to a bias toward larger lifetimes for the tag B that, as the signal B is unbiased, converts into a negative bias for Δt.

Parameter	Signal side	Tag side
$\mu 1$ [cm]	$(2.4 \pm 2.9) \times 10^{-5}$	$(4.62 \pm 0.44) \times 10^{-4}$
σ_1 [cm]	$(1.45 \pm 0.07) \times 10^{-3}$	$(2.79 \pm 0.06) \times 10^{-3}$
dm [cm]	$(0 \pm 8) \times 10^{-5}$	$(2.26 \pm 0.17) \times 10^{-3}$
f1	0.44 ± 0.05	0.560 ± 0.017
f2	0.41 ± 0.04	0.387 ± 0.016
s2	2.10 ± 0.07	2.91 ± 0.10
s3	2.96 ± 0.13	7 ± 6

Table 5.10: Parameters fitted from the fit to signal and tag side residuals in Fig 5.32

Figure 5.15 shows the fit to the residuals of Δt leaving all the parameters free. From this fit, one can calculate $\sigma_{\Delta t}$ = (weighted sum of the sigmas of each contributions) $\sim$ 1.1 ps. Similarly, one can calculate the resolution on the signal side vertex: $\sigma_{z_{sgn}}$ = (weighted sum of the sigmas of each contributions from table 5.10) $\sim$ 30 μm and for tag side: $\sigma_{z_{tag}} \sim$ 80 μm.

A fit is performed to extract the lifetime (Figure 5.16) on signal events. The only free parameters will be the lifetime itself and μ_1 and σ_1 of the resolution function while the other parameters can be fixed from the fit to the Δt distribution for the continuum events as shown in Figure 5.12. One can notice that the obtained value for the B^0 lifetime is compatible with the known one.

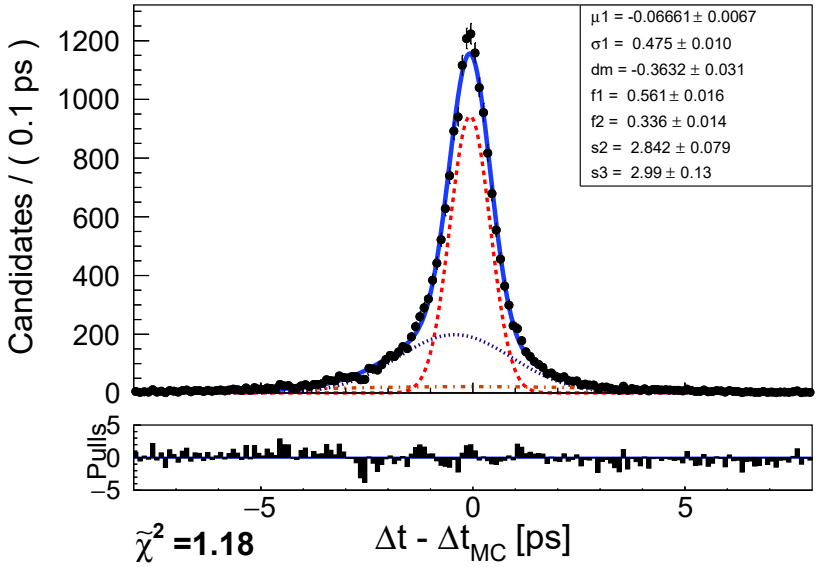


Figure 5.15: Fit to residual for the signal sample in simulated data leaving all the parameters free.

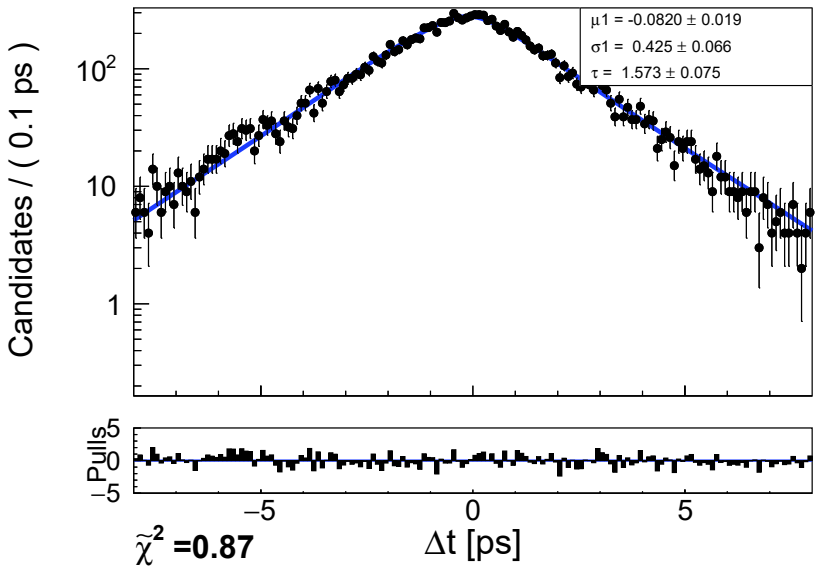


Figure 5.16: Fit to Δt distribution of the simulated signal sample.

$b\bar{b}$ background Δt distribution $\mathrm{P}_{b\bar{b}}$

Unlike in the continuum background case, the Δt distribution of the $b\bar{b}$ background events cannot be simply described by a sum of Gaussian distributions because, like in the signal case, the lifetime of the decaying B mesons cannot be neglected. Like in for the signal case the correct description will thus be the convolution of an exponential decay function with the resolution function as described in (5.6).

$$\mathrm{P}_{b\bar{b}}(\Delta t) = \int_{-\infty}^{+\infty} \frac{1}{2\tau_{eff}} \exp\Big(-\frac{|\Delta t'|}{\tau_{eff}}\Big)\mathcal{R}(\Delta t - \Delta t')\mathrm{d}\Delta t'. \tag{5.6}$$

The resolution function is exactly the same as the one used for the signal while instead of the B^0 lifetime an effective lifetime τ_{eff} is used.

Figure 5.17 shows the fit to the Δt distribution of $b\bar{b}$ events in the ΔE-M_{bc} signal range. The distribution in (5.6) is used. The parameters of the resolution function are fixed to the ones obtained from the signal fit shown in fig 5.15 and only the effective lifetime is left free. The fitted τ_{eff} value is 1.39 ± 0.064 ps and it will be fixed in the final fit.

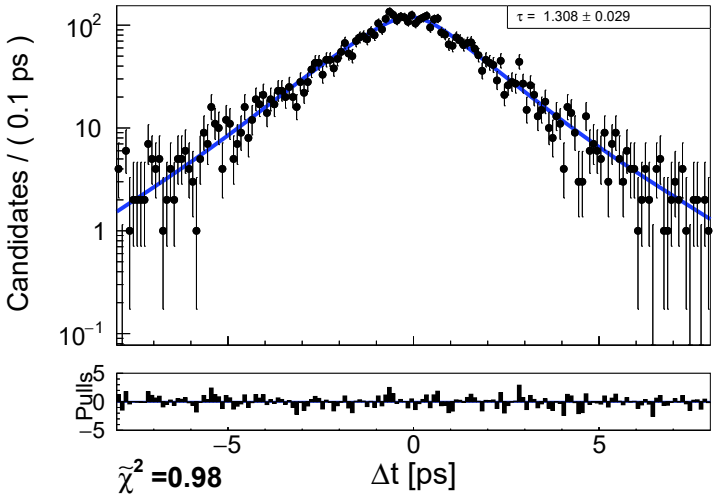


Figure 5.17: Distribution of Δt for the $b\bar{b}$ event contribution in the simulated data in the signal region. The superimposed fit follows the pdf defined in (5.6).

5.5.2 Full fit Δt distribution P_{all}

The B^0 lifetime is extracted with an unbinned maximum likelihood fit to the Δt distribution using (5.8) as model. The yields of the three populations are fixed to the ones obtained in Section 5.4. All the parameters of P_{cont} are fixed as explained in Section 5.5.1. P_{sgn} and $\mathrm{P}_{b\bar{b}}$ share the same resolution function whose parameters are all fixed to the ones obtained in Section 5.5.1 except for μ_1 and σ_1 (see Table 5.11). Figure 5.18 shows the result of this fit on the simulated sample. The obtained value of the B lifetime is compatible with the generated one.

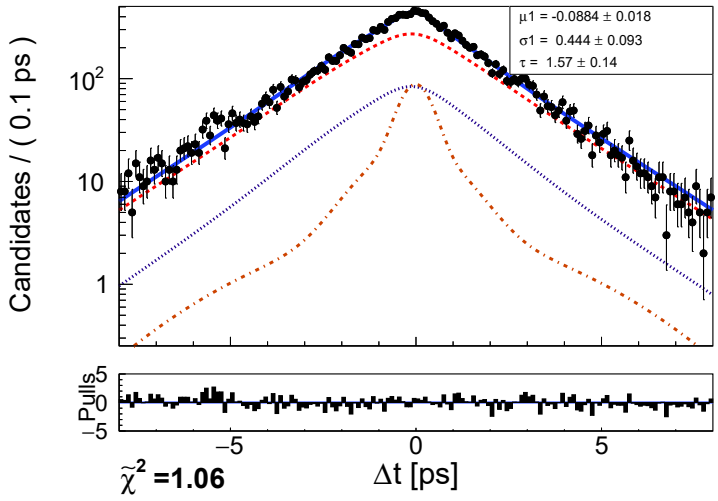


Figure 5.18: Fit to Δt distribution for all candidates in simulated data. The combined probability distribution function is represented by the solid blue line while the three components are represented by a dashed red for the signal, a dotted purple for the $b\bar{b}$ background and a dashed-dotted orange for the continuum background.

Parameter	Value used P_{all}	
$\mu 1_{cont}$	-0.007	fixed from MC sideband fit, Figure 5.12 (*right*)
$\sigma 1_{cont}$	0.401	fixed from MC sideband fit, Figure 5.12 (*right*)
dm_{cont}	-0.0846	fixed from MC sideband fit, Figure 5.12 (*right*)
$f1_{cont}$	0.468	fixed from MC sideband fit, Figure 5.12 (*right*)
$f2_{cont}$	0.357	fixed from MC sideband fit, Figure 5.12 (*right*)
$s2_{cont}$	2.88	fixed from MC sideband fit, Figure 5.12 (*right*)
$s3_{cont}$	3.02	fixed from MC sideband fit, Figure 5.12 (*right*)
$\mu 1_{res}$	-0.0884 ± 0.018	floating
$\sigma 1_{res}$	0.444 ± 0.093	floating
dm_{res}	-0.360	fixed from fit to Δt residuals from signal MC, Figure 5.15
$f1_{res}$	0.561	fixed from fit to Δt residuals from signal MC, Figure 5.15
$f2_{res}$	0.336	fixed from fit to Δt residuals from signal MC, Figure 5.15
$s2_{res}$	2.84	fixed from fit to Δt residuals from signal MC, Figure 5.15
$s3_{res}$	2.99	fixed from fit to Δt residuals from signal MC, Figure 5.15
τ_{eff}	1.31	fixed from fit to $b\bar{b}$ MC candidates, Figure 5.17
τ	1.57 ± 0.14	floating
n_{sgn}	12530	fixed from 2D fit on MC, Figure 5.8
$n_{b\bar{b}}$	3410	fixed from 2D fit on MC, Figure 5.8
n_{cont}	1430	fixed from 2D fit on MC, Figure 5.8

Table 5.11: Parameters used the final fit on MC in Figure 5.18, P_{cont} parameters are all fixed from the fit to the sideband events, P_{sgn} and $P_{b\bar{b}}$ share the same resolution where only μ_1 and σ_1 are floating.

5.5.3 Coutntinuum background Δt distribution from data sideband

As described in Section 5.5.1 the shape of the Continuum background Δt distribution in the final fit to extract the B^0 lifetime will be completely fixed. Its yield is fixed from the M_{bc}–ΔE fit of Section 5.4 while its shape is determined from a fit to a sideband in M_{bc}, ΔE, R_2 and $\cos\theta_{\text{thrust}}$. Figure 5.19 shows the result of this fit. The distribution is fitted with the sum of three Gaussian distributions with all the parameters fixed to the values obtained from the fit to the simulated candidates except a common mean and sigma to allow for data-MC differences. The parameters obtained from the fit to the data are compatible with the values from the fit to simulated candidates.

5.6 Unblinding

The unblinding with the whole sample of data as been performed. Its result can be seen in Figure 5.20 and Table 5.12. The measured lifetime is $\tau = 1.48 \pm 0.28$ which is compatible with the known value.

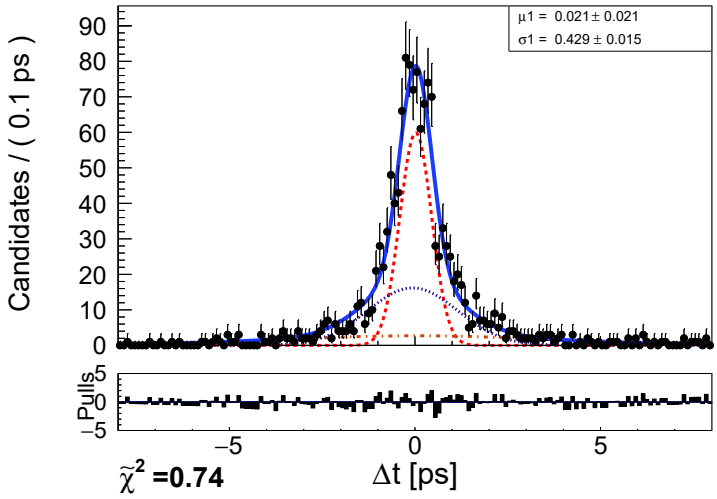


Figure 5.19: Fit to the Δt distribution of the sideband events in data.

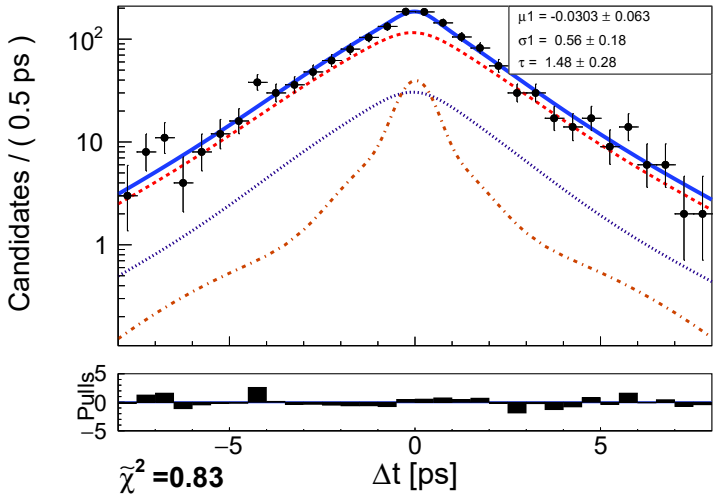


Figure 5.20: Fit to Δt distribution for all candidates in data. The combined probability distribution function is represented by the solid blue line while the three components are represented by a dashed red for the signal, a dotted purple for the $b\bar{b}$ background and a dashed-dotted orange for the continuum background.

Parameter	Value used P_{all}	
$\mu 1_{cont}$	0.021	fixed from data sideband fit, Figure 5.19
$\sigma 1_{cont}$	0.429	fixed from data sideband fit, Figure 5.19
dm_{cont}	-0.0846	fixed from MC sideband fit, Figure 5.12 (*right*)
$f1_{cont}$	0.468	fixed from MC sideband fit, Figure 5.12 (*right*)
$f2_{cont}$	0.357	fixed from MC sideband fit, Figure 5.12 (*right*)
$s2_{cont}$	2.88	fixed from MC sideband fit, Figure 5.12 (*right*)
$s3_{cont}$	3.02	fixed from MC sideband fit, Figure 5.12 (*right*)
$\mu 1_{res}$	-0.03 ± 0.06	floating
$\sigma 1_{res}$	0.56 ± 0.18	floating
dm_{res}	-0.360	fixed from fit to Δt residuals from signal MC, Figure 5.15
$f1_{res}$	0.561	fixed from fit to Δt residuals from signal MC, Figure 5.15
$f2_{res}$	0.336	fixed from fit to Δt residuals from signal MC, Figure 5.15
$s2_{res}$	2.84	fixed from fit to Δt residuals from signal MC, Figure 5.15
$s3_{res}$	2.99	fixed from fit to Δt residuals from signal MC, Figure 5.15
τ_{eff}	1.31	fixed from fit to $b\bar{b}$ MC candidates, Figure 5.17
τ	1.48 ± 0.28	floating
n_{sgn}	1120	fixed from 2D fit on data, Figure 5.9
$n_{b\bar{b}}$	271	fixed from 2D fit on data, Figure 5.9
n_{cont}	142	fixed from 2D fit on data, Figure 5.9

Table 5.12: Parameters used the final fit for data in Figure 5.20, P_{cont} parameters are all fixed from the fit to the sideband events, P_{sgn} and $P_{b\bar{b}}$ share the same resolution where only μ_1 and σ_1 are floating.

5.7 Systematic uncertainties and cross checks

The statistical uncertainty associated to this measurement is about 20% while the B^0 lifetime is known with a 0.3% uncertainty. Consequently, systematic studies only focused on the two main expected uncertainty sources: the parameterization of each time distribution contribution (partly fixed from simulated data) and the vertices reconstruction (embedding potential alignment and calibration effects).

5.7.1 Fit systematic uncertainty

Ten thousand toy datasets with a statistic equivalent to the one of the data sample have been obtained via the bootstrapping technique from a 100 fb^{-1} MC13 sample independent from the one used to develop the analysis. For each one of the samples we performed the strategy used on data: M_{bc}–ΔE fit, fit to the sideband to extract the shape of the continuum component and final fit to extract the B^0 lifetime. Figure 5.21 shows the difference with respect the true value of value of τ obtained with the procedure used on data obtained with a toy study and the corresponding pull distribution. A 3% bias is observed (-0.05 ps is the mean of the distribution of differences, blue bashed line in the figure). We assign as systematic uncertainty due to the fit procedure 0.05 ps. The central range containing 68.3% of the toys that corresponds to the fraction contained within 1 σ in

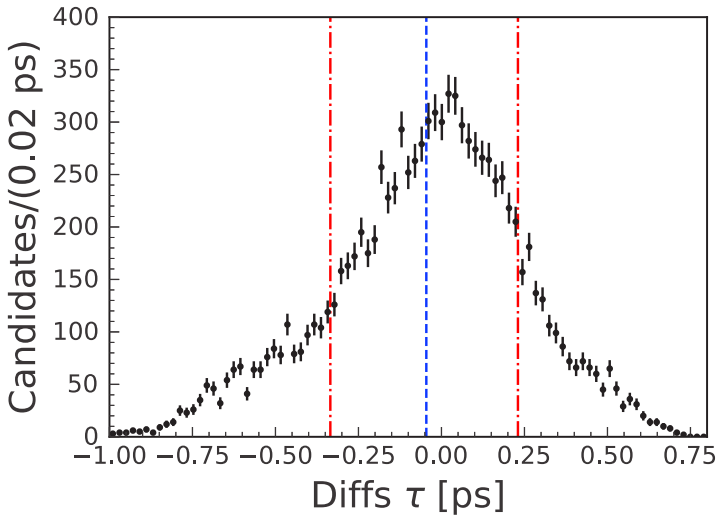


Figure 5.21: Distribution of the difference with respect the true value of value of τ obtained with the procedure used on data obtained with a toy study. The blue dashed line indicates the mean of the distribution while 68.3% of the toys are contained between the red dashed-dotted lines.

a Gaussian distribution (red dashed-dotted lines in the figure) has an half-width of 0.28 ps, the same value obtained as statistical error by the fit.

5.7.2 Systematic uncertainty for fixing τ_{eff} from simulation

The previous systematic uncertainty accounts for the bias in the fit strategy. It cannot however take into account the fit bias due data-MC differences as it is based on simulated samples. To take into account the data-MC difference some parameters of the resolution function and of the distribution for continuum events are obtained fitting the data. It is not possible however to determine the value of τ_{eff} in a data driven way. The B^0 lifetime fit is thus repeated leaving also τ_{eff} free (Figure 5.22). The difference with the lifetime obtained in the baseline fit is taken as systematic uncertainty. This amounts to 0.01 ps, which corresponds to a 0.7% relative systematic uncertainty.

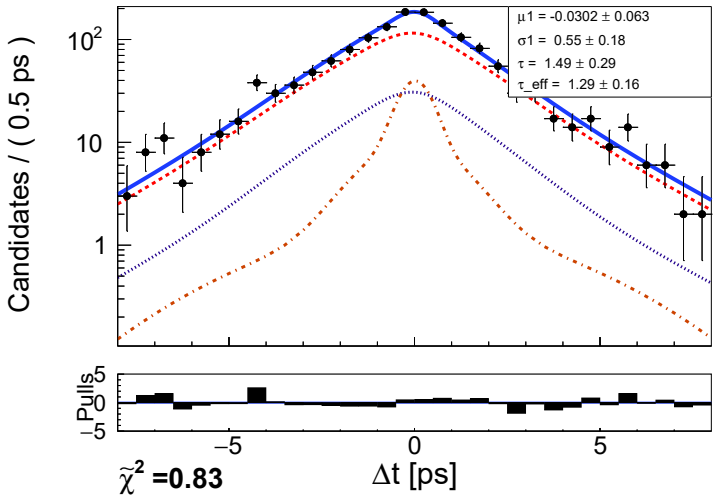


Figure 5.22: B^0 lifetime fit leaving τ_{eff} free.

5.7.3 Calibration and alignment systematic uncertainty

Another cross-check that can provide information on the systematic uncertainty due to the calibration and alignment quality is to extract the B^0 lifetime separately on three samples called in Belle II software as, `proc9+bucket7`, `proc10` and `bucket8` where `proc10` corresponds to the same dataset as `proc9+bucket7` but reconstructed with a better calibration and alignment. Figure 5.23 shows the difference of the SVD alignment constants used in this two data samples. Figure 5.24 and Table 5.13 contain the result of the same fit strategy used on data but applied on the different data samples. The fitted lifetime is compatible between the three samples which indicates that the possible systematic uncertainty is negligible with respect to the statistical uncertainty. A more precise estimate of the uncertainty linked to the calibration and alignment quality can be obtained by comparing the values from `proc9+bucket7` and `proc10` that correspond to the same dataset but with a different alignment and calibration. The difference of 0.03 ps would corresponds to a systematic uncertainty of 2%. We assign as systematic uncertainty due to the calibration and alignment 0.03 ps.

5.7.4 Total systematic uncertainty

The overall systematic uncertainty is obtained as a quadratic sum of the three contributions described above and amount to 0.06 ps or 4% relative uncertainty.

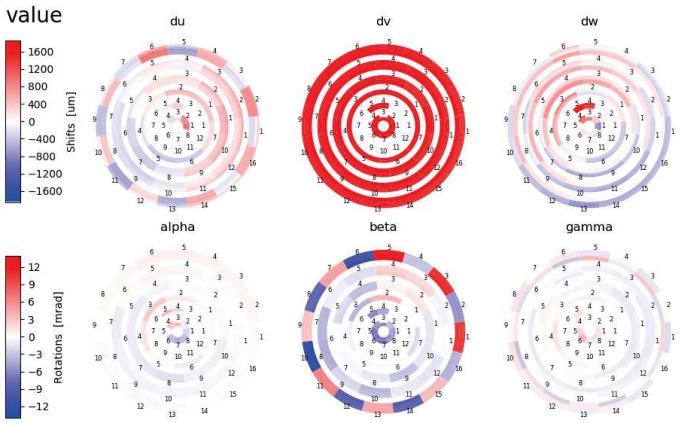


Figure 5.23: Difference of the SVD alignment constants between the alignment used in `proc10` and the one used in `proc9`.

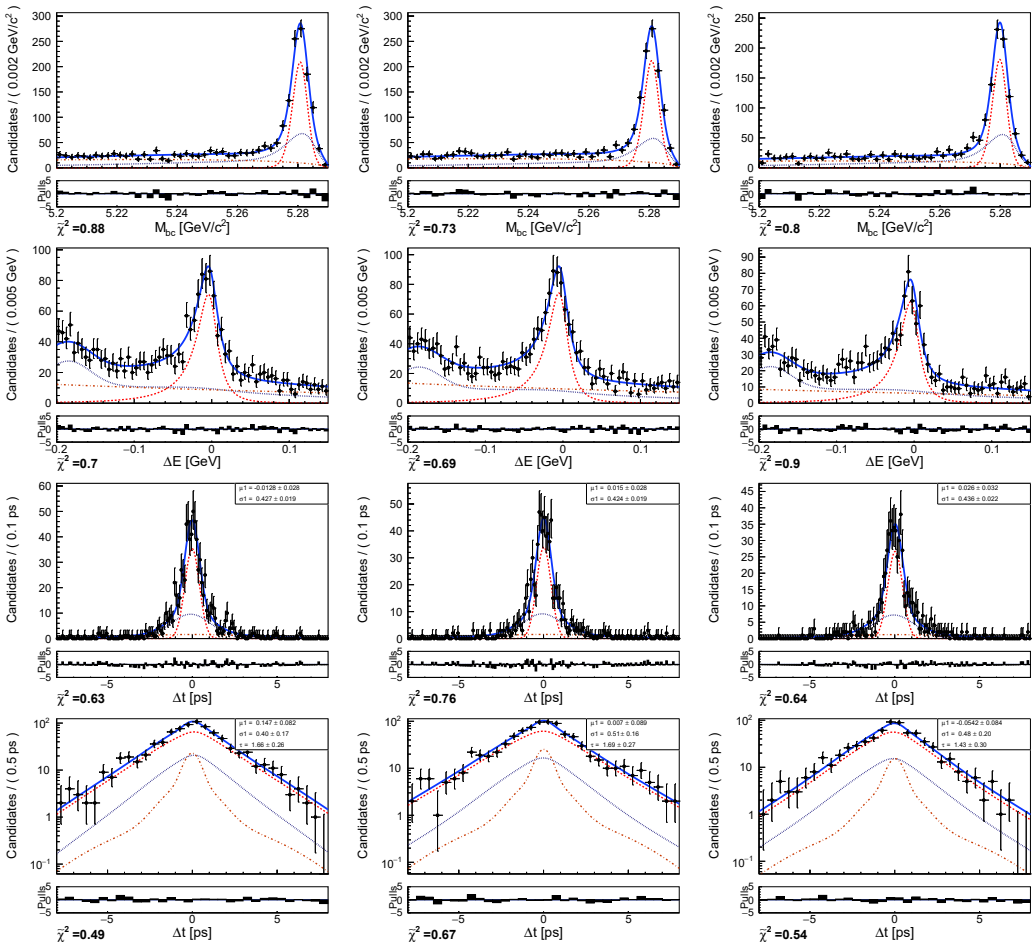


Figure 5.24: Comparison of the fit of (*respectively from the top*) M_{bc}, ΔE, the continuum shape from the sideband and the B^0 lifetime for (*left*) `proc9+bucket7`, (*middle*) `proc10` and (*right*) `bucket8`.

Fit parameter	value `proc9+bucket7`	value `proc10`	value `bucket8`
n_{sgn} fit region	661 ± 32	679 ± 31	555 ± 29
$n_{b\bar{b}}$ fit region	$(7.7 \pm 0.5) \times 10^2$	$(6.7 \pm 0.5) \times 10^2$	$(6.2 \pm 0.5) \times 10^2$
n_{cont} fit region	$(6.5 \pm 0.5) \times 10^2$	$(7.1 \pm 0.4) \times 10^2$	$(4.5 \pm 0.4) \times 10^2$
n_{sgn} signal region	596 ± 30	613 ± 29	503 ± 27
$n_{b\bar{b}}$ signal region	162 ± 25	141 ± 23	130 ± 22
n_{cont} signal region	79 ± 16	87 ± 16	55 ± 14
μ_{1cont} [ps]	-0.013 ± 0.028	0.015 ± 0.028	0.026 ± 0.032
σ_{1cont} [ps]	0.427 ± 0.019	0.424 ± 0.019	0.436 ± 0.022
μ_{1res} [ps]	0.15 ± 0.08	0.01 ± 0.09	-0.05 ± 0.08
σ_{1res} [ps]	0.40 ± 0.17	0.51 ± 0.16	0.48 ± 0.20
τ [ps]	1.66 ± 0.26	1.69 ± 0.27	1.43 ± 0.30

Table 5.13: Comparison fit values fitting data of different reprocessing; `proc10` corresponds to the same dataset as `proc9+bucket7` but reconstructed with a better calibration and alignment.

5.8 Conclusion

A first measurement of the B_d lifetime was performed with the 2019 Belle II data set, which amounts to an integrated luminosity of 8.7 ± 0.2 fb^{-1}. The estimated lifetime is $\tau_{B_d} = 1.48 \pm 0.28 \pm 0.06$ ps, where the first uncertainty is statistical and the second is systematic. This value is compatible with the world average of 1.519 ± 0.004 ps [23].
This analysis is a first step showing that the Belle II vertex detector delivers the expected performances and was publicly communicated outside Belle II [8]. Indeed, the resolution on the distance between the two B mesons is found o be 80 μm, approaching the expected 60 μm.

Conclusion

A first implementation of the measurement of the Time dependent CP violation parameters in radiative B^0 decays is done using Belle II simulated data. The technique is then applied to the simulated data equivalent to 1 ab^{-1} integrated luminosity collected at the $\Upsilon(4S)$ resonance from the SuperKEKB asymmetric e^+e^- collider. Two radiative decay channels are investigated $B^0 \to K^0_S\pi^+\pi^-\gamma$ and $B^0 \to K^0_S\pi^0\gamma$, to yield the following results:

$$\begin{array}{ll} \mathcal{S}_{B^0\to K^0_S\pi^+\pi^-\gamma} = -0.09 \pm 0.2 \pm 0.026 & \mathcal{S}_{B^0\to K^0_S\pi^0\gamma} = 0.02 \pm 0.3 \pm 0.02 \\ \mathcal{A}_{B^0\to K^0_S\pi^+\pi^-\gamma} = -0.21 \pm 0.17 \pm 0.025 & \mathcal{A}_{B^0\to K^0_S\pi^0\gamma} = 0.03 \pm 0.19 \pm 0.024 \end{array}$$

where the first uncertainty is statistical and the second is systematic. Our measurement results is compatible in precision with the Belle and Babar published results and using about the same integrated luminosity. A toy Monte Carlo study have been done using 200 toy experiments to extract the prospects of the statistical uncertainty with more data, as the Belle II program targets an integrated luminosity corresponding to $50\,\text{ab}^{-1}$. Figure 5.25 shows the calculated statistical uncertainty of the measured CP violation parameters $\mathcal{S}$ and $\mathcal{A}$ as function of the integrated luminosity for the $B^0 \to K^0_S\pi^0\gamma$ channel, the Belle and Babar statistical level is superimposed. Figure 5.26 similarly shows the statistical uncertainty for $B^0 \to K^0_S\pi^+\pi^-\gamma$ using also 200 toy Monte Carlo experiments. The figure reveals a promising result with the full Belle II dataset, where the expected statistical uncertainties for Belle II reach levels below the systematic one from Belle $\sim$ 0.05. However, such uncertainties cannot be directly converted into discovery potential for New Physics, since non CP eigenstates in this channel can dilute the precision on $\mathcal{S}$.
The next step regarding Time dependent CP violation in radiative B^0 decays will be the rediscovery of the two decay channels in the coming year (2021) with an integrated luminosity expecting to exceed 100 fb^{-1}.

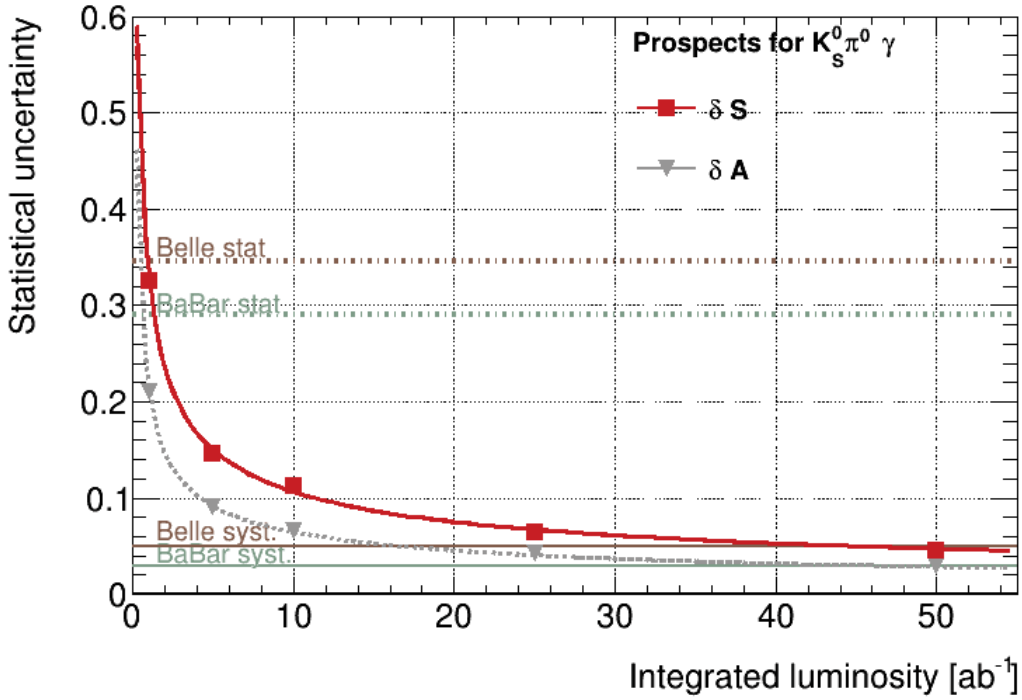


Figure 5.25: Prospects of $B^0 \to K^0_S\pi^0\gamma$ channel measured using 200 toy Monte Carlo experiments showing the statistical uncertainty of $\mathcal{S}$ and $\mathcal{A}$ parameters as function of the integrated luminosity planned for Belle II program. Belle and Babar statistical and systematical uncertainties from latest measurements for $B^0 \to K^0_S\pi^0\gamma$, $\mathcal{S}$ only parameter are also shown as dashed and full straight lines

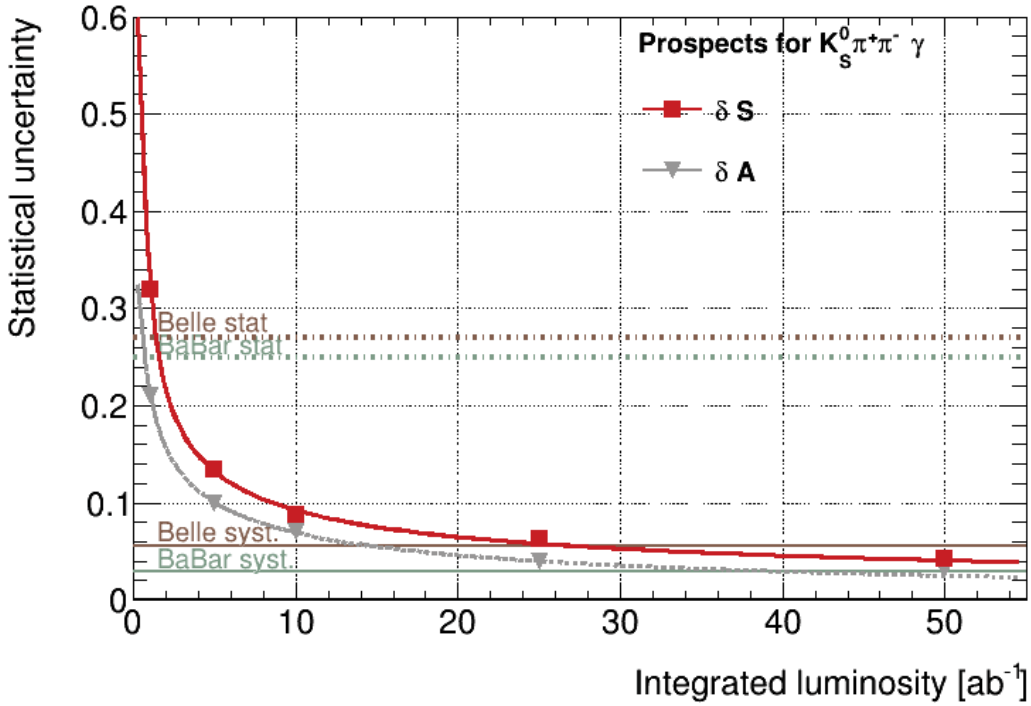


Figure 5.26: Prospects of $B^0 \to K^0_S\pi^+\pi^-\gamma$ channel measured using 200 toy Monte Carlo experiments showing the statistical uncertainty of $\mathcal{S}$ and $\mathcal{A}$ parameters as function of the integrated luminosity planned for Belle II program. Belle and Babar statistical and systematical uncertainties from latest measurements for $B^0 \to K^0_S\pi^+\pi^-\gamma$, $\mathcal{S}$ parameter only are also shown as dashed and full straight lines

As a complementary work to the TDCPV analysis and since data accumulated in 2019 was still not enough to run this analysis on real data. A demonstration of the vertexing performances has been studied, due its central importance for time-dependent analysis. A first measurement of the B^0 lifetime using hadronic decays is done on real data accumulated 2019 Belle II data set, which amounts to an integrated luminosity of 8.7 ± 0.2 fb^{-1}. The result of this measurement is:

$$\tau_{B_d} = 1.48 \pm 0.28 \pm 0.06 \text{ ps}$$

where the first uncertainty is statistical and the second is systematical. This value is compatible with the world average of 1.519 ± 0.004 ps [23]. Although the statistical uncertainty is quite large, the much smaller systematics demonstrates Belle II readiness for measurements with its vertex detector. One should note in addition, that this analysis uses a rather simple time resolution model to account for detector effects on the evaluation of decay time difference Δt beteen the two B mesons in the event. This strategy was chosen to reach a finalized measurement in a timely manner. Clearly more studies on Δt measurement and resolution parametrisation are needed and will benefit the statistical power of time dependent analysis. For example, a constraint on the vertex fit to the interaction point, which is very well known owing to the smallness of the beam size, bias the lifetime parameter measurement, since it shifts the Δz distribution. Already with the accumulated luminosity reached currently, a more complex resolution model reproducing the various reconstruction effects is needed and can be developped.

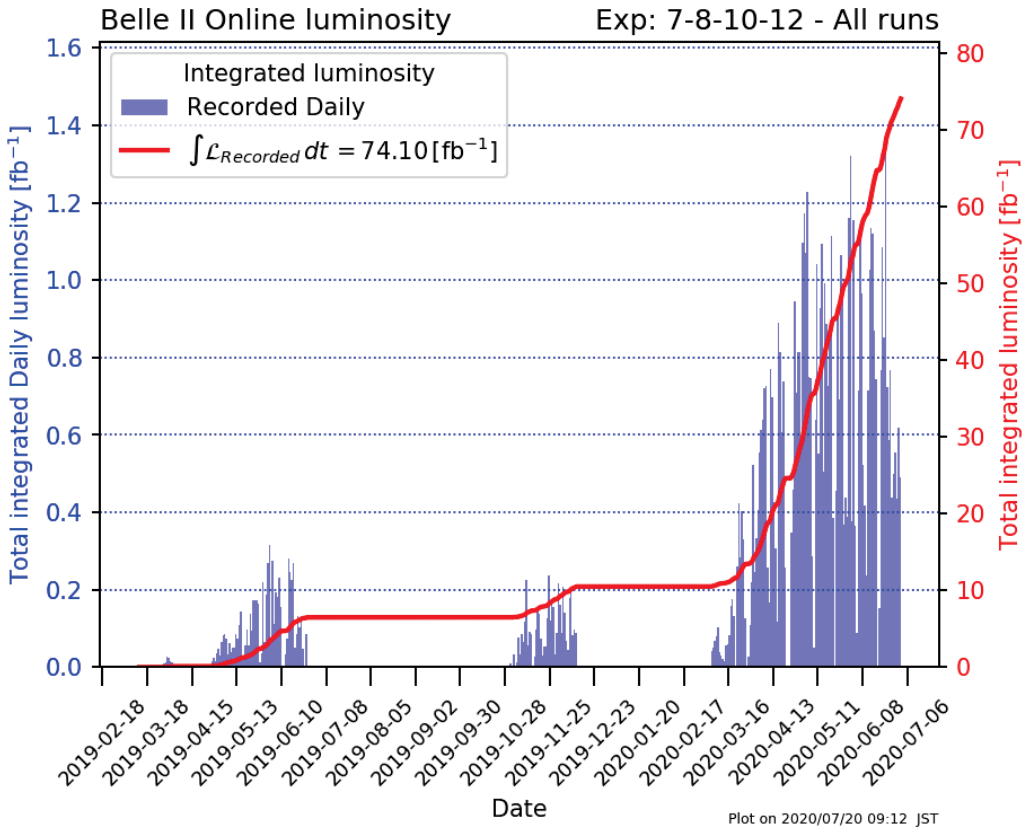


Figure 5.27: Total integrated daily luminosity and total integrated luminosity in fb^{-1} during Phase 3 2018-2020 data taking.

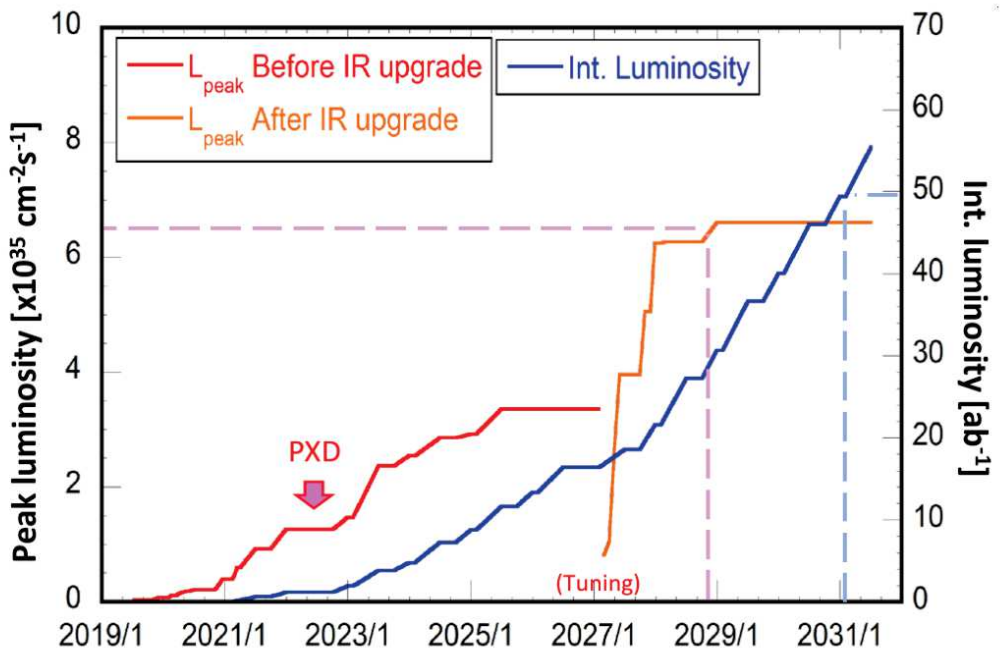


Figure 5.28: Mid and long term peak and integrated luminosity plan of Belle II project, IR (Interaction Region) need to be upgraded in 2026.

RÉSUMÉ français

Introduction

Pour mon doctorant, je travaille sur l'expérience Belle II, qui enregistre les phénomènes produits par les collisions e^+e^- de l'accélérateur SuperKEKB situé au Japon. Le but de cette expérience est d'observer des processus non décrits par le Modèle Standard de la physique des particules. De tels signes expérimentaux seraient une découverte d'une physique nouvelle et donneraient accès, au moins partiellement, à la théorie dont le Modèle Standard est une version effective.
L'un de ces nouveaux processus potentiel étudié dans notre groupe à l'IPHC, implique la restauration de la symétrie gauche-droite qui est rompue dans le modèle standard de la physique des particules et est également lié à l'asymétrie entre la matière et l'anti-matière observée dans notre univers.
Il existe deux types de violation de la symétrie *CP* (combinaison des opérations de conjugaison de charge *C* et de renversement des coordonnées d'espace ou parité *P*) : une violation directe et une violation indirecte. La violation directe de *CP* est observée lorsque la probabilité d'une désintégration et celle du processus conjugué par *CP* sont différentes, tandis que la violation indirecte se produit lorsque l'amplitude complexe de désintégration des particules et des anti-particules dans le même état final diffèrent. Dans mon travail de thèse, j'utilise une technique qui donne accès aux deux paramètres de la violation de *CP*, *S* pour la violation indirect et *C* pour la violation directe.

L'une des désintégrations intéressantes où la violation de *CP* serait un moyen de révéler l'existence de nouvelles particules est la désintégration radiative des méson B^0 qui se produit à travers des boucles quantiques, où des particules lourdes peuvent se propager. Le Modèle Standard, du fait de la structure vecteur-axial du couplage de l'interaction faible, prévoit que les photons émis dans ces désintégrations sont polarisés : principalement gauchers pour les mésons et droitiers pour les anti-mésons. L'état final étant différent pour les mésons et les anti-mésons, il ne peut y avoir de violation de *CP* indirecte. Certains modèles de

nouvelle physique introduisent des contributions de particules lourdes à ces désintégrations radiatives détruisant la polarisation différenciée entre méson et anti-méson de sorte que la violation indirecte peut se produire. Une telle observation représenterait à la fois une invalidation concrète du Modèle Standard et la découverte d'une nouvelle source de violation de *CP*.

Au sein du groupe strasbourgeois, je travaille sur la mesure des paramètres de violation de *CP* indirecte et directe S et C respectivement dans la transition radiative $b \to s\gamma$ qui se produit à travers des boucles quantiques. Nous étudions cette transition à travers deux états finals $B^0 \to K^0_s\pi^+\pi^-\gamma$ et $B^0 \to K^0_s\pi^0\gamma$. Les rapports d'embranch A first measurement of the B_d lifetime was performed with the 2019 Belle II data set, which amounts to an integrated luminosity of 8.7 ± 0.2 fb^{-1}. The estimated lifetime is $\tau_{B_d} = 1.48 \pm 0.28 \pm 0.06$ ps, where the first uncertainty is statistical and the second is systematic. This value is compatible with the world average of 1.519 ± 0.004 ps [23].
This analysis is a first step showing that the Belle II vertex detector delivers the expected performances and was publicly communicated outside Belle II [8]. Indeed, the resolution on the distance between the two B mesons is found o be 80 μm, approaching the expected 60 μm.ement de ces canaux sont relativement petits, respectivement de 7×10^{-6} et 9.5×10^{-6}. Les mesures existantes sur ces canaux ont été effectuées par les expériences *Belle* [4] [5] et *Babar* [6] [7] à partir d'une luminostié intégrée légèrement inférieure à 1 ab^{-1} et n'ont pas donné de résultats statistiquement significatifs pour la recherche de nouvelles physiques. Mon objectif était d'étudier la sensibilité de ces canaux pour obtenir une valeur non nulle de le paramètre $\mathcal{S}$ de violation indirecte du CP en utilisant TDCPV analyse avec l'ensemble de données Belle II.
Je commence à travailler avec des données issues de la simulation complète du détecteur pour paramétrer et affiner l'analyse des désintégrations radiatives des mésons B, qui consiste à sélectionner des événements potentiellement correspondant à notre canal puis effectuer un ajustement à quatre dimensions des données afin d'extraire le paramètres de violation de *CP*, $\mathcal{S}$ et $\mathcal{C}$. Pour finaliser l'analyse, j'ai évalué les incertitudes systématiques possibles de plusieurs sources pour les deux canaux. Ensuite, j'ai développé la première mesure de la durée de vie de B^0 avec des données réelles dans Belle II, la durée de vie de B^0 est précisément mesurée dans des expériences de physique des particules, la mesurer dans Belle II est une première démonstration des outils utilisés pour l'analyse TDCPV. La mesure de la durée de vie de B^0 a été documentée dans un article de la conférence Belle II, rapporté dans les conférences d'hiver 2020 et publié en mai 2020.

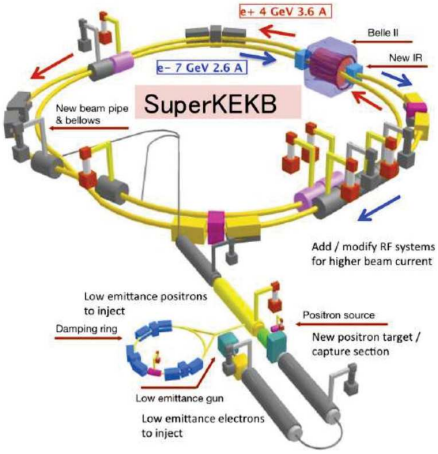


Figure 5.29: Une représentation schématique du l'accélérateur SuperKEKB

Projet de Belle II

L'accélérateur SuperKEKB fournit des collisions d'électrons de 7 GeV et de positron de 4 GeV pour obtenir une résonance de 10.57 GeV/c^2 d'énergie, nécessaire à la création d'un méson B et d'un anti-B. Figure 5.29 indique un aperçu schématique du collisionneur SuperKEKB. Le SuperKEKB vise une luminosité maximale de $8 \times 10^{35} cm^{-2} s^{-1}$ qui correspondent à une luminosité intégrée de 50 ab^{-1}, 40 fois plus grande que la luminosité produite à Belle.

La principale nouveauté de l'amélioration de la luminosité du SuperKEKB est le schéma de nano faisceau, dans lequel la fonction verticale β au "point d'interaction" IP appelé β_y^* est réduite à environ 0.3 mm (20 fois moins de le KEKB) et l'angle de croisement du faisceau ϕ_c a été augmenté d'un facteur de quatre environ par rapport à la KEKB. L'énergie asymétrique du faisceau, le $\Upsilon(4S)$, est produite avec une impulsion $\beta\gamma$, L'impulsion dépend de l'énergie des faisceaux et de l'angle de croisement entre eux. $\beta\gamma$ est nécessaire pour mesurer la différence de temps entre les désintégrations des deux mésons B^0 produits sur le site $\Upsilon(4S)$, puisque $\Delta t = \Delta z / \beta\gamma$. Grâce à la réduction de l'asymétrie de l'énergie du faisceau à SuperKEKB, $\beta\gamma$ est réduit d'un facteur 2/3 par rapport à KEKB. Ainsi, la distance moyenne Δt (Δz dans la direction de l'impulsion) d'environ 190 μm à la KEKB, est réduite à environ 130 μm à la SuperKEKB.

En raison de ces changements, le détecteur Belle II prendra des données à un accélérateur d'une luminosité 40 fois plus élevée, et doit donc être capable de fonctionner à des taux d'événements 40 fois plus élevés, avec des taux de fond plus élevés. Ainsi, afin d'améliorer les performances de Belle II, des modifications ont été apportées à la conception du détecteur. Le détecteur Belle II est conçu comme suit et comme présent dans la Figure 5.30: détecteurs de suivi qui consiste en, PXD (détecteur de pixel), SVD (détecteur de vertex de bande de silicium), CDC(chambre de dérive centrale). Les détecteurs d'identification des particules qui consiste en, TOP(comptage de propagation de temps) dan la région de la barrel et ARICH (Le compteur d'aérogels) détecteur. Calorimètre électromagnétique ECL, mesurer le dépôt d'énergie des photons neutres à l'aide de

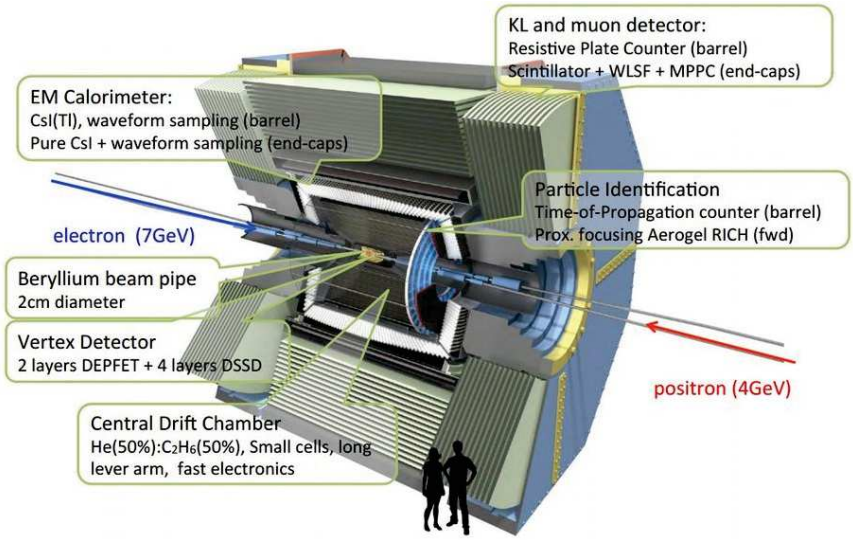


Figure 5.30: Une représentation schématique du détecteur Belle II

cristaux scintillants. Le détecteur de neutre kaon K_L^0 et muon μ KLM, la couche extérieure de Belle II détecteur. Enfin, Belle II en ligne trigger système qui fournissent des informations provenant de divers sous-détecteurs afin de filtrer le grand nombre de collisions intéressantes, et surtout pas la décroissance du méson B. Le système est composé d'un trigger matériel et d'un trigger logiciel. La décision de conserver l'événement est prise à l'aide du HLT, le trigger logiciel.

La mise en service de l'accélérateur SuperKEKB a été réalisée, en phase 1, les anneaux d'accélération ont été mis en service sans le système de focalisation finale au point d'interaction sans le détecteur Belle II. Au cours de la phase 2, la mise au point finale et l'anneau amortisseur de positrons sont en place, ainsi que le détecteur Belle II, à l'exception du détecteur de vertex où, à la place, le détecteur BEAST a été installé pour mettre en service la machine en mesurant les taux de fond du faisceau et assurer la sécurité radiologique de Belle II pour fonctionner à une luminosité plus élevée. Dans la phase 3, le détecteur de vertex complet a été installé et a commencé à prendre des données en mars 2019, le plan est d'atteindre une luminosité élevée de 50 ab^{-1}, permettra d'avoir un ensemble de données pour avoir une précision sur l'analyse TDCPV.

Sensibilité de l'analyse TDCPV
Dans cette section, les principaux principes utilisés pour effectuer l'analyse CP en fonction du temps sont énumérés. Belle II fournit des collisions électron-positon, à une résonance de 10.58 GeV se désintègre en une paire de BB et cette paire est au repos dans le $\Upsilon(4S)$ centre de masse système. Cette paire est produite dans un état cohérent quantique, ce qui signifie que lorsque le méson B subit un mélange de saveurs et un méson change de saveur, l'autre change automatiquement de saveur aussi. Ce fait permet la technique dite "flavour tagging". Dans cette analyse, nous notons B^0_{tag} qui est identifié expérimentalement par reconstruction inclusive et par entaglement quantique, l'autre saveur B^0_{sig} est connue à t_{tag}. Ensuite, comme B^0_{sig} se décompose en deux désintégrations radiatives, la différence de temps Δt peut être mesurée à partir de Δz, la distance entre les sommets de désintégration de B^0_{tag} et B^0_{sig}. Enfin, les paramètres TDCPV sont extraits de la distribution Δt.

Marquage des saveurs est nécessaire à l'analyse TDCPV, la tâche est de déterminer le flavor de B^0_{tag} au moment de son disintegration. B^0 mesons fourni des signatures de saveurs par des états finaux saveurs spécifiques. Après avoir connu la saveur des deux mésons B^0, et afin d'obtenir des $\mathcal{S}$ et $\mathcal{A}$ corrects, les effets expérimentaux doivent être pris et la fonction de densité de probabilité obtenue à partir des taux de décroissance est utilisée pour ajuster la distribution temporelle comme suit:

$$\begin{aligned}\mathcal{P}(\Delta t, q) = f_{sig}\frac{e^{-|\Delta t|/\tau_{B^0}}}{4\tau_{B^0}}[1 - q\Delta w + (1-2w)q\mathcal{A}\cos(\Delta M\Delta t) + \\ \mathcal{S}\sin(\Delta M\Delta t)] \otimes \mathcal{R}_{sig}(\Delta t) - (1 - f_{sig})\mathcal{P}_{bkg}(\Delta t)\end{aligned} \tag{5.7}$$

$\mathcal{P}_{bkg}(\Delta t)$ est la PDF decrivant la Δt distribution des candidats de fond, et $\mathcal{R}_{sig}(\Delta t)$ Δt fonction de résolution pour les candidats de signal. Afin d'obtenir des valeurs non biaisées des paramètres CP, il est important de bien comprendre et d'estimer f_{sig}, w, Δw, $\mathcal{R}_{sig}$, et $\mathcal{P}_{bkg}$. Ensuite, nous construisons une fonction de vraisemblance et nous la maximisons pour obtenir les meilleures estimations pour $\mathcal{A}$ et $\mathcal{S}$.
A fin d'extraire $\mathcal{S}$ et $\mathcal{A}$, plusieurs étapes doivent être réalisées la sélection des événements, PremièrE, pour chaque événement l'évaluation des temp de désintégrations et de la nature méson ou anti-méson de la désintégration, ensuite une inférence statistique des paramètres de CP sur l'ensemble des événements sélectionnés et enfin l'évaluation de l'incertitude associée aux effets systématiques sur la mesure.

Mon travail dans l'analyse TDCPV s'est principalement porté sur la première (sélection) et la dernière étape (systématique), les autres étant prises en charge par un post-doctorant du groupe.

Optimisation de la sélection :
Avec le détecteur Belle II, nous mesurons l'ensemble des caractéristiques des

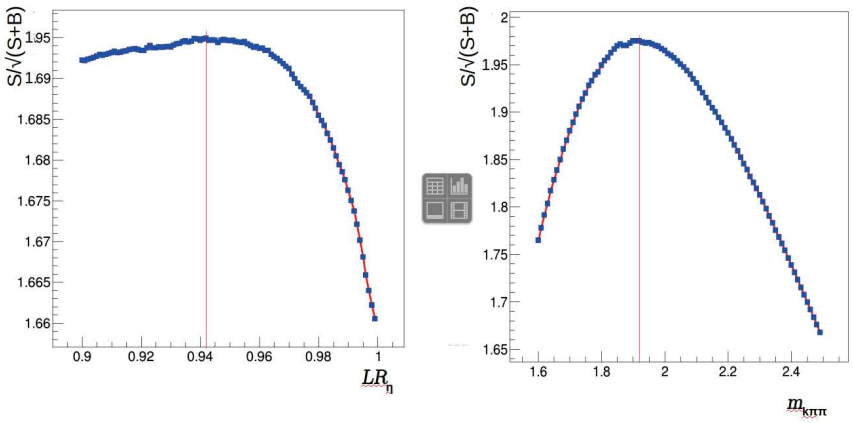


Figure 5.31: Les distributions de le $\frac{S}{\sqrt{S+B}}$en fonction des variables

particules produites par la collision. Nous pouvons alors les combiner pour construire une dizaine de grandeurs, qui présentent des distributions spécifiques en fonction de la cinématique des canaux de désintégration ($B0 \to (K^0_s\pi^+\pi^-\ \gamma$, $K^0_s\pi^0\ \gamma)$) et qui les distinguent du reste des autres états finals possibles. Pour sélectionner les canaux d'intérêt, nous appliquons des coupes dans ces distributions. Ces coupures sont choisies en fonction d'une stratégie spécifique appelée optimisation, qui maximise la signifiance du signal, définie par $\frac{N_S}{\sqrt{N_S+N_B}}$ (N_S: candidats de signal, N_B: candidats de bruit de fond) [7]. Après avoir fait l'optimisation complète, j'ai atteint une signifiance maximale de ~ 6. Figure 5.31 indique la première étape utilisée pour obtenir une signification maximale.

Systematics study: Différentes incertitudes systématiques contribuent à la mesure des paramètres quantifiant la violation de *CP*, S et C. La contribution dominante est liée à la procédure d'ajustement des distributions temportelles. En effet, de nombreux paramètres sont utilisés dans la modélisation de ces distributions et, lors de l'ajustement final des données, ces paramètres sont fixés à partir des données simulées. J'ai développé une procédure d'évaluation de l'incertitude induite sur les valeurs S et C par l'incertitude sur les paramètres fixés de l'ajustement.
La méthode consiste à faire varier individuellement tous ces paramètres dans un intervalle fixé par l'incertitude sur leur estimation, puis à refaire l'ajustement global. La distribution des valeurs de S et C trouvées permet alors de quantifier l'incertitude systématique de l'ordre de $\Delta S_{sys} = 0.02$ pour S par exemple. Ces effets systématiques sont beaucoup plus faibles que l'incertitude statistique, qui elle atteint $\Delta S_{stat} = 0.2$.

Conclusion de l'analyse TDCPV: Une comparaison est faite avec les incertitudes statistiques réalisées par Belle. Le tableau 5.14, rapporte les incertitudes statistiques obtenues dans cette analyse en utilisant les données simulées de Belle II de $1\,\text{ab}^{-1}$ et les incertitudes obtenues de la dernière analyse de Belle

$\mathcal{S}$ **parameter**	$\mathcal{S}_{B^0 \to K^0_S \pi^0 \gamma}$	$\mathcal{S}_{B^0 \to K^0_S \pi^+ \pi^- \gamma}$
Belle II statistical uncertainty using 1 ab^{-1}	0.30	0.219
Belle statistical uncertainty	0.31	0.27
Expected uncertainty with Belle II 50 ab^{-1}	0.04	0.03
Belle II systematic uncertainty using 1 ab^{-1}	0.02	0.027
Belle systematic uncertainty	0.07	+0.04 /-0.07

Table 5.14: Comparaison de l'incertitude statistique des paramètres entre l'analyse actuelle de Belle II sur les données simulées et les derniers résultats de Belle sur les deux canaux $B^0 \to K^0_S \pi^+ \pi^- \gamma$ et $B^0 \to K^0_S \pi^0 \gamma$, plus les attentes avec l'ensemble complet des données prévues de Belle II de 50 ab^{-1}.

pour les mêmes canaux. Les résultats de Belle II sont similaires ou légèrement meilleurs que celles de Belle. C'est une découverte importante, qui démontre que le nouveau détecteur de vertex Belle II a la capacité, dans la simulation, de surmonter la pénalité de la faible poussée disponible dans SuperKEKB par rapport à celle qui prévaut à KEKB-Belle. Le prochain chapitre explorera l'état actuel du vertex dans Belle II avec une mesure sur des données réelles. En ce qui concerne les attentes relatives à l'ensemble des données de Belle II, soit 50 ab^{-1}, il semble que la mesure sera encore statistiquement limitée. Bien entendu, il s'agit d'une enquête préliminaire sur les performances de l'expérience Belle II. Des outils d'analyse plus avancés sont déjà développés et ils augmenteront naturellement la puissance statistique des mesures TDCPV.

Mesure du temps de vie des mésons B^0 avec les premières données

Dans ce chapitre, une nouvelle analyse complète est présentée, la mesure de la durée de vie B^0. Comme déjà révélé dans le chapitre 4, dans la mesure TDCPV, le vertex est la clé pour augmenter la sensibilité à l'analyse temporelle. Pour démontrer la capacité de vertexing dans Belle II, une analyse qui mesure la mesure de la durée de vie B^0, τ en utilisant la différence de temps mesurée entre les deux paires B^0 et $\overline{B}^0$ sera un outil pour vérifier les outils d'ajustement des vertex et la modélisation de la résolution temporelle. Cette mesure est effectuée en utilisant l'ensemble de données de la phase 3 précoce et les désintégrations hadroniques du méson B. Nous suivons une procédure d'analyse standard qui présente des similitudes avec l'analyse TDCPV. Comme pour l'analyse TDCPV, le candidat méson B est entièrement reconstruit mais avec des états finaux de désintégration hadronique [42].

La technique du reste de l'événement permet de reconstruire la position du

sommet de l'autre méson B, toujours appelé *tag side* même s'il n'est pas utilisé pour le marquage comme c'est le cas dans l'analyse TDCPV. La méthode d'estimation de la fraction du signal est similaire à celle utilisée dans l'analyse TDCPV, en utilisant un ajustement 2D aux distributions M_{bc} et ΔE. Le paramètre de durée de vie τ est mesuré en utilisant un ajustement à une dimension de la distribution du temps. Chacune des trois distributions du temps, pour le signal, le continuum et le fond $b\bar{b}$, est modélisée. Une fonction commune a également été développée pour le modèle de résolution temporelle, en ajustant les paramètres spécifiquement pour chaque contribution. La forme fonctionnelle du modèle de résolution est définie pour être simple car il s'agit de la première modélisation au démarrage de l'analyse de Belle II.

Toute mesure officiel de la collaboration Belle II suit une procédure | "à l'aveugle". C'est à dire que la méthode est mise au point entièrement sur des données simulées, puis après validation d'un comité de revue, elle est appliquée au données réelles.

Méthode de l'extraction la durée de vie B^0 Pour mesurer la durée de vie B^0 des candidats sélectionnés, un ajustement de probabilité non binné est effectué sur la distribution globale Δt. La distribution des probabilités dans l'équation (5.8) décrit cette distribution globale en combinant les rendements de contribution mesurés dans la section 5.4.

$$\mathrm{P}_{all}(\Delta t) = n_{sgn}\mathrm{P}_{sgn}(\Delta t) + n_{b\bar{b}}\mathrm{P}_{b\bar{b}}(\Delta t) + n_{cont}\mathrm{P}_{cont}(\Delta t). \tag{5.8}$$

Les modèles analytiques de distribution de Δt pour les trois principales contributions à l'échantillon candidat sont décrits dans la section 5.5.1.

Un élément important de l'ajustement pour extraire la durée de vie B est la résolution fonction $\mathcal{R}$ qui décrit le frottement introduit par divers effets au cours de la reconstruction. Dans cette analyse, $\mathcal{R}$ est modélisé par la somme de trois distributions gaussiennes(5.9).

$$\begin{aligned}\mathcal{R}(\delta_{\Delta t}) = f_1\mathcal{G}(\delta_{\Delta t};\mu_1,\sigma_1) + f_2\mathcal{G}(\delta_{\Delta t};\mu_1+dm,s_2\times\sigma_1)\\ +(1-f_1-f_2)\mathcal{G}(\delta_{\Delta t};\mu_1,s_2\times s_3\times\sigma_1)\end{aligned} \tag{5.9}$$

Une fonction de résolution universelle est utilisée et non fonction candidat par candidat fonction, en fonction par exemple de l'incertitude sur Δt due à la petite taille de l'échantillon considéré dans cette analyse.Cette résolution est également utilisée pour ajuster la fonction Δz des deux côtés, signal et tag. Figure 5.32 montre ces ajustements. L'ajustement pour obtenir la durée de vie est également indiquée dans la figure 5.20.

Une première mesure de la durée de vie du B_d a été réalisée avec l'ensemble des données de 2019 Belle II, ce qui correspond à une luminosité intégrée de

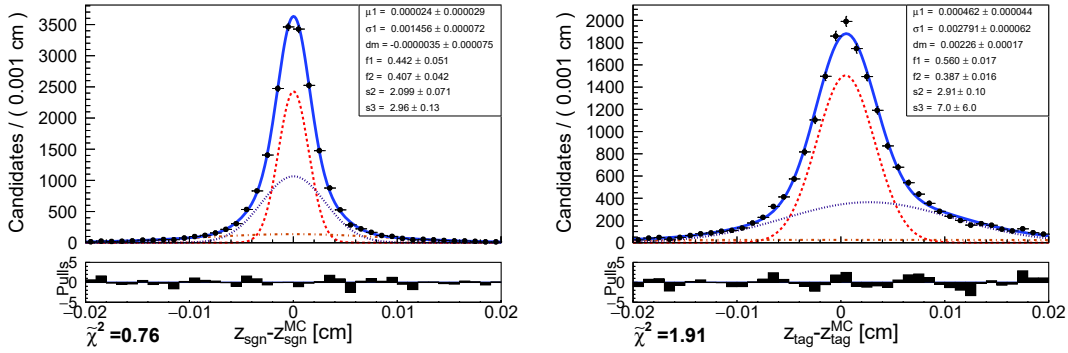


Figure 5.32: Fit to the z vertex residual for (*left*) the signal B and (*right*) the tag B.

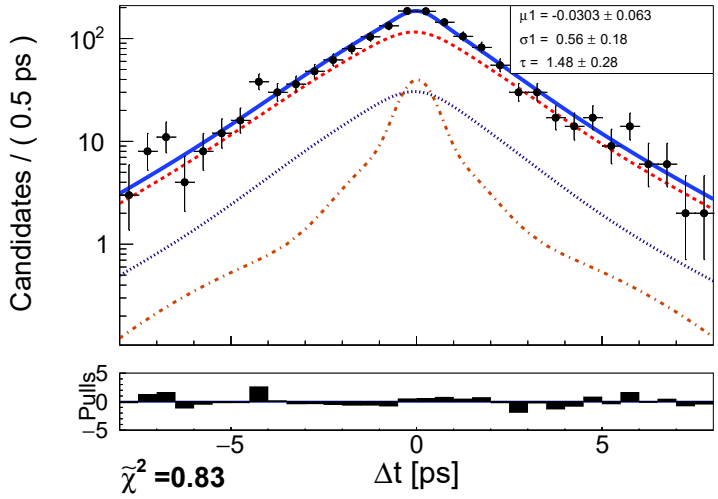


Figure 5.33: Fit to Δt distribution for all candidates in data. The combined probability distribution function is represented by the solid blue line while the three components are represented by a dashed red for the signal, a dotted purple for the $b\bar{b}$ background and a dashed-dotted orange for the continuum background.

8.7 ± 0.2 fb^{-1}. La durée de vie estimée est $\tau_{B_d} = 1.48 \pm 0.28 \pm 0.06$ ps, où la première incertitude est statistique et la seconde est systématique. Cette valeur est compatible avec la moyenne mondiale de 1.519 ± 0.004 ps [23].

Cette analyse est une première étape montrant que le vertex détecteur de Belle II fournit les performances attendues et a été publiquement communiqué en dehors de Belle II [8]. En effet, la résolution sur la distance entre les deux mésons B se trouve être de 80 μm, approchant les 60 μm attendus.

Conclusion

La mesure de la violation de la symétrie CP est l'un des programmes principaux et prometteurs du projet Belle II visant à découvrir la nouvelle physique. Durant ma thèse, j'ai quantifié avec des données simulées la précision atteignable avec une analyse TDCVP des désintégrations radiatives des mésons B^0. Cette analyse donne les résultats suivants :

$$\mathcal{S}_{B^0\to K^0_S\pi^+\pi^-\gamma} = -0.09 \pm 0.2 \pm 0.026 \qquad \mathcal{S}_{B^0\to K^0_S\pi^0\gamma} = 0.02 \pm 0.3 \pm 0.02$$
$$\mathcal{A}_{B^0\to K^0_S\pi^+\pi^-\gamma} = -0.21 \pm 0.17 \pm 0.025 \qquad \mathcal{A}_{B^0\to K^0_S\pi^0\gamma} = 0.03 \pm 0.19 \pm 0.024$$

la première incertitude est statistique et la seconde est systématique. Nos résultats de mesure sont compatibles en termes de précision avec les résultats publiés par Belle et Babar et utilisent la même luminosité intégrée. La prochaine étape concernant la violation du Time dependent CP dans les décroissances radiatives B^0 sera la redécouverte des deux canaux dans l'année à venir (2021) avec une luminosité intégrée qui devrait dépasser 100 fb^{-1}. Par ailleurs, étant donné que les données de Belle II accumulées en 2019 n'étaient pas suffisantes pour démarrer cette analyse TDCVP, j'ai développé une autre analyse complète en utilisant les désintégrations du méson hadronique B pour mesurer la durée de vie pour la première fois dans Belle II. Cette mesure est un premier pas nécessaire pour mettre en place des mesures de type TDCPV.

Une première mesure de la durée de vie de B^0 utilisant des désintégrations hadroniques est effectuée sur des données réelles accumulées 2019 Belle II, équivaut à une luminosité intégrée de $8,7 \pm 0,2$ fb^{-1}. Le résultat est :

$$\tau_{B_d} = 1.48 \pm 0.28 \pm 0.06 \text{ ps}$$

la première incertitude est statistique et la seconde est systématique. Cette valeur est compatible avec la moyenne mondiale de 1.519 ± 0.004 ps [23]. Bien que l'incertitude statistique soit assez grande, la systématique beaucoup plus petite démontre que Belle II est prête pour des mesures avec son détecteur de vertex.

Probability density functions

In this section, I give the definitions of the PDFs used in the fits

.1 Gaussian function

The expression for the standard Gaussian function is defined as:

$$G(x,\mu,\sigma) = \frac{1}{a}\exp\left[\frac{1}{2}\left(\frac{x-\mu}{\sigma}\right)^2\right]$$

The parameters μ and σ are the mean and the width of the Gaussian; $\frac{1}{a}$ is a normalization constant.

.2 Crystal Ball function

The expression for the standard Crystal Ball function is given as:

$$CB(x,\mu,\sigma,\alpha,) \propto \left\{ \begin{array}{ll} (\frac{n}{\alpha})^n \frac{\exp(-\alpha^2/2)}{((\mu-x)/\sigma+n/\alpha-\alpha)^n} & x \leq \mu-\alpha\sigma \\ \\ exp\left[\frac{1}{2}(\frac{x-\mu}{\sigma})^2\right] & x > \mu-\alpha\sigma \end{array} \right\}$$

The parameters μ and σ describes a Gaussian, which is truncated on the low side at $\mu - \alpha\sigma$ and joined continuously to a power function with an exponent n, $\frac{1}{a}$ is a normalization constant.

.3 Argus function

The Argus function is given by:

$$Argus(x,x_0,\chi) = \frac{1}{a}t\cdot\sqrt{1-t^2}\cdot\exp[-\chi(1-t^2)] \quad \text{with} \quad t = \frac{x}{x_0}.$$

The parameter χ is the Argus shape parameter, the cutoff x_0 is the nominal beam energy, and $\frac{1}{a}$ normalization constant.

.4 Chebychev function

$$Chebychev(x) = \frac{1}{a}(1 + c_1 x)$$

$\frac{1}{a}$ normalization constant.

Plots fit to get signal and background fractions for channels

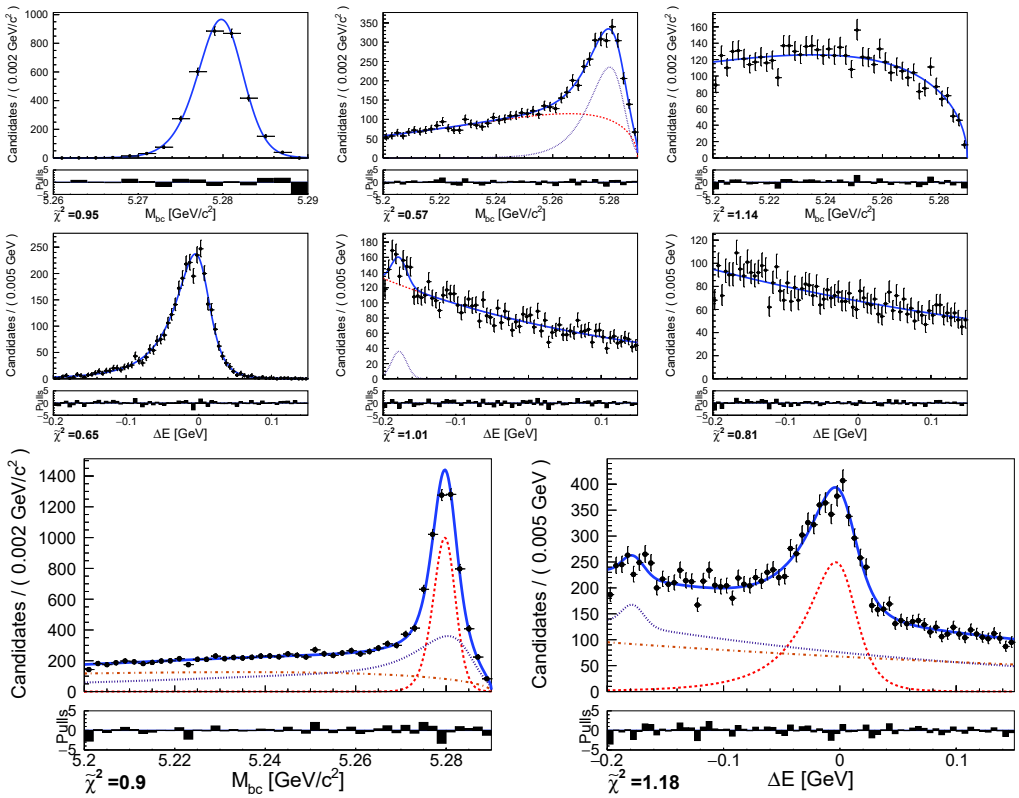


Figure 34: Fits projection for $B_d \to D^- \rho^+$. The first two rows show the projections in (*top*) M_{bc} and (*middle*) ΔE of the fits to the individual populations (*left*) signal, (*center*) $b\bar{b}$ background and (*right*) continuum background. The last row shows the projections in (*left*) M_{bc} and (*right*) ΔE of fit to extract the yields of the individual components.

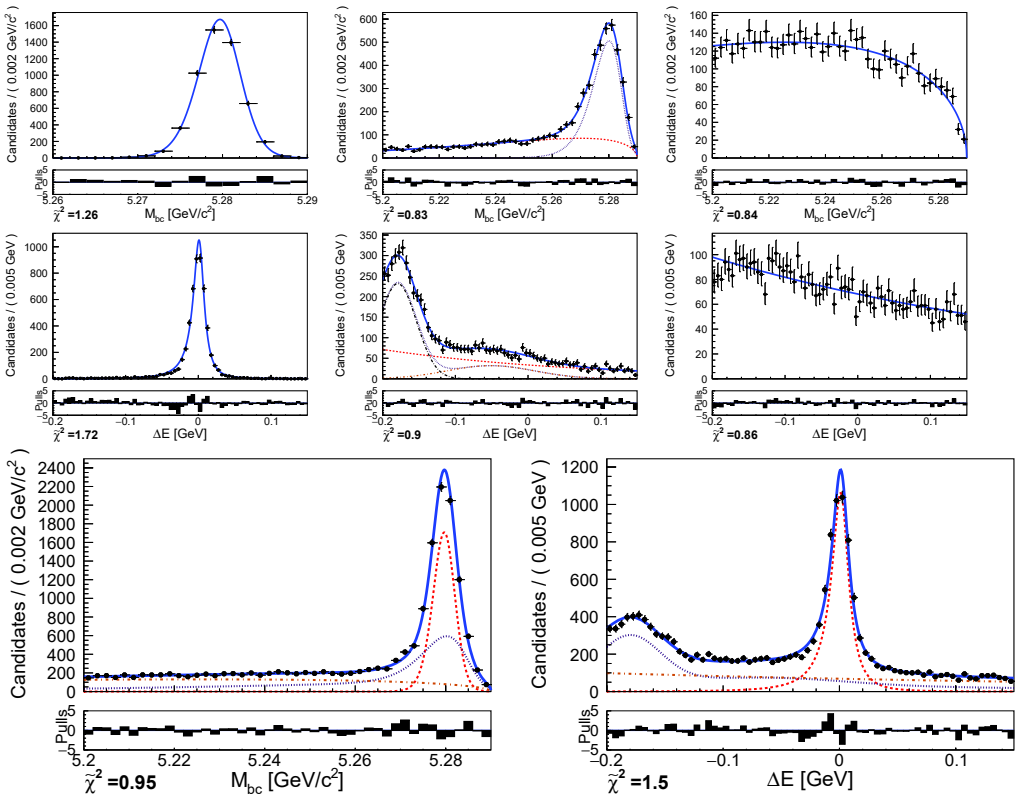


Figure 35: Fits projection for $B_d \to D^- \pi^+$. The first two rows show the projections in (*top*) M_{bc} and (*middle*) ΔE of the fits to the individual populations (*left*) signal, (*center*) $b\bar{b}$ background and (*right*) continuum background. The last row shows the projections in (*left*) M_{bc} and (*right*) ΔE of fit to extract the yields of the individual components.

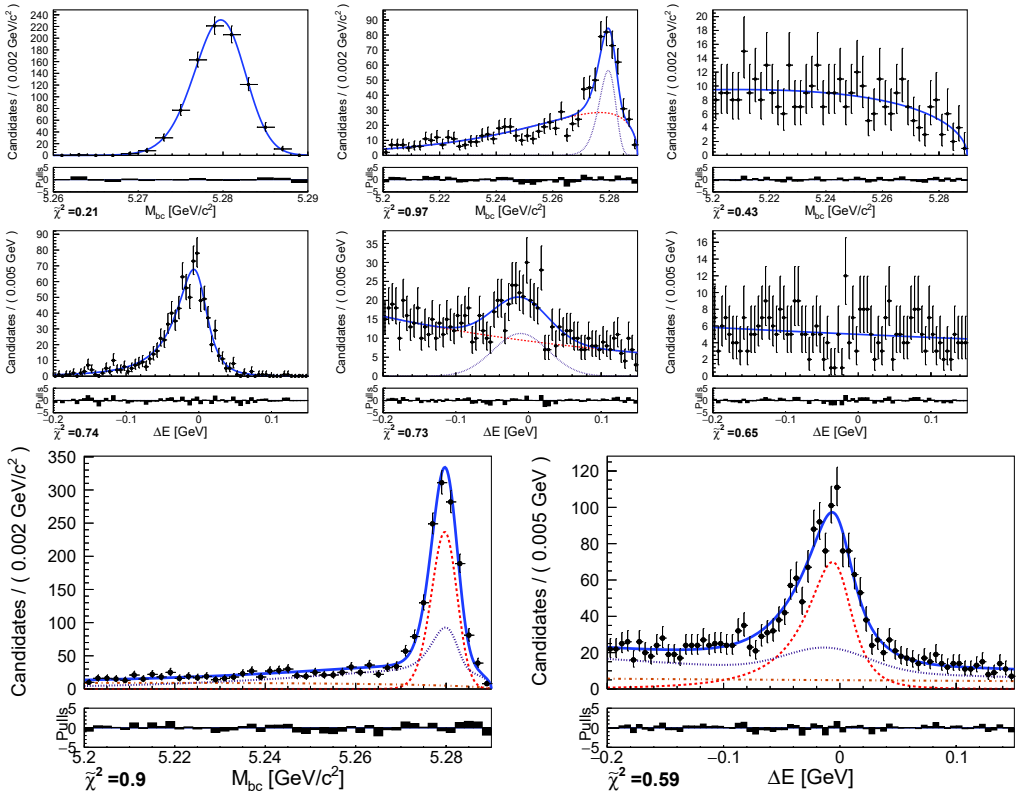


Figure 36: Fits projection for $B_d \to D^{*-}\rho^+$ ($D^0 \to K^-\pi^+$). The first two rows show the projections in (*top*) M_{bc} and (*middle*) ΔE of the fits to the individual populations (*left*) signal, (*center*) $b\bar{b}$ background and (*right*) continuum background. The last row shows the projections in (*left*) M_{bc} and (*right*) ΔE of fit to extract the yields of the individual components.

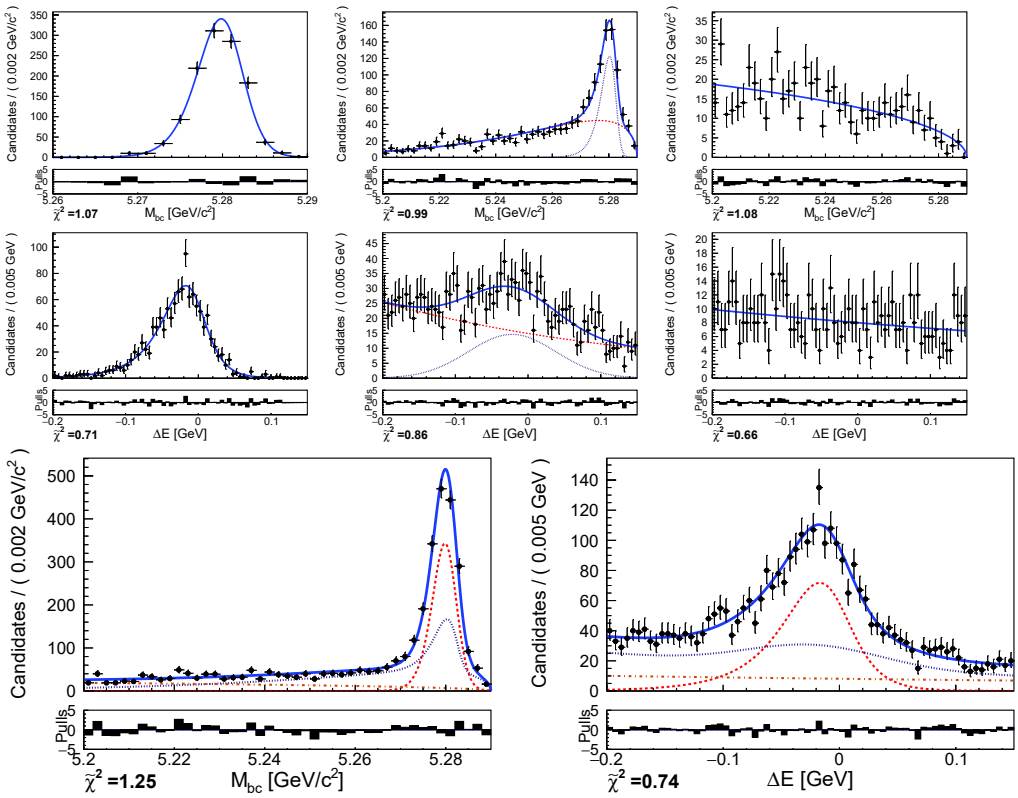


Figure 37: Fits projection for $B_d \to D^{*-}\rho^+$ ($D^0 \to K^-\pi^+\pi^0$). The first two rows show the projections in (*top*) M_{bc} and (*middle*) ΔE of the fits to the individual populations (*left*) signal, (*center*) $b\bar{b}$ background and (*right*) continuum background. The last row shows the projections in (*left*) M_{bc} and (*right*) ΔE of fit to extract the yields of the individual components.

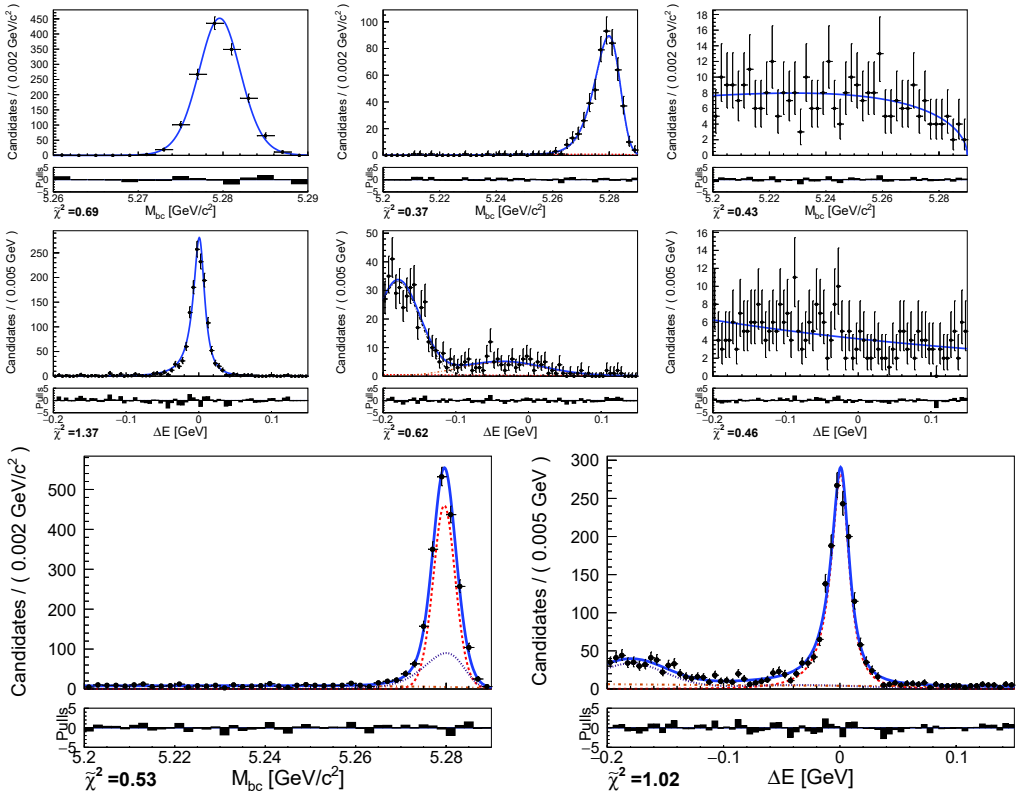


Figure 38: Fits projection for $B_d \to D^{*-}\pi^+$ ($D^0 \to K^-\pi^+$). The first two rows show the projections in (*top*) M_{bc} and (*middle*) ΔE of the fits to the individual populations (*left*) signal, (*center*) $b\bar{b}$ background and (*right*) continuum background. The last row shows the projections in (*left*) M_{bc} and (*right*) ΔE of fit to extract the yields of the individual components.

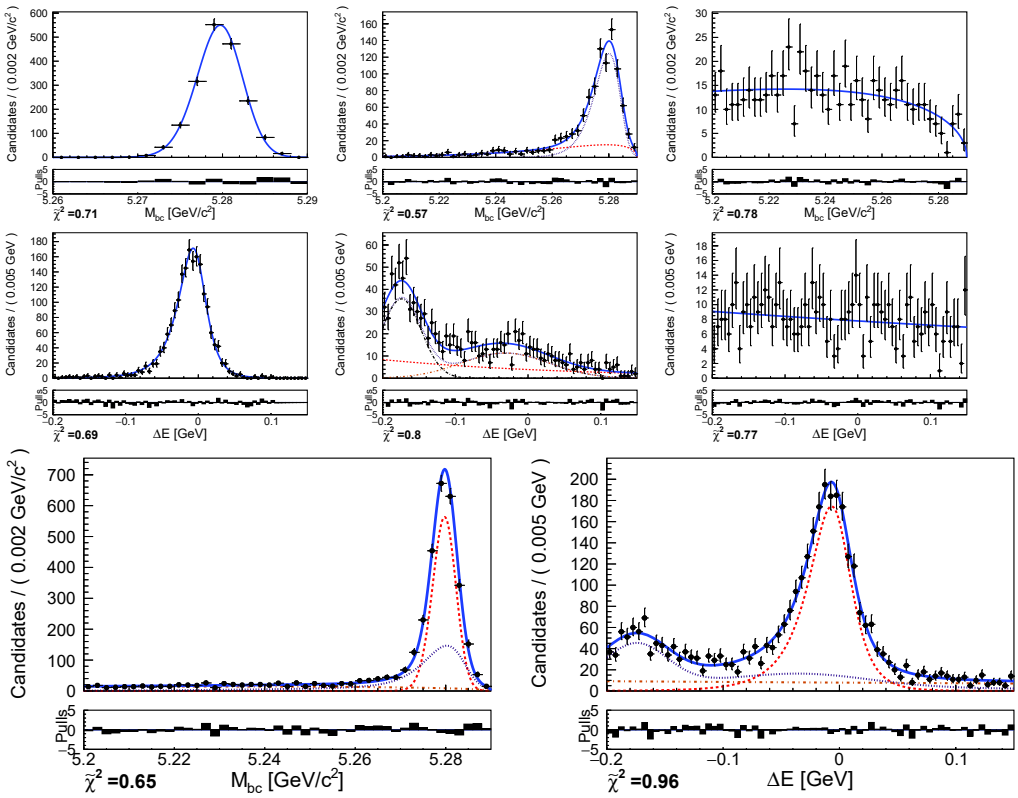


Figure 39: Fits projection for $B_d \to D^{*-}\pi^+$ ($D^0 \to K^-\pi^+\pi^0$). The first two rows show the projections in (*top*) M_{bc} and (*middle*) ΔE of the fits to the individual populations (*left*) signal, (*center*) $b\bar{b}$ background and (*right*) continuum background. The last row shows the projections in (*left*) M_{bc} and (*right*) ΔE of fit to extract the yields of the individual components.

Bibliography

[1] *PEP-II: An Asymmetric B Factory. Conceptual Design Report. June 1993*, .

[2] K. Oide, *KEKB B-factory, the luminosity frontier*, Prog. Theor. Phys. **122** (2009) 69–80.

[3] D. Atwood, M. Gronau, and A. Soni, *Mixing induced CP asymmetries in radiative B decays in and beyond the standard model*, Phys. Rev. Lett. **79** (1997) 185–188, arXiv:hep-ph/9704272.

[4] Y. Ushiroda et al., Belle, *Time-Dependent CP Asymmetries in $B^0 \to K^0_S \pi^0 \gamma$ transitions*, Phys. Rev. D **74** (2006) 111104, arXiv:hep-ex/0608017.

[5] J. Li et al., Belle, *Time-dependent CP Asymmetries in $B^0 \to K^0_S rho^0 \gamma$ Decays*, Phys. Rev. Lett. **101** (2008) 251601, arXiv:0806.1980 [hep-ex].

[6] B. Aubert et al., BaBar, *Measurement of Time-Dependent CP Asymmetry in $B^0 \to K^0_S \pi^0 \gamma$ Decays*, Phys. Rev. D **78** (2008) 071102, arXiv:0807.3103 [hep-ex].

[7] P. del Amo Sanchez et al., BaBar, *Time-dependent analysis of $B^0 \to K^0_S \pi^- \pi^+ \gamma$ decays and studies of the $K^+ \pi^- \pi^+$ system in $B^+ \to K^+ \pi^- \pi^+ \gamma$ decays*, Phys. Rev. D **93** (2016) no. 5, 052013, arXiv:1512.03579 [hep-ex].

[8] F. Abudinén et al., Belle-II, *Measurement of the B^0 lifetime using fully reconstructed hadronic decays in the 2019 Belle II dataset*, arXiv:2005.07507 [hep-ex].

[9] J. Bernstein, *Spontaneous symmetry breaking, gauge theories, the higgs mechanism and all that*, Rev. Mod. Phys. **46** (1974) 7–48. [Erratum: Rev.Mod.Phys. 47, 259–259 (1975), Erratum: Rev.Mod.Phys. 46, 855–855 (1974)].

[10] G. Aad et al., ATLAS, *Observation of a new particle in the search for the Standard Model Higgs boson with the ATLAS detector at the LHC*, Phys. Lett. **B716** (2012) 1–29, arXiv:1207.7214 [hep-ex].

[11] S. Chatrchyan et al., CMS, *Observation of a New Boson at a Mass of 125 GeV with the CMS Experiment at the LHC*, Phys. Lett. **B716** (2012) 30–61, arXiv:1207.7235 [hep-ex].

[12] T. Lee and C.-N. Yang, *Question of Parity Conservation in Weak Interactions*, Phys. Rev. **104** (1956) 254–258.

[13] C. Wu, E. Ambler, R. Hayward, D. Hoppes, and R. Hudson, *Experimental Test of Parity Conservation in β Decay*, Phys. Rev. **105** (1957) 1413–1414.

[14] R. Garwin, L. Lederman, and M. Weinrich, *Observations of the Failure of Conservation of Parity and Charge Conjugation in Meson Decays: The Magnetic Moment of the Free Muon*, Phys. Rev. **105** (1957) 1415–1417.

[15] J. Christenson, J. Cronin, V. Fitch, and R. Turlay, *Evidence for the 2π Decay of the K_2^0 Meson*, Phys. Rev. Lett. **13** (1964) 138–140.

[16] M. Kobayashi and T. Maskawa, *CP Violation in the Renormalizable Theory of Weak Interaction*, Prog. Theor. Phys. **49** (1973) 652–657.

[17] N. Cabibbo, *Unitary Symmetry and Leptonic Decays*, Phys. Rev. Lett. **10** (1963) 531–533.

[18] J. Charles, A. Hocker, H. Lacker, S. Laplace, F. R. Le Diberder, J. Malcles, J. Ocariz, M. Pivk, and L. Roos, *CKMfitter Group*, Eur. Phys. J. **C41** (2005) no. 1, 1–131, arXiv:hep-ph/0406184 [hep-ph].

[19] K. Lande, E. Booth, J. Impeduglia, L. Lederman, and W. Chinowsky, *Observation of Long-Lived Neutral V Particles*, Phys. Rev. **103** (1956) 1901–1904.

[20] H. Albrecht et al., ARGUS, *Observation of B0 - anti-B0 Mixing*, .

[21] B. Aubert et al., BaBar, *Evidence for $D^0 - \overline{D}^0$ Mixing*, Phys. Rev. Lett. **98** (2007) 211802, arXiv:hep-ex/0703020.

[22] Y. Amhis et al., HFLAV, *Averages of b-hadron, c-hadron, and τ-lepton properties as of summer 2016*, Eur. Phys. J. C **77** (2017) no. 12, 895, arXiv:1612.07233 [hep-ex].

[23] M. Tanabashi et al., Particle Data Group collaboration, *Review of Particle Physics*, Phys. Rev. D **98** (2018) no. 3, 030001.

[24] A. Einstein, B. Podolsky, and N. Rosen, *Can quantum mechanical description of physical reality be considered complete?*, Phys. Rev. **47** (1935) 777–780.

[25] Y. Grossman and M. P. Worah, *CP asymmetries in B decays with new physics in decay amplitudes*, Phys. Lett. B **395** (1997) 241–249, arXiv:hep-ph/9612269.

[26] S. P. Martin, *A Supersymmetry primer*, vol. 21, pp. 1–153. 2010. arXiv:hep-ph/9709356.

[27] Y. Nir, *CP violation in meson decays*, in *Les Houches Summer School on Theoretical Physics: Session 84: Particle Physics Beyond the Standard Model*, pp. 131–175. 2006. arXiv:hep-ph/0510413.

[28] P. L. Cho and M. Misiak, *b —> s gamma decay in SU(2)-L x SU(2)-r x U(1) extensions of the Standard Model*, Phys. Rev. D **49** (1994) 5894–5903, arXiv:hep-ph/9310332.

[29] K. Babu, K. Fujikawa, and A. Yamada, *Constraints on left-right symmetric models from the process b —> s gamma*, Phys. Lett. B **333** (1994) 196–201, arXiv:hep-ph/9312315.

[30] T. Inami and C. Lim, *Effects of Superheavy Quarks and Leptons in Low-Energy Weak Processes k(L) —> mu anti-mu, K+ —> pi+ Neutrino anti-neutrino and K0 <—> anti-K0*, Prog. Theor. Phys. **65** (1981) 297. [Erratum: Prog.Theor.Phys. 65, 1772 (1981)].

[31] S. Kurokawa and E. Kikutani, *Overview of the KEKB accelerators*, Nucl. Instrum. Meth. **A499** (2003) 1–7.

[32] P. M. Lewis et al., *First Measurements of Beam Backgrounds at SuperKEKB*, Nucl. Instrum. Meth. **A914** (2019) 69–144, arXiv:1802.01366 [physics.ins-det].

[33] W. Altmannshofer et al., Belle-II, *The Belle II Physics Book*, PTEP **2019** (2019) no. 12, 123C01, arXiv:1808.10567 [hep-ex].

[34] T. Abe et al., Belle-II, *Belle II Technical Design Report*, arXiv:1011.0352 [physics.ins-det].

[35] F. Luetticke, DEPFET collaboration, *The ultralight DEPFET pixel detector of the Belle II experiment*, Nucl. Instrum. Meth. A **845** (2017) 118–121.

[36] A. Bevan et al., BaBar, Belle, *The Physics of the B Factories*, Eur. Phys. J. C **74** (2014) 3026, arXiv:1406.6311 [hep-ex].

[37] T. Keck, *FastBDT: A speed-optimized and cache-friendly implementation of stochastic gradient-boosted decision trees for multivariate classification*, CoRR **abs/1609.06119** (2016) , arXiv:1609.06119. http://arxiv.org/abs/1609.06119.

[38] Y. Amhis et al., Heavy Flavor Averaging Group, *Averages of B-Hadron, C-Hadron, and tau-lepton properties as of early 2012*, arXiv:1207.1158 [hep-ex].

[39] J. Beringer et al., Particle Data Group, *Review of Particle Physics (RPP)*, Phys. Rev. D **86** (2012) 010001.

[40] J. F. Krohn et al., Belle-II analysis software Group, *Global Decay Chain Vertex Fitting at B-Factories*, arXiv:1901.11198 [hep-ex].

[41] W. Waltenberger, *RAVE: A detector-independent toolkit to reconstruct vertices*, IEEE Trans. Nucl. Sci. **58** (2011) 434–444.

[42] B. Collaboration, Belle Collaboration, *Precise Measurement of B Meson Lifetimes with Hadronic Decay Final States*, Phys. Rev. Lett. **88** (Apr, 2002) 171801. https://link.aps.org/doi/10.1103/PhysRevLett.88.171801.

Rasheed Reem

Recherche de nouvelles physiques grâce à la désintégration radiative de mésons B et mesure de leur temps de vie avec l'expérience Belle II

Juste après le Big Bang, matière et antimatière étaient présentes en quantités égales. Mais l'univers que nous observons aujourd'hui est presque entièrement constitué de matière. Une différence de comportement des particules et anti-particules constitue un ingrédient fondamental pour expliquer cette disparition. La violation de la symétrie quantique CP (Charge et Parité) introduit une telle asymétrie, cependant le niveau observé actuellement pour cette violation ne suffit quantitativement pas. L'expérience Belle II vient de démarrer au Japon, elle permet d'étudier avec une très grande précision des systèmes particules/anti-particules produits par le collisionneur électron-positron SuperKEKB , qui sera bientôt le plus lumineux au monde. Dans mon doctorant, J'ai travaillé sur la mesure de la violation de CP dans les désintégrations radiatives du méson B (désintégrations avec des photons à l'état final) particulièrement prometteuses grâce à leur haute sensibilité aux possibles nouveaux processus. Suite à cette analyse, j'ai commencé une nouvelle mesure de la durée de vie des mésons B, pour vérifier la robustesse des outils utilisés pour mesurer la violation de CP.

Mot clé: La violation de CP, collisionneur électron-positron, SuperKEKB, L'expérience Belle II, asymétrie, la durée de vie, le plus lumineux au monde, méson B

After the Big Bang matter and antimatter were present in equal amounts. Today, however, everything we see, is made almost entirely of matter. A fundamental ingredient to explain this asymmetry between matter and antimatter is the violation of the CP (Charge Parity) symmetry. CP violation has been observed but quantitatively not enough to explain the huge asymmetry. The Belle II experiment in Japan studies the particles produced in electron-positron collisions at the SuperKEKB collider, the highest intensity collider in the World, allowing a high precision measurements of the known sources of CP violation and looking for new ones. In my PhD, I worked on measuring the CP violation in B meson radiative decays (decays with photon in final state) particularly promising thanks to their high sensitivity to possible new processes. Following this analysis, I started a new measurement of the B mesons lifetime where I could verify the robustness of the tools used in the CP violation measurement.

Keywords : CP violation, lifetime, B meson, SuperKEKB collider, Belle II, asymmetry, collider,, Electron-Positron Collisions, highest intensity,